Methodologies for Earth Observation with Hyperspectral Analysis and Multimodal Image Fusion

Ping Ma

Centre for Excellence in Signal & Image Processing,

Department of Electronic & Electrical Engineering,

University of Strathclyde, Glasgow, Scotland

This thesis is submitted for the degree of

Doctor of Philosophy

March 2022

Declaration

This thesis is the result of the author's original research. It has been composed by the author and has not been previously submitted for examination which has led to the award of a degree.

The copyright of this thesis belongs to the author under the terms of the United Kingdom Copyright Acts as qualified by University of Strathclyde Regulation 3.50. Due acknowledgement must always be made of the use of any material contained in, or derived from, this thesis.

Signed: *Ping Ma*

March 2022

Acknowledgements

The three years studying experience in the United Kingdom is a treasure for my whole life. I have learnt different cultures, thoughts and gained lots of academic research knowledge, which have profound effects on how I plan my future life. I would like to pay my thanks to the people who has helped me to complete the PhD studying and go through difficulties in the UK.

First, to my supervisor, Prof. Jinchang Ren, many thanks for your kind support and guidance. You have helped me to start my UK studying journey, taught me many research skills, provide expert insights, helped me revise and edit articles, given many valuable suggestions on life and future career. I am gratitude to what you have done in favour of the scholarships I applied, which makes all PhD research works being possible. Many thanks to the time you have given to help me.

My supervisor, Prof. Malcolm Macdonald, it is a true pleasure to work with you for the last year of PhD studying. I have learnt a great deal from you and successfully completed the SAGES-MASTS Policy internship work and thesis with your help. The group meetings let me have chances to communicate with other researchers and gained a lot of suggestions and comments for my research improvement. Thank you for you have done in support of my PhD studying.

I would also present my gratitude to those who have studied at Royal College Building. In particular, Dr. Paul Murray, Dr. Yijun Yan, Mr Guoliang Xie, Dr. Ahmed Alzin, Ms Xiaoquan Li, Mr Faxian Cao. You all helped me a lot not only for the academic exchanges, but also for the difficulties in life. My roommates and friends all helped me to quickly adapt to the life in Glasgow, clear my head and recharge, and have a nice and unforgettable time in the UK. In addition, I would like to show my appreciations to the researchers I knew in the last year, including Dr. Sally Rouse, Dr. Astrid Werkmeister, Dr. Ruaridh Clark, Dr. Christopher Lowe, Dr. Steven Owens, Dr. Ciara McGrath, Olabamiji Olojo and Adah Tole. I have received many useful suggestions and comments to improve my research and dissertation. In addition, to my supervisor in master studying, Prof. Genyun Sun, many thanks for leading me into the

remote sensing research field and providing many supports for my studying abroad. You all played an important role in helping me achieve this lifelong goal.

To my Mum and Dad, Weixiu Ma and Changsheng Ma, thank you for providing me a happy life and supporting every decision I have made. To my husband, Jie Sun, thanks for your patience, understanding, support and sympathy. To my little brother, Taiwei Ma, thank you for always being there to support me.

Last but not least, I owe a great deal of gratitude to the China Scholarship Council, the University of Strathclyde JARA Scholarship and the SAGES-MASTS Policy Internship organized by Marine Scotland Science. Without these funding support, this research work would not be possible.

Abstract

Ping Ma. *Methodologies for Earth Observation and Remote Sensing with Hyperspectral Imaging and Multimodal Image Fusion.* Ph.D. thesis, University of Strathclyde, 2022.

Remote sensing has been one of the most common approaches to acquire relevant information for Earth observation, using both active and passive devices. With different sensors and platforms, various aspects of the Earth's surface can be observed for analysis. Facing the considerable multimodal heterogeneous remote sensing data, how to effectively extract the key information to support the varying needs from different applications has become a big challenge. Due to different characteristics of the remote sensing datasets acquired from various sensors and conditions, effective technologies are demanded for accurate and efficient data interpretations. In this thesis, the object identification and pixel-level classification task on the multimodal remote sensing data is particularly focused, especially the Hyperspectral imagery (HSI), Multispectral Instrument (MSI) and the Syntenic Aperture Radar (SAR) to facilitate different Earth observation tasks.

Although HSI has rich spectral information to enable the high discrimination ability for subtle spectral differences on materials, it suffers from different sources of noise and highly correlated spectral information. Despite of various approaches which have been proposed for denoising/smoothing and data reduction, the efficacy is still affected even using the corrected dataset (the data with the water absorption bands and noise bands discarded), especially when the training samples are limited and unbalanced. In this thesis, A signal decomposing technology is introduced into HSI for more effective feature extraction and improved data classification, where a superpixelwise multiscale Prophet model (SMP) is proposed for noise-robust feature extraction and effective classification of the HSI. The prophet model can deeply dig into the complex latent structures of HSI and extract features with enlarged interclass diversity and improved intraclass similarity. Firstly, the first three principal components of the HSI are extracted for implementing the superpixelwise segmentation, where pixels are grouped

into regions with adaptively determined sizes and shapes. Secondly, a multiscale prophet model is utilized to extract the multiscale informative trend components from the average spectrum of each superpixel. Taking the multiscale trend signal as the input feature, the HSI data are further classified superpixelwisely, which is further refined by majority voting based decision fusion. Experiments on three publicly available datasets have fully validated the efficacy and robustness of the proposed approach, when benchmarked with several state-of-the-art classifiers, including some typical spatial-spectral methods and deep learning classifiers. In addition, both quantitative and qualitative assessment has validated the efficacy of our approach in noise-robust classification of HSI even with limited training samples, especially in classifying uncorrected data (without pre-filtering the water-absorption and noisy bands).

The proposed SMP method focuses on the multiscale noise removal in spectral domain, which shows limited performance in spatial noise filter. In order to explore spatial noise-robust features whilst reducing the data dimension, a novel effective and efficient feature extraction framework is proposed for the HSI, namely Multiscale 2D singular spectrum analysis (2D-SSA) with principal component analysis (2D-MSSP). This method investigates the multiscale strategy in the spatial domain by combining the dimension reduction in the spectral domain. First, multiscale 2D-SSA is applied to exploit the multiscale spatial features in each spectral band of HSI via extracting the varying trends in different windowing scales. Taking the extracted trend signals at each scale level as the input features, the principal component analysis (PCA) is employed to the spectral domain for dimensionality reduction and spatial-spectral feature extraction. The derived spatial-spectral features in each scale are separately classified and then fused at the decision level for efficacy. As our 2D-MSSP method can extract features whilst removing the noise simultaneously in both the spatial and spectral domains, it is proven to be particularly noise-robust for data classification of HSI, when being benchmarked with several state-of-the-art classifiers, including effectively classifying of uncorrected data with limited training samples.

The MSI and SAR are also increasingly used in Earth observation and remote sensing. The capabilities of all-weather and all-day operation of the SAR enable it to be compatible with MSI, which usually suffers from severe weather conditions, e.g.,

cloud-covering but benefits from high spatial and spectral resolutions. Based on this, combination of SAR and MSI data is applied for the detection of offshore infrastructure, which is particularly challenging due to the noisy and vast ocean surface. In this thesis, we propose an automatic method for the geolocation and size evaluation of offshore infrastructure through the combination of Sentinel-1 SAR data and Sentinel-2 MSI imagery. Specifically, three strategies, transformed median composite, 2D-Singular Spectrum Analysis (SSA) filtering and threshold segmentation, are applied to first extract the 'guide area' of the infrastructure in the Sentinel-1 images, followed by applying morphological operations on a cloud free Sentinel-2 true color image of the 'guide area' to obtain the precise location as well as estimating the size of each structure. For each scene, five time-series Sentinel-1 data and one Sentinel-2 image are used for automatic identification. With validation against ground truth data of Scottish waters from the baseline and closing bays, to the limit of the Exclusive Economic Zone of Scotland, an area of 371,915 km2, our method automatically identifies 329 objects with an omission error of 1.20% and a commission error of 0%. For the size evaluation of wind turbine, oil/gas platform and semi-permanent object, the achieved size errors are around 1, 2 and 13 pixels, respectively in Sentinel-2 image. The method provides an effective technique for the identification of offshore infrastructure.

Table of Contents

List of Figures

List of Tables

Acronyms / Abbreviations

Acronyms / Abbreviations	Meaning
AA	Average accuracy
ASMGSSK	Adjacent superpixel-based multiscale spatial-spectral kernel
ATSR	Along track scanning radiometer
AVIRIS	Airborne visible/infrared imaging spectrometer
BLP	Bridge-linked platform
CD-CNN	Contextual deep convolution neural network
CFAR	Constant false alarm rate
CNN	Convolution neural network
CNN-PPF	Pixel-pair features-based convolution neural network
CR	Compression reception
2D-SSA	Two-dimensional singular spectrum analysis
2D-MSSA	Multiscale two-dimensional singular spectrum analysis
2D-MSSP	Multiscale two-dimensional singular spectrum analysis with principal component analysis
DBN	Deep belief network
DP	Drilling and process
DR-CNN	Diverse region-based convolution neural network
EEZ	Exclusive economic zone
EMD	Empirical mode decomposition
EEMD	Ensemble empirical mode decomposition
ESA	European space agency
EVG	Eigenvalue grouping
FPSO	Floating production storage and offloading
FSU	Floating storage unit
FS^{2}LRL	Fast superpixel based subspace low rank learning
GAN	Generative adversarial network
GF-2	Gaofen-2
HSI	Hyperspectral imagery

ICS	Iterative censoring scheme
IMF	Intrinsic mode function
IMFG	IMF Grouping
IW	Interferometric wide
KLFDA	Kernel local Fisher discriminant analysis
KNWFE	Kernel nonparametric weighted feature extraction
LDA	Linear discriminant analysis
LRR	Low-rank representation
MCP01	Manifold and compression platform 01
MODIS	Moderate-resolution imaging spectroradiometer
MRF	Markov random field
MSE	Mean size error
MSER	Mean size error rate
MSI	Multispectral imagery
MSP	Multiscale superpixel
MSuperPCA	multiscale superpixelwise principal component analysis
NASA	National aeronautics and space administration
NDA	Nonparametric discriminant analysis
NDWI	Normalized difference water index
NMF	Non-negative matrix factorization
NPCs	The number of principal components
NWFE	Nonparametric weighted feature extraction
OA	Overall accuracy
OGA	Oil and gas authority
OSP	The offshore substation platform
OSPAR	Oslo and paris commissions
OTMs	Offshore transformer modules
PC	Principal component
PCA	Principal component analysis
PDQ	Production, drilling and living quarters
PDR	Processing, drilling and riser
PUQ	Process, utilities and quarters

QU	Quarters and utilities
RBF	Radial basis function
RF	Random forest
RNN	Recurrent neural network
ROSIS	Reflective optics system imaging spectrometer
SAE	Stacked autoencoder
SAR	Synthetic aperture radar
SE	Size error
SER	Size error rate
SLIC	Simple linear iterative clustering
SMLR	Sparse multinomial logistic regression
SMP	Superpixelwise multiscale Prophet
SNR	Signal-to-noise ratio
SpATV	Spatially adaptive total variation
SPM	Single point mooring
SSA	Singular spectrum analysis
SS-GAN	Spatial-spectral generative adversarial networks
SS-LRR	Superpixel segmentation and low-rank representation
SVM	Support vector machine
SVD	Singular value decomposition
TCP	Treatment compression platform
TP	Treatment platform
VNF	Network function virtualization
VOD	Vegetation optical depth
WHP	Wellhead platform

Nomenclature

Symbol	Definition	Section
A	Column vector	4
a	The elements of an input matrix for Hankelization	4
C	Carrying capacity of Trend component	3
C	The number of class labels	4
c	Class label	4
Cl	The number of class labels	3
D	Total number of bands	All
Day	The predefined holiday days	3
$Dist$	Distance	3
F	Indicator function	4
G	Geometric factor	3
g	Trend component in the Prophet model	3
H	Hankel structure	4
h	Holiday effects in the Prophet model	3
I	Gray image	All
i	One pixel of input image	3
I_{spa}	Reconstructed image	4
j	One pixel of input image	3
k	The number of superpixels	3
L_x, L_y	Window length	4
L	The number of principal components	4
l	Class label	3
M	Classification map	3
m	Offset	3
M	The number of subsets	4
Mf	The final classification map	3
Mp	Regular period in Seasonality	3
N	Fitting factor in Seasonality	3
N	The image size	4

N	The number of detected pixels	5
n	Total number of pixels of input image	3
P	The grouped individual components	4
p	Periodic seasonality in the Prophet model	3
p_e	The proportion agreement occurring by chance	3
R	Segmentation scale	3
r	Growth rate	3
r	spatial resolution	5
S	Classification maps	4
S	Topside area of offshore infrastructure	5
s	Topside area of one pixel in the Sentinel-2 image	5
s	Changepoint	3
Sc	The number of correctly classified samples	3
SP	Superpixelwise mean spectra	3
St	The total number of samples for each class	3
T	The number of scales	3
t	Time	3
U	Eigenvectors	4
V	principal components	4
v	Fitting factor in Holiday effects	3
W	A sliding window in 2D-SSA	4
X	Trajectory matrix	4
x	Intensity values of input image	3
y	The output result for Hankelization	4
Z	Indicator for holiday events	3
ε	Error term	3
δ	Rate adjust vector	3
ϕ	Adjustment on offset parameter	3
β	Seasonal factor	3
κ	Change magnitude of holiday events	3
κ	Kappa coefficient	5

1 Introduction

1.1 Motivation and objective

In 1972, the National Aeronautics and Space Administration (NASA) launched the first Earth observation satellite, Landsat 1, which started the observation on earth surface from space [1, 2]. From then, many countries have developed the space technology and successfully created, launched and operated various satellites for enhanced Earth observation [3]. In general, the sensors carried by these satellites can detect, record and measure the electromagnetic energy reflected or emitted at different wavelengths from distant Earth's surface [2]. Based on the amount of radiation (radiances), the properties of different objects and materials can be extracted and analysed. This non-contact, long-distance detection technology is also called Remote Sensing. Recently, with the developments of imaging sensor, other Earth observation and data acquisition approaches including airborne surveying and photogrammetry are also proposed for remote sensing [4, 5]. Subsequently, the multispectral, multitemporal, multiangle and multiscale observations for the Earth surface has been realized. Remote sensing technology has been applied in many areas, such as land cover mapping [6, 7], vegetation dynamics observation [8, 9], water quality monitoring [10, 11], and urban growth analysis [12, 13].

Based on the type of energy source, remote sensing techniques can be divided into passive sensing and active sensing [14, 15]. In the passive remote sensing, sensors observe objects relying on external energy sources, such as the sun. These passive sensors have various sensitivities to radiations at different wavelengths in the electromagnetic spectrum [16]. With the technology development in passive sensor, the spectral resolution is correspondingly improved with different kinds of images acquired including panchromatic image, multispectral image and hyperspectral image [17]. The panchromatic image only has one spectral channel, which is difficult to identify the complex land covers. In 1970s, the multispectral sensors start to be applied in the earth observation. It can capture visible spectrum, near-infrared radiation, short-

wave infrared radiation and other wavelengths [18]. In general, there are tens of spectral bands, usually less than 20, in multispectral imagery, which shows effectiveness in discriminating various land surface features and landscape patterns. With the increasing demands of higher spectral resolution, the hyperspectral sensor is further developed, which measures energy in narrower but much more spectral bands than multispectral sensors. The captured hyperspectral imagery (HSI) usually contains hundreds of contiguous spectral bands across the entire electromagnetic spectrum [19]. This rich spectral information in HSI allows for accurate discrimination of materials with subtle spectral differences than panchromatic and multi-spectral remote sensing [20]. However, these advantages lead to increasing complexity of the system in terms of lighting, filtering, and optical design. Fig. 1.1 shows the data with different spectral resolution.

| (a) | (b) | (c) |
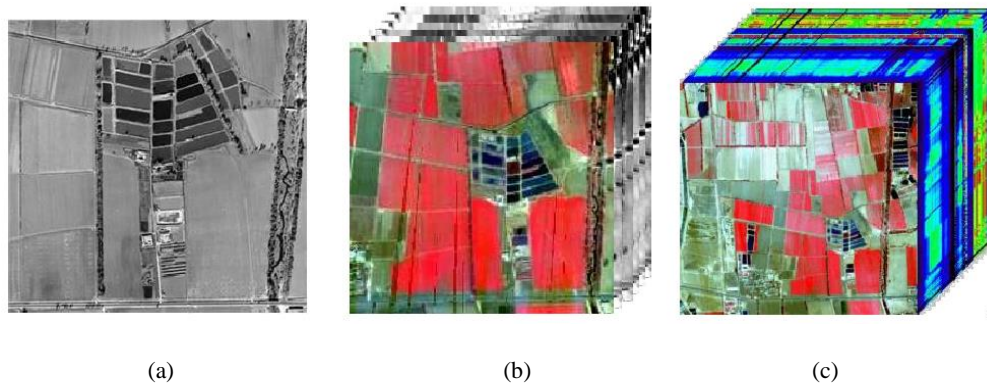
Fig. 1.1 The remote sensing data with different spectral resolution: (a) Panchromatic image, (b) Multispectral image and (c) Hyperspectral image.

In HSI, many contiguous bands are highly correlated, in which spectra changes gradually and slightly [21, 22]. That is, the extremely high dimension in the spectral domain contains not only the discriminative information but also high redundancy. The hundreds of spectral bands have enabled a large number of applications for HSI. Nevertheless, for a certain application problem, not all bands are useful to reveal the absorption characteristics of the interested materials, especially for the machine learning tasks such as image classification, where taking the whole spectral bands as the input can lead to the increasing computational load, curse of dimensionality [23] or the Hughes effect [24]. Thus, it is important to select and extract the most discriminative features to describe the properties of HSI data. In addition, due to the

environmental factors, limitations of the sensors and atmospheric effects, there inevitably exist bands with a low signal to noise ratio, such as the water vapour absorption bands and severely noisy bands [25]. This would unavoidably degrade the subsequent feature extraction and classification. Often, these water absorption bands are removed manually to get corrected HSI data (the data with the water absorption bands and noise bands discarded) for analysis [26]. However, this could lead to extra burden in filtering these bands and also result in loss of information from such bands. Hence, how to automatically deal with these highly noisy bands becomes another challenging task for effective and noise-robust feature extraction in HSI analysis. Besides, it is difficult to collect sufficient training samples in practice [27], where limited and unbalanced sampling in different classes can easily lead to the lack of training data [28]. These limitations can degrade the accuracy of target detection and image classification.

Overall, the multispectral and hyperspectral technologies have their own advantages in different tasks. The rich information of HSI over a contiguous spectrum make it more suitable for distinguishing subtle material differences, which can be easily missed by the multispectral system due to a larger sampling gap in the spectral domain. Nevertheless, on some certain applications, the light is required to be captured in selected wavelengths with certain range of the electromagnetic spectrum to be blocked, as other wavelengths may be noisy and affect the observation and analysis. Besides, input data with less dimension can further reduce the computational load and save the cost for processing.

The passive sensors are easily influenced by the weather condition, such as clouds, rain and fog [29]. Hence, another kind of sensor is employed, namely active sensors, in which own sources of radiation are used to "illuminate" the objects, at an additional cost, using a receiver system to record the returned energy [30]. The most common active sensor in remote sensing is Radar, which usually operates in the microwave regions of the electromagnetic spectrum and also stretches a little into the radio regions [16]. In Radar, an antenna is used to emit the radiation, in which the longer length generates a higher spatial resolution. In order to achieve this, a synthetic aperture technique is developed and provides higher resolution data for the observation [31].

As microwaves can penetrate the clouds, gases and even forests, ice and soil to some degree, this has made synthetic aperture radar (SAR) be able to deal with the cloud-covering problem, a bottleneck in multispectral/hyperspectral imagery. However, SAR data shows insufficient spectral information. Based on these, fusion of SAR and multispectral/hyperspectral data can combine the advantages of these two kinds of data, which has been employed in many remote sensing applications [32-34].

One of the applications is to identify the offshore infrastructure in a vast ocean area [35, 36]. The introduction of engineered structures to the marine environment can have profound effects on the ecosystems, including through interactions with oceanographic processes, biological productivity and the spatial distribution of fish, mammals, and birds [37, 38]. Authorities, in different countries, such as the global marine science community, governments/regulators and operators are actively seeking greater international alignment on installation and removal practices as well as policies for offshore infrastructure to ensure their impacts to the marine environment are minimized. This requires accurate and accessible knowledge on structures, especially their quantity, spatial distribution, and size. Globally, energy infrastructure including oil and gas platforms, and wind turbines constitute a substantial proportion of offshore structures [39, 40]. Many countries maintain databases of offshore energy structures. However, many of these databases have restricted access, inaccurate data, omissions, and/or lack up-to-date information [41, 42]. Moreover, oil and gas production platforms can be relocated, creating a risk to safe navigation of shipping if nautical charts are not promptly updated with new location data. Thus, a method to detect the location and properties of offshore infrastructure quickly and accurately is required. For this problem, there are many conventional survey approaches which can provide highly accurate detection. However, these methods are generally unsuitable for deployment at global scale due to time and cost requirements [29]. With the development of space-based remote sensing, satellite data offers a potential solution to this challenge, with short revisit periods, timeliness and larger area synchronous observations. For the observation of offshore infrastructure, satellites offer a frequently updated, and archived, near-global database. As such, how to effectively and efficiently use the kinds of satellite data to identify and estimate the offshore infrastructure needs further analysis.

The processing flowchart of different kinds of satellite data is shown in Fig.1.2. The work presented in this thesis aims to tackle the aforementioned challenging problems in satellite remote sensing, i.e., effective and noise-robust feature extraction for HSI data, and offshore infrastructure analysis by fusion of multimodal satellite data. In summary, the following objectives are defined in this thesis:
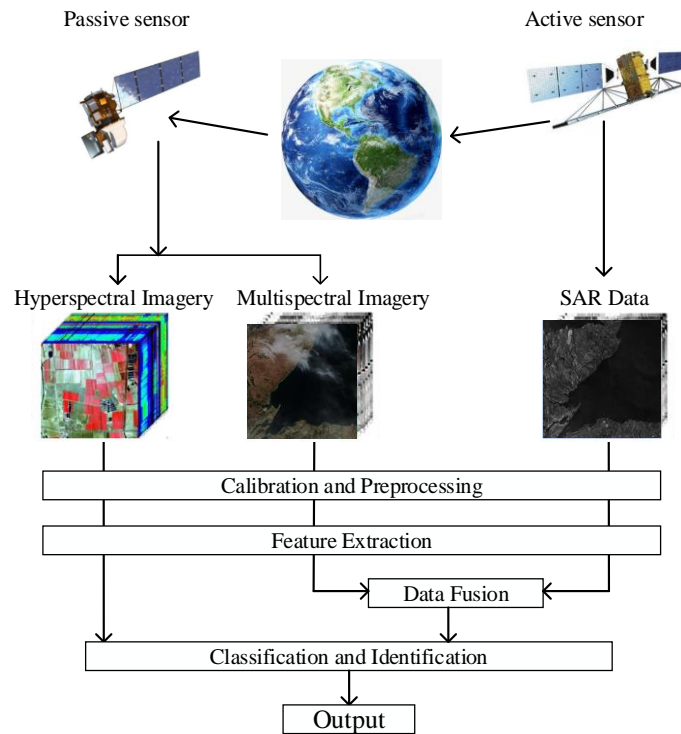
Fig. 1.2 The processing flowchart of different kinds of satellite data.

1. To develop a novel feature extraction method for hyperspectral images to deal with the highly redundant data and improve the subsequent classification accuracy even with a small number of training samples.

2. To explore a noise-robust approach for dealing with the water-absorption and noisy bands in HSI, i.e., to automatically extract discriminative features in HSI without manually filtering out water vapour absorption bands and severely noisy bands.

3. To introduce a new framework to quickly and effectively geolocate and measure the offshore infrastructure with multimodal satellite data.

1.2 Main contributions

In order to achieve the objectives summarized in Section 1.1, here three new approaches are proposed in this thesis, in which the major contributions are highlighted as follows.

1. To suppress the correlated spectral information and severe noise, a novel spectral-spatial feature extraction framework, Superpixelwise Multiscale Prophet model (SMP), is proposed, by combining the Prophet model, superpixel segmentation and multiscale strategy together. The prophet model can deeply dig into the complex structure features of HSI and enhance HSI features with enlarged interclass diversity and improved intraclass similarity. Through the superpixelwise fusion and multiscale fusion on the extracted trend components of the Prophet model, it achieves superior HSI classification even from the uncorrected dataset (data without pre-filtering the water absorption bands and noisy bands). Comprehensive experiments have fully validated the exceptional efficacy and robustness of the proposed model even under limited training samples. This addresses the points 1 and 2 of the defined objectives.

2. The proposed SMP method focuses on the multiscale noise removal in spectral domain, which shows limited performance in spatial noise filter. By combining the 2D singular spectrum analysis (2D-SSA) and the principal component analysis (PCA), a novel noise-robust spatial-spectral feature extraction method, namely 2D-MSSP, is proposed for addressing the noisy and water absorption bands in uncorrected HSI data. With different window sizes in 2D-SSA, multiscale spatial features are extracted and further processed by PCA for spectral domain dimensionality reduction. The derived features are separately classified and fused at the decision level for efficacy. Experimental results have validated the superior advantage of the proposed method in effective feature extraction whilst removing the noise simultaneously in both the spatial and spectral domains. This has provided a noise-robust solution for classification of HSI, even using the uncorrected dataset. This also addresses the first two research objectives as given in the previous section.

3. A case study for the geolocation and size evaluation of offshore infrastructure is implemented through the combination of Sentinel-1 Synthetic Aperture Radar (SAR) data and Sentinel-2 Multi-Spectral Instrument (MSI) imagery. First, three strategies are applied on Sentinel-1 data including transformed median composite, 2D- SSA filtering and threshold segmentation to extract the 'guide area' of the infrastructure. Then, the morphological operations are applied on a cloud free Sentinel-2 true colour image of the 'guide area' to obtain the precise location as well as estimating the size of each structure. Quantitative evaluation with various ground truth data have validated the efficacy of the proposed method in producing high accuracy results in terms of the geolocating and size measuring of the identified offshore infrastructure over the vast ocean surface. The developed solution actually has great potential for mapping and tracking of offshore platforms and wind turbines on a global scale. This addresses the point 3 of the defined objectives in the previous section.

To support the research in this dissertation, the following research articles have been produced/published:

- **Ping Ma**, Jinchang Ren, Huimin Zhao, Genyun Sun, Paul Murray, and Jiangbin Zheng. "Multiscale 2-D Singular Spectrum Analysis and Principal Component Analysis for Spatial–Spectral Noise-Robust Feature Extraction and Classification of Hyperspectral Images." *IEEE Journal of Selected Topics in Applied Earth Observations and Remote Sensing*, vol. 14, pp. 1233-1245, 2020. (published)

- **Ping Ma**, Jinchang Ren, Genyun Sun, Paul Murray, and Tariq Durrani. "Region Based Hierarchical Modelling for Effective Shadow Removal in Natural Images." In International Conference in Communications, Signal Processing, and Systems, pp. 2336-2342. Springer, Singapore, 2019. (published)

- **Ping Ma**, Jinchang Ren, Genyun Sun, Huimin Zhao, Paul Murray, Yijun Yan, and Jaime Zabalza. "Superpixelwise Multiscale Prophet Model for Noise-Robust Feature Extraction in Hyperspectral Images." (submitted)

- **Ping Ma**, Sally Rouse, Jinchang Ren, Malcolm Macdonald. "Geolocating and Measuring Offshore Infrastructure with Multimodal Satellite Data." (submitted)

1.3 Thesis structure

In Chapter 2, an overview is provided including the background introduction and related work for the feature extraction and data classification of HSI, and offshore infrastructure detection from varying satellite images. Chapter 3 describes the proposed SMP approach including the principles of the Prophet model, details of the SMP framework, and experimental results in comparison with seven spectral-spatial feature extraction approaches and four deep learning ones. In Chapter 4, the proposed noise-robust feature extraction method, 2D-MSSP, is presented, in which the 2D-SSA, PCA and multiscale strategy are described in detail. The experiments are illustrated mainly on uncorrected HSI data for demonstrating its noise-robustness. Chapter 5 introduces the proposed framework for geolocating and measuring offshore infrastructure in the Scottish waters. The proposed strategies in Sentinel-1 SAR data and Sentinel-2 MSI data are presented in detail in this chapter. The detection and size estimation accuracy are also estimated, analysed and discussed. Chapter 6 provides the concluding remarks and findings of the thesis as well as possible ideas and recommendations for future research work.

2   Background and Related Work

Based on the motivations and objectives summarized in Chapter 1, the background and related work are introduced in detail in this chapter as follows.

2.1 Feature extraction in HSI

In recent years, Hyperspectral image classification has become one of the most popular research topics. Its goal is to allocate the observations, i.e., pixel vectors in HSI with unique labels. The HSI classification faces challenges due to the data characteristics like high dimension and redundant features, as well as the limited and imbalanced distribution of training samples. In order to improve the classification accuracy, the discriminative features from the original HSI data and advanced classifiers that better separates the pixel vectors are all necessary.

2.1.1 Spectral feature extraction

In order to reduce the data redundancy and suppress noises in HSI, the feature extraction approaches have been intensively studied during the past decades. The conventional approaches mainly focus on the spectral feature extraction, which can be categorized as unsupervised (without any prior knowledge) and supervised (require training samples) techniques. Among the unsupervised ones, principal component analysis (PCA) [43-45] can achieve dimensionality reduction via a linear transformation. It transforms the original data into new feature space with uncorrelated components and the first few principal components contains the most useful information of input data. It is validated that the first three components preserve more than 90% energy of the original data [46]. Then only the first few principal components are selected for the further processing of input image, which significantly reduces the dimensionality and thus make the subsequent operations faster. It is quick and easy to carry out without any label information on the input data [47]. Other widely used spectral feature extraction methods like non-negative matrix factorization (NMF) [48, 49], independent component analysis (ICA) [50] [51] and minimum noise fraction

(MNF) [52] also can realize the dimension reduction on HSI. Compared with these linear techniques, non-linear feature extraction methods perform better on complex nonlinear data [22]. By introducing kernel trick [53], the kernel PCA [54], kernel ICA [55], kernel MNF [56] and kernel NMF [57] are developed. Besides, some signal decomposition methods are also introduced for the spectral feature extraction on HSI, such as singular spectrum analysis (SSA) [25, 58] and empirical mode decomposition (EMD) [59]. In these methods, the spectral data of each pixel in hundreds of bands is recognized as a signal. SSA can decompose the spectral data into several components including trend, oscillations and noises. By removing the noisy components, SSA is validated to improve the feature extraction performance on HSI [60]. Similarly, EMD is able to decompose the input signal into intrinsic mode functions (IMFs). However, its extracted spectral features decrease the classification accuracy on HSI data [59]. This problem is addressed by the ensemble EMD (EEMD) [61, 62].

Different from the unsupervised feature extraction methods, the supervised ones need training samples to derive the discriminative features. Linear discriminant analysis (LDA) is one traditional supervised approach that features are extracted based on the criterion of class separability calculated as proportion of scatter matrices in between-class and within-class [63, 64]. Its performance is limited by the training samples sizes and classes distributions. Nonparametric methods are further developed for this problem. Nonparametric discriminant analysis (NDA) [65] defines a weight for each sample according to its distribution on feature extraction. Nonparametric weighted feature extraction (NWFE) further introduces regularization techniques [66]. Also, kernel trick can transform aforementioned methods into non-linear models, such as kernel local Fisher discriminant analysis (KLFDA) [67] and Kernel nonparametric weighted feature extraction (KNWFE) [68]. However, these supervised feature extraction methods can increase computational load and affect image processing speed.

2.1.2 Spatial-spectral feature extraction

The spectral features are not enough to deal with the HSI scene with high intra-class disparity and inter-class similarity [6]. As presented in [69], the HSI data are supposed to be processed as an image rather than a collection of pixels. Thus, various spatial-spectral feature extraction methods are developed to consider both spectral and

contextual information [22]. The Gabor filter [70], wavelets [71], the extended morphological profile [6], Markov random field [72] and sparse representation [7] are all unsupervised techniques and have been applied to the HSI classification. In [73], a supervised spectral-spatial classification approach is proposed, which features a spectral data fidelity term derived from the sparse multinomial logistic regression (SMLR) and a spatially adaptive Markov Random Field (MRF) prior model constructed via spatially adaptive total variation regularization (denoted as SMLR-SpATV). This method could spatially smooth the images and gain robust results of classification even with very limited training samples. In [20], a 2-D extension to SSA method (denoted as 2D-SSA) is developed for effective spatial features extraction of HSI, in which each band image is decomposed into various components and reconstructed using trend and selected oscillation information. The 2D-SSA can extract the spatial structural features by using the characteristics of neighbouring pixels in a specified embedding window. It performs better in suppressing high noises and data classification. In 2D-SSA, the embedding window size is a key parameter that influences the informativeness and noise level of extracted features. However, it is a challenging work to select an optimal window size for all the spectral bands in different HSI datasets.

In real cases, the regions of interest are usually irregularly shaped and inconsistently sized [74]. Therefore, the spatial regions used for feature mining should be adaptive to the specific structures of the image. To this end, the superpixel has been employed to adaptively extract the spatial features. The superpixels in an image are local homogeneous regions with different sizes and shapes. It is found effective to represent the spatial-contextual information and improve the classification [75]. For example, in [76], a novel spatial-spectral model, adjacent superpixel-based multiscale spatial-spectral kernel (ASMGSSK), is proposed. This method employs the entropy rate superpixel segmentation algorithm for multiscale superpixels and then calculate kernel matrix on spatial-spectral features extracted within adjacent superpixels. The ASMGSSK achieves superior classification performance on HSI datasets with very limited training samples. In [47], a superpixelwise PCA approach is proposed by incorporating the spatial context information generated from superpixel technique into the spectral information with dimensionality reduction by PCA method. In [77],

multiscale superpixel (MSP) segmentation and subspace-based support vector machine (SVM), SVMsub, are combined for spectral-spatial classification of HSI. By using the simple linear iterative clustering (SLIC) for extracting superpixels, multiscale spatial features are combined and fused for improved classification of HSI.

With the advantage of providing hidden structure spatial-spectral features, the deep learning models have also been successfully applied for the HSI feature extraction and classification. In [78], a contextual deep convolution neural network (CD-CNN) is proposed to explore local contextual features employing a multiscale convolutional filter bank to extract local spatial-spectral features of neighbouring pixel vectors. The obtained multiscale spatial-spectral features are combined into a joint feature map for the further HSI classification through a fully convolutional network. A diverse region-based CNN (DR-CNN) is presented in [79], which integrates spectral features, spatial structure characteristics and semantic context-aware properties of every pixel using its surrounding areas from six diverse regions. These deep features are then fused in different scales and multiple levels from unequal layers. Zhong et. al [80] introduce the spectral–spatial features of HSI into the designed four types of convolutional and transposed convolutional layers of a generative adversarial network (GAN) to generate discriminative features from limited numbers of labelled samples. Hang et. al [81] use two layers of recurrent neural network (RNN), in which one layer is for eliminating redundancy between adjacent bands, the other is used to extract complementary information from nonadjacent spectral bands. The spatial features are further introduced by incorporating some convolutional layers. However, most of the deep learning methods demand more training samples to realize better classification performance and would perform poor when the training size is limited [76].

2.1.3 Noise-robust feature extraction

The aforementioned spectral and/or spatial feature extraction methods show superiority on the classification of corrected HSI data with image pre-processing where noisy and water absorption bands are manually removed. This can lead to information loss in these bands and increase the image processing burden. In recent years, many denoising techniques have been proposed to deal with the uncorrected datasets without removing noisy and water absorption bands. For example, Sun et al.

[82] present a fast superpixel based subspace low rank learning method (termed as FS2LRL) for HSI mixed noise removal. This method factorizes HSI data into two lower-rank sub-matrices in the spectral domain and exploit the local spatial low-rankness of superpixel regions in the decomposed subspace. In [75], the low-rank representation (LRR) is combined with superpixel segmentation (denoted as SS-LRR), in which LRR is applied to each superpixel to excavate the spatial-spectral information of HSI. In [83], the low-rank matrix approximation and an iterative regularization framework is proposed to denoise the low signal-to-noise ratio (SNR) bands while preserving high-SNR bands. These approaches can effectively remove different types of noise simultaneously on the simulated and real HSI datasets, however, achieve limited accuracy improvements on uncorrected HSI classification.

2.2 HSI data classification

The HSI data classification aims to identify the characteristics of the input pixels and classify them into different classes. The HSI classification methods include unsupervised classification, supervised classification and semi-supervised classification.

2.2.1 Unsupervised HSI classification

When only the unlabelled samples are available, the HSI images are required to be segmented into different sets without training samples. The commonly used unsupervised HSI classification methods in machine learning community mainly includes the density-based, graph-based, centroid-based, biological based and deep learning-based methods [84]. Some conventional centroid and density-based methods include *k*-means [85], fuzzy c-means [86] and density peaks algorithm [87]. Xie et al. [88] propose a novel clustering method by using density and distance between pixels. This method develops an adaptive-bandwidth probability density function as the density metric and the Euclidean distance is employed for estimating the distance of pixel vectors in different bands. Zhao et al. [89] present a spectral clustering method for large-scale HSI data unsupervised classification, which introduces Nyström extension and anchor-based graph to form the affinity matrix. It effectively reduces the computational cost in clustering. The biological-based clustering methods usually

realize the clustering using the swarm intelligence in ecology, such as the automatic clustering method on basis of multilevel quantum ant colony optimization [90] and particle swarm optimization-based HSI clustering method [91]. Recently, the deep learning-based clustering approaches are also developed, such as Laplacian regularized deep subspace clustering [92], deep k-means clustering [93], deep embedded clustering [94], graph convolutional subspace clustering [95] and deep self-evolution clustering [96].

HSI data usually shows high dimensional, complex and nonlinear capabilities [97], which increases the difficulty in classification, especially the unsupervised methods. This requires that the input features are discriminative enough to be identified and classified by the unsupervised model. In recent years, the manifold learning is proposed and developed, which has been demonstrated its potential in modelling nonlinear data structure and reducing nonlinear dimensionality [98, 99]. It can characterize the topology of high-dimensional nonlinear HSI data in the lower dimensions for classification [100]. To realize this, a graph embedding framework is often used [101]. Lunga et al. [100] summarize the traditional graph-based nonlinear dimensionality reduction methods and propose a framework to represent HSI spectrum in terms of graph weights. The unsupervised clustering methods are usually used for the final classification. Wang et al. [102] present a fast spectral clustering with anchor graph by combining spectral and spatial features, which significantly reduce the computational complexity compared to traditional graph-based clustering approaches. Zhang et al. [103] develop an unsupervised HSI classification framework by proposing a unified low-rank matrix factorization to reduce the dimensionality and cluster data. This method also employed an out-of-sample extension trick for addressing large-scale HSI data.

2.2.2 Semi-supervised HSI classification

Semi-supervised classification represents the intermediate ground between supervised and unsupervised classification algorithms. It combines labelled and unlabelled datasets during training. One commonly used semi-supervised classification is based on the graph strategy. A graph is constructed by nodes and edges to represent data structures. Camps-Valls et al. [104] propose a semi-supervised graph-based method to

deal with the high dimensional HSI with limited labelled samples. This method uses both unlabelled and labelled samples to train the classifier, which capture the intrinsic structure of these samples and achieves stable and good classification performance. Shao et al. [105] introduce the sparse representation into graph-based approach and present a probabilistic class structure regularized sparse representation method, in which a small number of labelled samples are used to characterize the probabilistic relationship of data to generate discriminative coefficients in sparse representation model. He et al. [106] develop a fast semi-supervised HSI classification method using anchor graph in order to deal with large HSI data. The non-parametric, sparse and scale invariant capabilities of anchor graph enable it to efficiently discriminate the label of samples, which significantly reduce the computational complexity.

In addition, with the popularity of deep learning technique in computer vision community, it has also been successfully employed in the semi-supervised HSI classification. Wu et al. [107] use the labelled data and abundant unlabeled data with cluster labels to pre-train the convolutional recurrent neural networks and then employ the limited available labelled data for fine tuning. The cluster labels of unlabeled data are generated by a new proposed constrained Dirichlet process mixture model which fully utilizes the spectral and spatial information. Wang et al. [108] combines the convolutional conditional random fields with region growing strategy to propose a new HSI semi-supervised classification architecture. The region growing strategy can avoid the challenges of limited labelled samples and convolutional conditional random fields can maintain more detailed information in the image for fine-grained predictions.

2.2.3 Supervised HSI classification

The supervised classification is the most widely used HSI classification method. With a certain number of pixels in each class are labelled in prior, the supervised classifier can be trained for better identify the characteristics of the input pixels and classify them into different classes. At present, the main supervised methods include SVM [109], random forest (RF) [110], neural networks [111] and deep learning approaches [78].

Random forest is a non-parametric supervised classifier [112]. It grows many

regression and classification trees using the randomly selected training samples and input feature vectors. Each tree can provide a classification and the final classification results is decided by trees ensemble learning, i.e., "votes" over all the trees in the forest. For the HSI data classification, the RFs show efficiency in handling the large data bases [113], thousands of input features [114], missing data [115] and importance of different features [116]. Zhang et al. [117] propose a cascaded random forest method, in which the boosting strategy is introduced into RF with out-of-bag error added to update the sample weights. In this method, several base classifiers are trained at each iteration, which is different from that in boosting strategy. Wang et al. [118] combine the random forest with deep convolutional neural network for classification accuracy improvement, in which the deep convolutional neural network is employed as individual classifier for feature extraction and RF is used to construct a multiple classifier system for ensemble learning. Some other RFs variants are also proposed, such as rotation random forest [119], canonical correlation forests [120] and deep random forest [121, 122].

SVM shows promising performance in coping with high dimensional HSI data under the small size of training samples [123, 124]. It aims to separate the input data by finding an optimal hyperplane to maximise the margin, which is the closest distance between input feature vectors of different classes. With the more applications on the complex nonlinear data, the kernel strategy is subsequently introduced into SVM [125]. SVM classifier is also widely used in the HSI data classification, such as the rotation-based SVM [126], intelligence algorithm optimized SVM [127] and deep SVM [128]. Zhu et al. [127] introduce three intelligence algorithms including particle swarm optimization, genetic algorithms and artificial bee colony into SVM classifier for the parameter optimization, which aims to improve the feature selection ability and HSI classification accuracy under small sample size. Okwuashi et al. [128] integrate the SVM with deep learning techniques to develop a deep SVM classifier for a robustness classification. In this method, four kernel functions, gaussian radial basis function, exponential radial basis function, neural and polynomial, are employed with interconnecting weights acquired from stand-alone SVM.

The deep learning approaches can extract high-level features as well as achieve

promising HSI classification performances. Deep learning methods usually adopt the logistic model, softmax function as the classifier. The most widely used deep learning approaches include stacked autoencoder (SAE) [129, 130], deep belief network (DBN) [131], convolutional neural network (CNN) [132], recurrent neural network (RNN) [133], and generative adversarial network (GAN) [134].

2.3 Offshore infrastructure detection

2.3.1 Detection in optical data

Xing et al. use [135] Landsat 5/TM and Landsat 7/ETM+ data to detect ships and offshore oil/gas platforms in the Bohai Sea to assess the oil spill risk. Liu et al. propose [29] an automatic method with the Landsat-8 OLI (band 6) for the detection of offshore platforms in Persian Gulf, the Gulf of Mexico and the Gulf of Thailand. This method considers the features of spectra, texture, size, location and shape to discriminate the platforms from ocean background. Zhao et al. [136] identify offshore oil/gas platforms in the South China Sea using Landsat optical images through multitemporal image lamination and adaptive threshold segmentation with multiple sliding windows. Fan et al. [137] realize the automatic detection of offshore platforms in the Bohai Sea area using high resolution images from the Gaofen-2 (GF-2) MSS sensor, using time series images, an order statistical filtering approach, and a morphological operator. In order to improve the platform detection accuracy with a single image, Zhu et al. [138] employ the Harris detector and intensity-texture feature image to extract the platforms from a Sentinel-2 L2A Image in Persian Gulf of Mexico area. Zhu et al. [139] propose an automatic method for offshore platforms identification on Landsat 7 ETM+ images in Caspian Sea area. This method builds a cloud shadow-free Normalized Difference Water Index (NDWI) composite and a multiple threshold segmentation to remove the influence of cloud and extract drilling rigs. Strikingly, these methods all employ optical imagery and so suffer from cloud contamination, which can significantly reduce the number of available images for object detection.

The high temperature and brightness of waste gas flames at night have also been used for the identification and monitoring of oil and gas platforms. Croft [140] firstly uses the DMSP/OLS night-time light image data to identify the waste gas flame.

Chowdhury et al. [141] propose a fast and semi-automated endmember extraction method to extract daytime gas flares in Alberta using Sequential Maximum Angle Convex Cone with the short-wave infrared of 1.6 µm and 2.2 µm Landsat-8 images. Casadio et al. [35] monitor the night-time gas flaring activity of the extracted offshore oil/gas platforms in the North Sea area through the fusion of Synthetic Aperture Radar (SAR) and Along Track Scanning Radiometer (ATSR) data. The positions of rigs are firstly extracted by SAR data, and then flaring activity is estimated on the short-wave infrared band (1.6 µm) at ATSR. Anejionu et al. [142] develop a double threshold segmentation approach for the retrieval of the flaring location and the gas combusted volume in the Niger Delta from 2000 to 2014 through nighttime Moderate-resolution Imaging Spectroradiometer (MODIS) thermal imagery. Elvidge et al. [143] further refine the network function virtualization (VNF) algorithm [144] to extract global waste gas combustion sources based on the thermal anomalies with high-resolution National Polar-orbiting Operational Environmental Satellite System Preparatory Project/Visible infrared Imaging Radiometer images. Some, but not all, of these methods resolve the issue of cloud contamination however they are only applicable to platforms with gas combustion, and therefore not able to detect the full suite of energy infrastructure in the marine environment.

2.3.2 Detection in SAR data

Given the capabilities to image through cloud, and in darkness, SAR can overcome the shortcomings of optical imagery. For example, An et al. improve [145] the Constant False Alarm Rate (CFAR) detectors with a modified Iterative Censoring Scheme (ICS) for ship extraction utilizing RADARSAT-2 ScanSAR data. This method extracts target pixels and adjacent pixels, and designs a new detector by sorting all testing pixels. A coherence image-based method [41] is proposed by using the combined coherence of more than two sub-apertures on RADARSAT-2 data for hierarchical ship detection. Multi-temporal SAR data has also been used, Cheng et al. [146] extract offshore oil/gas platforms from multitemporal ENVISAT ASAR data by a two-parameter CFAR detector. Wong et al. [42] detect offshore infrastructure including oil platforms or platform complexes and wind turbines by using multi-temporal SAR and Google Earth Engine, in which the median composite, Gaussian difference, thresholding and

morphological post processing are adopted. Zhang et al. propose [147] an automatic offshore platforms detection method using GF-3 SAR data on basis of a dual-step-modified model, in which the two-parameter CFAR and the Hough transform are employed to remove ship targets and detect oil/gas platforms. Liu et al. [148] systematically evaluate the geometric accuracy of offshore platforms detection on the different remote sensing images with various resolutions by using a position-invariance based method. The method achieves better results on the higher resolution optical data. The spatial sampling resolution of SAR data is however limited which creates a challenge for high rates of detection accuracy, especially for smaller infrastructure.

High accuracy detection of offshore infrastructure from remote sensing images remains a challenge due to the small size of some infrastructure (e.g. Mungo rig), dim targets and weak image features, noisy images (cloud, cloud shadow, mist, waves, etc.), false alarms (passing vessels) and vast sea area [29, 139]. There are limitations for offshore infrastructure detection associated with all types of satellite data. Optical imagery can provide rich spectral and spatial details and structural information, but suffers from cloud. SAR data can avoid the challenge of cloud but often shows inadequate spectral and spatial information, or swath width, for the fine analysis of small infrastructure like wind turbines at scale. Moreover, remote sensing data with poor spatial resolution creates difficulty in accurately identify each rig within closely gathered clusters, especially rigs linked with bridges.

2.4 Summary

In this chapter, related research on the feature extraction and data classification of HSI are reviewed, including the spectral, spatial and hidden features extraction, and the supervised, unsupervised and semi-supervised classification. These approaches can effectively smooth the input HSI data, derive the discriminative features and achieve promising classification performances. However, the study on improving the classification accuracy using the small number of training samples is still limited for the uncorrected HSI data without filtering out the water absorption and severely noise bands. Additionally, the literature review about the remote sensing application, i.e., detection of offshore infrastructure using the optical and SAR remote sensing data is

carried out. Most methods can better remove the background noises and moving ships to detect the oil/gas rigs. However, many of them utilize a large number of datasets and complicated strategies, which increase the computational time and work burden. Therefore, the effective and efficient method for the quick identification of these infrastructure is still desirable. Besides, the further analysis on the detected offshore infrastructure, like topside area of rigs and diameter length of wind turbines, are also challenging and limited in the present studies.

Given these limitations of current state-of-the-art methods mentioned above, we propose novel methods in this thesis. Firstly, we introduce the Prophet model and 2D-SSA to deal with the water absorption and severely noise bands under small training size. As a recently developed forecasting tool by Facebook, the Prophet model can deeply analyse data by decomposing it into different components whilst well preserving the trend component and the most informative part of signal [149]. The derived trend component is jointly decided by the information of former data in the series, making it robust to any missing or highly noisy data. The HSI also characterizes a sequential data though in the spectral domain [82], which contains highly nonlinear scattering noise and even missing data, thus it motivated us to apply the Prophet model in analysing the HSI. The prophet model can remove noises throughout continuous bands and generate new intensity value (gray level) of each band by considering the information of former bands, which makes it show robust capability to any missing or highly noisy data. Given this, the severely noises in water absorption bands can be better removed. In addition, the 2D-SSA method can supress noises of each pixel in HSI by considering the information of adjacent pixels. It shows strength in exploring noise-robust spatial features even on the water absorption bands. In this thesis, we also incorporate the multiscale strategy into both Prophet and 2D-SSA models to remove noises at different level throughout the hyperspectral bands, which is beneficial to the final data classification under limited and unbalanced training samples. Secondly, in order to propose an effective and efficient method for the geolocation of offshore infrastructure, we combine the strengths of SAR data and MSI imagery from the Sentinel satellites, in which only a small amount of data is used. No cloud removal operations are required in our method like the methods using optical images. Besides,

the limited research, topside area assessment of oil/gas platforms and diameter evaluation of wind turbines are explored in our proposed method.

3   Superpixelwise Multiscale Prophet model (SMP) for Noise-Robust Feature Extraction in Hyperspectral Images

3.1 Introduction

As an emerging technique with massive applications, hyperspectral images suffer from different sources of noise. Although various approaches are proposed for smoothing the images before feature extraction, the efficacy is still affected by the noise, even using the corrected dataset with the water absorption bands and noise bands discarded. Especially when the number of training samples is small, the performance of data classification is inevitably affected. Therefore, in order to solve these problems, a novel superpixelwise multi-scale Prophet model (SMP) is proposed in this chapter. With exceptional capability of the Prophet model in noise-robust trend extraction and data prediction for enhancing features with improved interclass diversity and intraclass similarity, we aim to realize improved classification even on uncorrected HSIs.

The remainder of this chapter is organized as follows. Section 3.2 introduces the principles of the Prophet model. Section 3.3 presents in detail the proposed SMP framework. The design of experiments including the testing datasets and parameter settings are discussed in Section 3.4. Section 3.5 presents the experimental results and analysis, followed by some summaries drawn in Section 3.6.

3.2 Principles of the Prophet Model

3.2.1 Concept and Algorithm of the Prophet Model

As a recently developed forecasting tool by Facebook for analysing time-series data of business [149], the Prophet model blends the advantages of judgmental (incorporate intuitive judgement, opinions and subjective probability estimates) and statistical (use machine learning and data mining) modelling to convert the forecasting problem to a curve-fitting task. As a nonlinear and decomposable model, the Prophet model can

deeply analyse data by decomposing a given time-series $y(t)$ into different components, in which the trend component represents the most informative part of signal.

$$y(t) = g(t) + p(t) + h(t) + \varepsilon_t \tag{3.1}$$

where $g(t)$ is the trend component modelling the non-periodic changes; $p(t)$ is the periodic seasonality component i.e. daily, weekly or annual seasonality; $h(t)$ denotes the holiday effects which usually appear on irregular schedules over one or more days; ε_t is the error term assumed in the normal distribution.

The trend component represents the most informative part of signal, which is widely defined by a logistic function [149].

$$g(t) = C \Big/ \Big(1 + \exp\big(-r_s \left(t - m_s \right) \big) \Big) \tag{3.2}$$

where C is the carrying capacity determining the maximum value of $g(t)$, r denotes the growth rate and m is an offset parameter. In $g(t)$, the growth rate r is defined to characterize the changes in trend component. More specifically, there are S changepoints set over the whole time t. At each changepoint s ($s = 1, ..., S$), the growth rate r is set to change for better curve-fitting. The rate change is defined as $\boldsymbol{\delta} \in \mathbb{R}^S$, where δ_s denotes the rate change at the s-th changepoint. Therefore, the growth rate r_s at any changepoint is calculated by adding the rate adjustment to the former growth rate.

$$r_s = r_{s-1} + \delta_s \tag{3.3}$$

where the base rate r_1 is determined by the Stan's L-BFGS [32] and the rate adjust vector $\boldsymbol{\delta}$ is represented by a sparse prior via a Laplace distribution: $\delta_q \sim \text{laplace}(\tau)$. The more explanations are given in Section 3.4.3. Based on the growth rate, the parameter m is correspondingly updated for connecting the trend at different changepoints. The adjustment on m at the s-th changepoint is defined as ϕ_s. Thus, the offset value m at s-th changepoint is given by:

$$m_s = m_{s-1} + \phi_s \tag{3.4}$$

where the base offset m_1 is also defined using the Stan's L-BFGS. The ϕ_s is calculated as:

$$\phi_s = (s - m_1 - \sum_{q<s} \phi_q)(1 - r_{s-1}/r_s) \tag{3.5}$$

where ϕ_1 is set to 0.

Business time series usually possess periodic phenomena due to the associated repeated seasonal behaviours [150]. To achieve this, the period function of t is employed as the Seasonality in the model. It employs a standard Fourier series to flexibly approximate the seasonal effects.

$$p(t) = \left[\cos\left(\frac{2\pi(1)t}{Mp}\right), ..., \sin\left(\frac{2\pi(N)t}{Mp}\right) \right] \beta \tag{3.6}$$

where Mp represents the expected regular period of data (e.g., $Mp = 7$ for weekly series when using days as the time scale). The parameter vector β is set to satisfy $\beta \sim \text{Normal}(0, \sigma^2)$. The factor N affects the fitting performance on the seasonality, where a large N results in more decomposed terms in $p(t)$. It allows seasonal patterns change more quickly with an increased risk of overfitting [149, 150].

In the forecasting of business time series, the holiday's effects are incorporated in a straightforward way based on the prior knowledge of the events as follows:

$$h(t) = Z(t)\kappa \tag{3.7}$$

where $Z(t) = \left[1(t \in Day_1), ..., 1(t \in Day_L) \right]$ is an indicator signifying if a time t is in the period of holiday events. The factor Day is the predefined holiday days. The parameter κ denotes the magnitude of the change caused by the corresponding holiday events

in the forecast, which is defined as $\kappa \sim \text{Normal}\left(0, v^2\right)$. Further details about the Prophet Model can be found in [149, 151].

3.2.2 Enhancing Features of HSI with the Prophet Model

From Eqs. (3.3-3.5), it is clear that the derived trend component is jointly decided by the information of the former data in the time-series. This can avoid the negative effect of some highly noisy data. As such, the Prophet model has great potential to analyse the complex HSI with noisy and water absorption bands. By taking the spectral data in hundreds of bands as a time-series, we can gain insights into the HSI, including decomposing the spectral profiles into different components to derive the informative parts i.e., the trend and mitigate noisy data in HSI.

For effective feature extraction, it is necessary to deal with the subtle interclass difference and large intraclass variability of HSI [152]. In order to evaluate the feature characterization ability of Prophet on HSI, the interclass and intraclass differences are calculated and assessed in this section. Here, some classic feature extraction approaches, such as SSA [25] and Mean filtering are compared with Prophet model. The raw spectral profiles are taken as the baseline for comparison, too. Besides, the Prophet model with and without seasonality settings are also evaluated to test the effects of seasonality components in feature extraction of HSI. For SSA, the window size is set to 5×5. Only the first component is used for eigenvalue grouping (EVG) according to the recommended configurations [25, 20]. The size for the mean filtering is set to 5×5. In the Prophet Model, the values of parameters τ, σ and N are set to 25, 0.5, 30 and 3 empirically in this test.

For evaluating how the Prophet model may affect the interclass diversity and intraclass variance, the Kullback-Leibler divergence [153] is employed, which is based on the information entropy theory to quantify the dissimilarity (or difference, distance and discrimination) between different data. Here, the Salinas dataset [154] is taken as an example. For each comparing approach, ten samples are randomly selected from each class of the 16 labelled classes. The Kullback-Leibler divergences among the samples from every two classes, each with all other classes on average, and within each class

are calculated. The results of interclass and intraclass Kullback-Leibler divergences are shown in Fig.3.1.
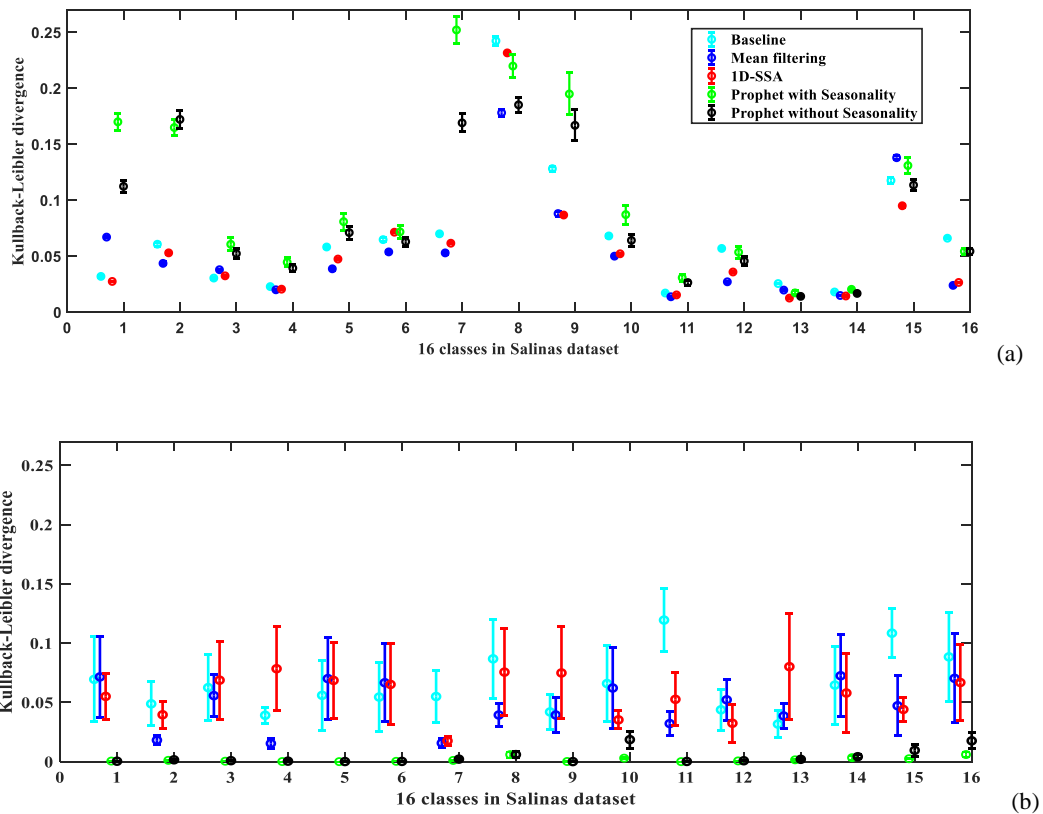
Fig. 3.1 The Kullback-Leibler divergence of classes in Salinas dataset: (a) interclass Kullback-Leibler divergence, (b) intraclass Kullback-Leibler divergence.

As seen in Fig. 3.1, the Prophet model achieves highest interclass Kullback-Leibler divergence and lowest intraclass Kullback-Leibler divergence in most classes. That is, the Prophet model can effectively improve the disparity between classes and similarity within each class, which would help enhance further data classification [155]. This validates the potential of Prophet in HSI feature extraction. The raw spectral profiles (Baseline) contain much noisy information. As shown in Fig.3.1, compared with Mean filtering and SSA, the Baseline exhibits higher interclass and intraclass Kullback-Leibler divergence. As for Mean filtering, it performs better in classes #1, #3, and #15 on interclass disparity and classes #2-#4, #7-#9, and #11 on intraclass similarity. The SSA shows higher interclass Kullback-Leibler divergence on the class #6 and better intraclass Kullback-Leibler divergence on the classes #1, #10, #12, and #14-#16. The main reason for the inferior performances of SSA and Mean filtering is that they filter

out the noisy contents only using the local information within each sliding window size. On the contrary, the Prophet model can suppress the noisy and reconstruct data based on the contextual spectral information in former bands. In addition, from Fig. 3.1, we can find that the Prophet model without Seasonality shows better results, i.e., higher interclass Kullback-Leibler divergence and lower intraclass Kullback-Leibler divergence in most cases. This may be due to that it is difficult to use the periodic Seasonality settings to characterize the complicated non-periodic changes in HSI spectra. Thus, in this chapter, we use the Prophet model without Seasonality for the further feature extraction and data classification.

3.3 The proposed Approach

The flowchart of the proposed SMP approach is depicted in Fig. 3.2, which has three main stages, i.e., superpixelwise spatial constrained smoothing, superpixelwise multiscale Prophet model based feature extraction, and superpixelwise HSI classification and fusion. Detailed implementation of these three stages is presented as follows.

3.3.1 Superpixelwise Spatial Segmentation and Smoothing

In general, adjacent pixels in HSI often share the similar spectral profiles because of the same surface material. Through superpixelwise segmentation, these pixels can be grouped to one region (superpixel) whilst the whole image is segmented into homogeneous regions with adaptively determined sizes and shapes. To ease the computational cost, the PCA is applied onto the original HSI dataset to extract the first three principal components, which contains the most useful information of input data [46], to form a pseudocolour image. The SLIC [156] method is then selected and applied to this pseudocolour image for superpixelwise segmentation of the HSI, as the SLIC can produce accurate boundary adherence yet with a low computational complexity [77].
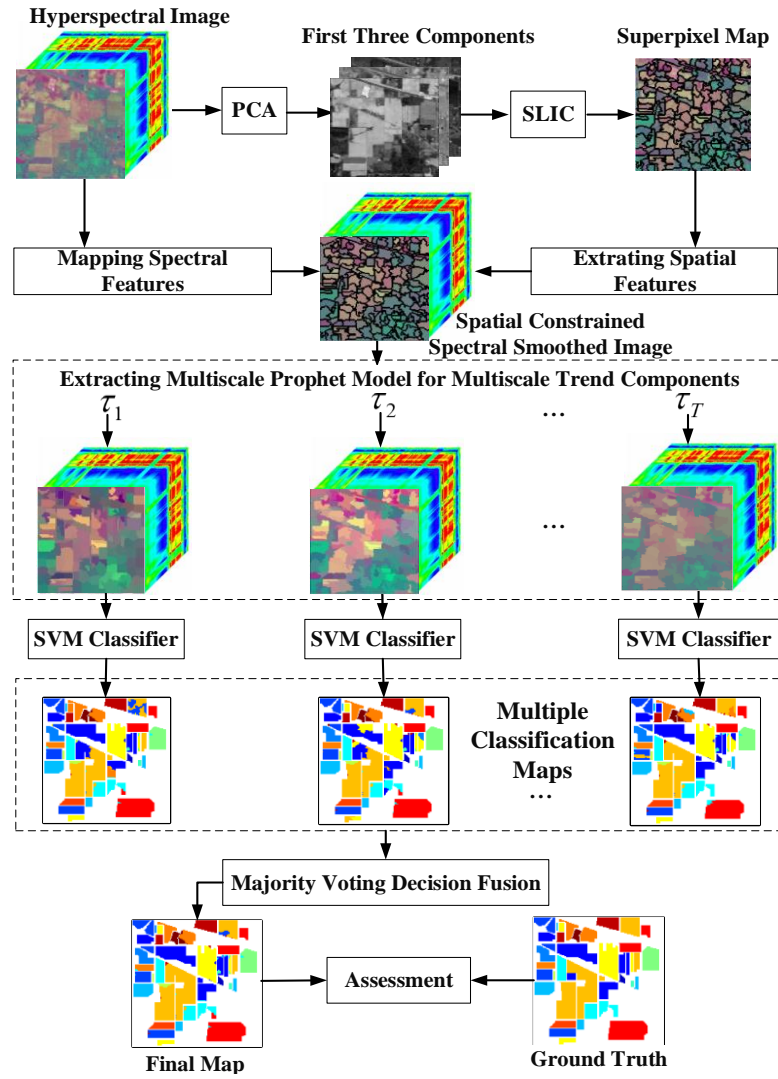
Fig. 3.2 The flowchart of the proposed SMP method.

Specifically, the SLIC starts with k initial cluster centres distributed on an evenly spaced grid, where k is the desired number of superpixels. It clusters on a square region sized of $2R \times 2R$ around the centres, where $R = \sqrt{n/k}$ denotes the segmentation scale, and n is the total number of pixels of the HSI. For measuring the homogeneity of a superpixel, a distance between two pixels $Dist(i, j)$ is defined, which includes the spectral distance to measure the spectra similarity and the spatial distance to estimate the regularity, proximity and compactness of these two pixels, respectively:

$$Dist(i,j) = \sqrt{\sum_{d=1}^{D}(x_{i,d} - x_{j,d})^2 + (G/R^2)\left((p_i - p_j)^2 + (q_i - q_j)^2\right)} \qquad (3.8)$$

51

where the spatial coordinates of the two pixels i and j are (p_i, q_i) and (p_j, q_j); their intensity values in the d-th band are denoted as $x_{i,d}$ and $x_{j,d}$, where $1 \leq d \leq D$, and D is the total number of bands; G is a geometric factor to balance the relative importance between the spectral and spatial features.

For each superpixel in the generated segmentation results of the superpixel maps, the location indices of all its pixels will be recorded and mapped to all the spectral bands, resulting in non-overlapping 3-D superpixels [74]. In this way, each superpixel contains a group of adjacent pixels in D dimensions. Afterwards, as shown in Fig.3.1, superpixelwise spatially constrained image smoothing is employed to remove the noise. Specifically, for each spectral band, the mean value of all pixels within the superpixel is taken as the value for that superpixel. In other words, superpixelwise mean spectral vectors are calculated to replace all pixels within each superpixel.

With the superpixelwise image smoothing, the spatial features are incorporated. More importantly, the proposed multiscale prophet model will only need to be applied to the mean spectral vector of each superpixel, which can significantly improve the efficiency of the following-on analysis.

3.3.2 Superpixelwise Multiscale Prophet Model

The Prophet model without the Seasonality is used for the further image processing. Specifically, for the k-th superpixel, let $SP_{k,d}$ denote its superpixelwise mean spectra at the d-th band, and the spectra data from all bands would form a vector SP_k. The trend component in the Prophet model $SP_{k,d}^g$ can be derived via Eq. (3.9) as:

$$SP_{k,d}^g = C_k / (1 + \exp(-r_d(d - m_d)))$$
(3.9)

where C_k is the carrying capacity of the k-th superpixel, which is determined based on the input spectra, i.e., the maximum value among the spectra of all bands, $C_k = \max_{d \in \{1,\ldots,D\}} SP_{k,d}$. For better capturing the statistical spectral-spatial structures in HSI

throughout the whole bands, we define each band as a changepoint. This can help to extract the local shifts of the superpixelwise spectral profile (the spectrum of all bands for the selected superpixel) among consecutive bands. Based on the Eqs. (3.3-3.5), the r_d and m_d in HSI data can be calculated.

During this process, as explained in Eq. (3.3), the factor τ significantly affects the value of r in each pair of consecutive bands, which further determines the magnitude of output trend components. That is, a large τ leads to the derived trend components overfitting while a small τ causes trend components under-fitting with the input superpixelwise spectral profile. In other words, the parameter τ determines the informativeness and noise level of the input data. Generally, the noise level varies throughout the hyperspectral bands, which is also correlated to sensor characteristics, image contents and weather conditions whilst the image is acquired [157].

Taking one pixel from the Salinas dataset [20] as an example, Fig. 3.3 shows the extracted trend signals under different values of τ, indicating the effect of various noise levels on the derived features. The trend function with a larger τ generates more similar estimates to the original data, although it may risk of potential overfitting. In essence, for HSI data with a low-SNR, smaller τ values can remove most of the noisy content. However, if τ is too small, important characteristics of the spectral profile may be lost. Thus, if the dataset has a high-SNR and τ is too small, this can bring about the loss of discriminating information in the samples. Besides, it also shows that the Prophet model can derive the informative trend from the HSI data, which is robust to the noisy content. This will be further validated in Section 3.5.

For the noisy HSI data, in real cases the signal and noise ratio varies differently in each band [157]. Therefore, it is a challenging or even impossible task to estimate an optimal scale of τ for the trend components for all the bands. To tackle this challenge, a multiscale approach is adopted in our SMP framework, where a set of τ values are used, $\tau = \{\tau_1, \tau_2, ..., \tau_T\}$, representing different scales, where T is the number of scales. For various values of τ, in total T trend components can be extracted from the smoothed mean spectral vector of each superpixel. These are then taken as multiscale

features of the HSI for data classification in the next stage, where the Prophet R package is used for implementation in our experiments [158].
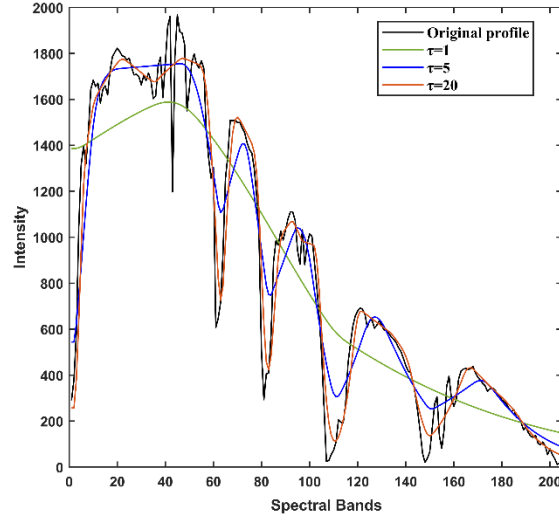
Fig. 3.3 The original and derived (by the Prophet model) profiles with different τ values for a pixel selected from the Salinas scene.

3.3.3 Superpixelwise HSI Classification and Decision Fusion

At a given scale, the trend components extracted from the Prophet model can be taken as the feature for the corresponding superpixel to produce a superpixelwise classification map. For T scales, we will have T classification maps, denoted as $\boldsymbol{M} = \{M_1, M_2, ..., M_T\}$. The final classification map Mf is determined by majority voting, i.e., the label that has the maximum number of appearances within $\boldsymbol{M}$:

$$Mf = \arg\max_{l=1,...,L} \sum_{t=1}^{T} F(M_t, l) \tag{3.10}$$

where l represents the possible class label in a HSI, and F is an indicator function given by $F(i, j) = \begin{cases} 1 \text{ if } i = j \\ 0 \text{ otherwise.} \end{cases}$

3.4 Experimental Settings and Datasets Description

For performance assessment, three publicly available HSI datasets are used in this chapter. The descriptions of the datasets and the experimental settings as well as some

54

ablation studies are presented in detail as follows.

3.4.1 Datasets

Three publicly available datasets are used in the experiments including the Airborne Visible/Infrared Imaging Spectrometer (AVIRIS) scenes Indian Pines and Salinas Valley, as well as the Reflective Optics System Imaging Spectrometer (ROSIS) scene Pavia University. Details of these datasets are given in Appendix A.

The Indian Pines [159] contains 145×145 pixels with 220 spectral bands. Twenty water absorption bands (104-108, 150-163 and 220) are often discarded [160] to get the corrected datasets. There are 16 manually defined land-cover classes, which are mostly different kinds of crops. The Salinas datasets [161] has 512×217 pixels and 224 spectral bands. Similarly, twenty water absorption bands are usually discarded. The corresponding ground-truth map also has 16 classes. The Pavia University dataset [162], namely PaviaU in this chapter, contains 114 spectral bands and 610×340 pixels. The available number of bands is reduced from 114 to 103 to avoid the effects of water absorption. The ground truth has nine classes of land covers.

3.4.2 Experimental Settings

For performance evaluation, two groups of experiments are designed, using respectively the uncorrected HSI dataset (without removing any bands), and the corrected dataset (with the noisy and water absorption bands removed). This is to validate the robustness of our SMP as most of the existing approaches only work well on the corrected HSI datasets.

First, comparison analysis is conducted and benchmarked with six state-of-the-art spectral-spatial HSI classification methods, using both the corrected and uncorrected HSI images. These include two signal decomposition-based methods, 2D-EMD [163] and 2D-SSA [20], the multiscale superpixel-based method, MSP-SVMsub [77], an MRF weighted spatial-spectral classifier, SMLR-SpATV [73] and two superpixelwise low rank representation based denoising techniques, SS-LRR [75] and fast superpixel based subspace low rank learning method (FS^{2}LRL) [82], which exhibited superiority in directly classifying the uncorrected HSI data. Besides, the approach to apply the

55

SVM classifier on the raw spectral profiles of HSI for classification, denoted as SVM-spe, is taken as the baseline.

Here, the efficacy of different strategies in SMP is also evaluated, i.e., the superpixelwise spatial segmentation and smoothing, and the superpixelwise multiscale Prophet model. Concretely, two cases are included: (1) SMP with only the superpixelwise segmentation/smoothing but not the multiscale Prophet model, denoted as SP-SVM, and (2) the proposed SMP. In addition, the baseline SVM-spe is also compared as one option of SMP yet without the above two strategies. In addition, our SMP is also compared with some deep learning approaches.

The parameter settings of all involved methods are summarized in Table 3.1. As for the proposed SMP, the optimal superpixel segmentation scale R is set to 150, 600 and 100 for Indian Pines, Salinas and PaviaU datasets, respectively, according to the ablation study in Section 3.4.3.1. As for the scale τ of the Prophet model, it varies within the range of $\{1, 5, 10, 15, 20, 25, 30, 35\}$ in different permutations and combinations. For balancing the accuracy and efficiency, the optimal set of $\{5, 10, 20, 25, 30\}$ is employed based on the ablation study in Section 3.4.3.2. The base rate r_0 and the base offset value m_0 are set by using Stan's L-BFGS in the Prophet R package by determining a maximum a *posteriori* estimate [32]. For SVM, the LIBSVM library is utilized for implementing multiclass classification [164, 165]. According to [166, 163], the Gaussian radial basis function (RBF) is employed, where the kernel factor and penalty parameter are optimally determined via a grid search to 0.125 and 1024, respectively. To ensure a fair comparison, we keep the SVM parameters consistent in all experiments. The other parameters for the benchmarking approaches are set according to their recommended default values [25] as shown in Table 3.1.

To reduce the random discrepancies and avoid systematic errors, all experiments are independently run ten times. In each run, the training sets are randomly selected from the corresponding dataset, i.e., training samples are individually selected from the corrected and uncorrected datasets. To fully evaluate the performance of these methods, experiments are also conducted with different numbers of training samples. In

particular, we mainly concern the problem of a small training set. Hence, the number of selected samples m varies within $\{5, 10, 15, 20, 25, 30\}$ for each land cover class in the training set via stratified sampling. If the total number of samples within the land cover class is less than 30, such as grass/pasture-mowed and oats in Indian Pines, 50% of samples in each class will be used for training [167]. The rest samples of each class are used as the testing samples. The number of samples in each class for different datasets is listed in detail in Figs. A.1.1, A.1.2 and A.1.3 in Appendix 1.

In addition, the overall accuracy (OA), Kappa coefficient (κ) and average accuracy (AA) are used for quantitative evaluation of the classification results. The OA denotes the ratio of the number of correctly classified samples for all classes to the total number of samples. The AA refers to the average percentage of correctly labelled samples for each class. For Cl classes in one dataset, supposing the number of correctly classified samples is Sc and the total number of samples for each class is St, the OA and AA are calculated based on the following equations.

$$OA = \frac{\sum_{i=1}^{Cl} Sc_i}{\sum_{i=1}^{Cl} St_i} \tag{3.11}$$

$$AA = \frac{1}{Cl} \sum_{i=1}^{Cl} \frac{Sc_i}{St_i} \tag{3.12}$$

The Kappa coefficient is a measure for the overall classification performance compared to values assigned by chance [168]. It is calculated as follows:

$$\kappa = \frac{OA - p_e}{1 - p_e} \tag{3.13}$$

where p_e is the proportion agreement occurring by chance. It takes value from 0 to 1. The higher the kappa coefficient, the more accurate the classification is.

All involved approaches are implemented using the Matlab 2018a platform on a computer with an Intel (R) Core (TM) i7-8700 CPU (3.20 GHz) and 16.0 GB of memory. The Prophet model is implemented on the R 3.5.3.

Table 3.1 List of parameter settings for our proposed SMP framework and other benchmarking approaches

Method	Indian Pines	Salinas	PaviaU
SVM-spe	N/A	N/A	N/A
2D-EMD	Stop threshold: 0.2, IMF Grouping (IMFG): 1-3rd	Stop threshold: 0.2, IMF Grouping (IMFG): 1-4th	Stop threshold: 0.2, IMF Grouping (IMFG): 1-4th
2D-SSA	Window size: 10×10, EVG: 1st	Window size: 40×40, EVG: 1-2nd	Window size: 5×5, EVG: 1-2nd
SMLR-SpATV	Smoothness parameter: 2	Smoothness parameter: 2	Smoothness parameter: 2
MSP-SVMsub	Superpixel number: [5, 10, 15, 25, 50, 75, 100]	Superpixel number: [5, 10, 15, 25, 50, 75, 100]	Superpixel number: [5, 10, 15, 25, 50, 75, 100]
SS-LRR	Superpixel number: 40	Superpixel number: 40	Superpixel number: 190
FS^{2}LRL	Subspace dimension: 10 Superpixel number: 100 Sparse parameter: 0.13 Fidelity parameter: 0.040	Subspace dimension: 10 Superpixel number: 100 Sparse parameter: 0.13 Fidelity parameter: 0.040	Subspace dimension: 10 Superpixel number: 100 Sparse parameter: 0.13 Fidelity parameter: 0.040
Proposed SMP	τ : [5, 10, 20, 25, 30], Superpixel scale: 150	τ : [5, 10, 20, 25, 30], Superpixel scale: 600	τ : [5, 10, 20, 25, 30], Superpixel scale: 100

3.4.3 Parameter Analysis

3.4.3.1 Segmentation scale

The scale of superpixel segmentation is a key parameter that affects the generated superpixels and the classification results [169]. Here, the optimal scale values for the three datasets are tested. The Indian Pines and PaviaU datasets possess more complicated land covers than Salinas dataset. A large superpixel scale is suitable for Salinas dataset. Therefore, scales are respectively set to [50, 75, 100, 125, 150, 175, 200] for the Indian Pines and PaviaU datasets, and [450, 500, 550, 600, 650, 700, 750] for the Salinas dataset. Then the classification result of the proposed method at different superpixel scale is evaluated. Note that the numbers of training and test samples are set the same as aforementioned in Section 3.4.2.

For balanced performance assessment of each class, we adopt the mean AA over ten independent runs for tuning the scale parameters. Fig. 3.4 illustrates the AA values of the proposed SMP using different superpixel scales on the three corrected datasets, under various numbers of training samples per class. In general, more training samples will lead to better classification results in terms of higher AA values. However, it seems the training size of 20 yields overall best results in the corrected Salinas dataset, whilst for corrected Indian Pines and PaviaU datasets the best results are generated when the training samples is 30 in our experiments. For a given training size, the segmentation scale in SMP determines the homogeneity within a local region and thus affects the classification accuracy. An appropriate scale value can generate more accurate object boundaries. As seen in Fig. 3.4, the best superpixel scales for Indian Pines, Salinas and PaviaU are found to be 150, 600 and 100, respectively, as they can help to generate the highest AA for a given number of training samples. As a result, these are used in the remaining experiments for superpixel based segmentation of the three images.

(a)　　　　　　　　　　(b)　　　　　　　　　　(c)
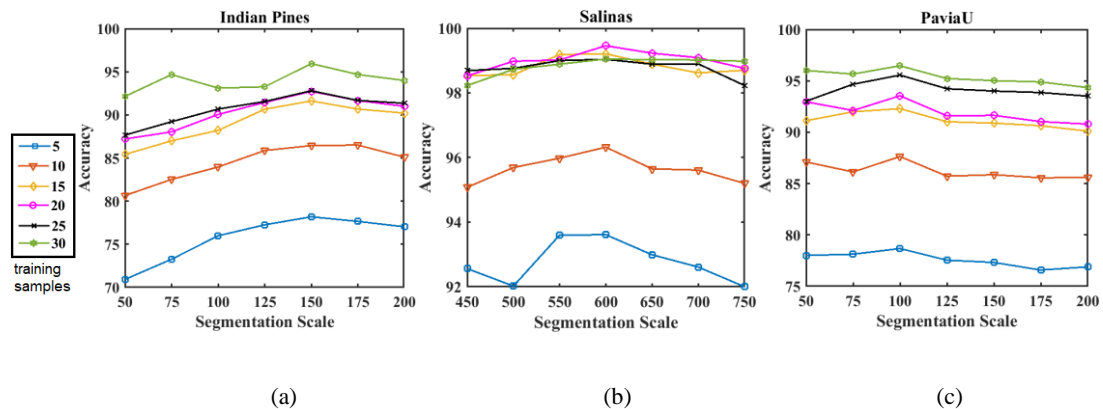
Fig. 3.4 Mean AA of MSP with different superpixel segmentation scales for three datasets of Indian Pines (a), Salinas (b) and PaviaU (c).

3.4.3.2 The parameter τ

In order to test the optimal sets of parameter τ on three datasets, the achieved class-based accuracy and OA of the proposed method with varying τ within the range of $\{1, 5, 10, 15, 20, 25, 30, 35\}$ are analysed in this section and shown in Fig. 3.5. The number of training samples are set to 5 for each land cover for all tests.

59
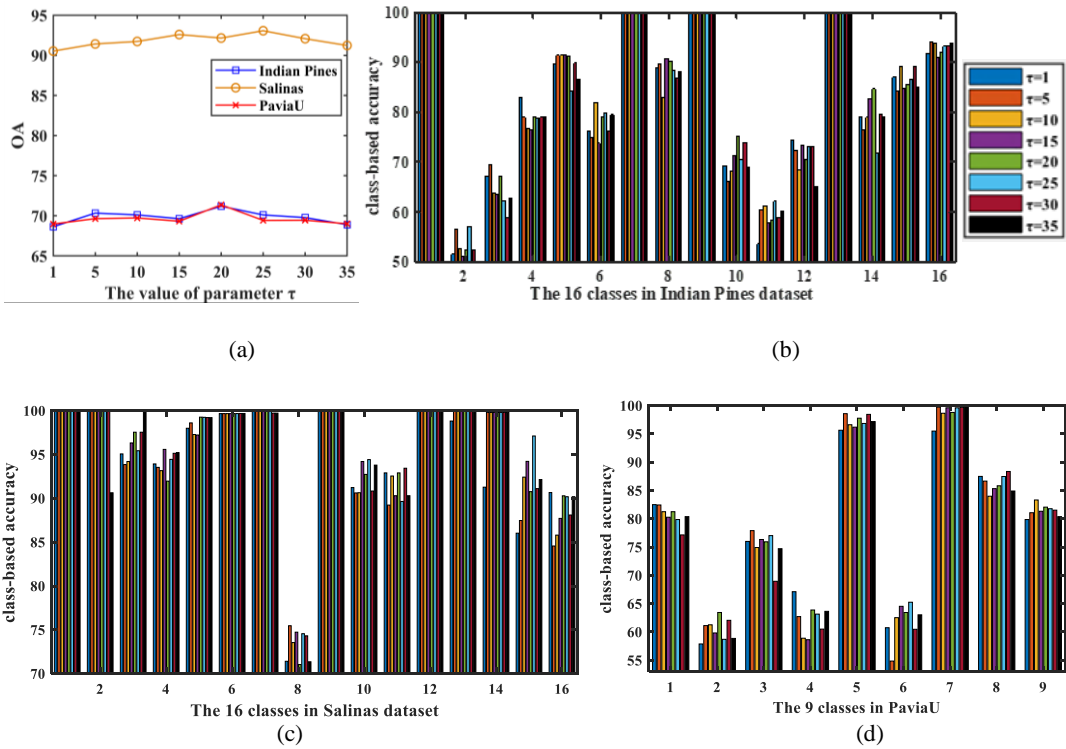
Fig. 3.5 The effect of the parameter τ of MSP to the OA (a) and class-based classification accuracy on datasets of Indian Pines (b), Salinas (c) and PaviaU (d).

From Fig. 3.5 (a), it is clear that the value of parameter τ in the range [5,30] enables the SMP to achieve better classification results in terms of higher OA values. As for the class-based classification performance, on the Indian Pines dataset shown in Fig. 3.5 (b), the value 5, 10, 20 and 25 for parameter τ leads to the best accuracy in the three classes (the classes #3, #5 and #16), two classes (the classes #6 and #15), two classes (the classes #10 and #14) and two classes (the class #2 and #11), respectively. On the corrected Salinas dataset, apart from the classes #1, #9 and #12, where the 100% accuracy of SMP are produced on all cases, the best results are generated when the parameter τ equal to 20 and 25, in which SMP achieve the highest accuracy in three classes, respectively. The proposed SMP also realize better performance when parameter τ are set to 5, 15 and 30. As seen in Fig. 3.5 (d), the best value of parameter τ for PaviaU are found to be 1 and 5, as they can help to generate the highest accuracy on the classes #1 and #4, and #3 and #5, respectively. The value 10, 20, 25, 30 and 35 for parameter τ also lead to the best classification performance on the classes #9, #2, #6, #8 and #7, respectively. To sum up, considering the OA and class-based

performance of SMP on three datasets, we employ the set of $\{5, 10, 20, 25, 30\}$ for the parameter τ in this chapter.

3.5 Results and discussion

In this section, qualitative and quantitative results from the three HSI datasets are presented for performance assessment of the proposed SMP approach. Relevant results from uncorrected and corrected HSI datasets as well as the efficacy of different strategies in SMP and further comparison with several deep learning based approaches are reported in detail as follows.

3.5.1 Results from the Indian Pines Dataset

Indian Pines dataset is heavily corrupted by noise and water absorption [82]. Here, corrected and uncorrected Indian Pines datasets, where noisy and water absorption bands are removed or kept, respectively, are used for quantitative and qualitative performance evaluation as detailed below.

(1) Quantitative evaluation

For quantitative evaluation, the overall accuracy (OA) and the Kappa coefficient (κ) are utilized. The proposed SMP approach has been compared with 2D-EMD, 2D-SSA, SMLR-SpATV, MSP-SVMsub, SS-LRR, FS^{2}LRL, SVM-spe, and SP-SVM (only use superpixelwise smoothing yet without Prophet model). Relevant results are reported in Table 3.2. Note that the best results in each row are highlighted in bold for comparison.

First of all, all the results in Table 3.2 are positively correlated with the increasing number of training samples. With the introduced spatial features, 2D-EMD, 2D-SSA and SMLR-SpATV have all yielded better classification results than SVM-spe, in which no spatial features are used. With superpixel based smoothing, more effective spatial features can be extracted thus the further improved results from MSP-SVMsub. This superior performance is mainly due to the utilization of adaptive local structures in superpixelwsie segmentation and smoothing, which has enhanced the consistency of the spectral features better than using a fix-sized window. Besides, SS-LRR and

61

FS^{2}LRL also improve the classification accuracy due to the effect of their denoising operations. Overall, the proposed SMP remains the best and constantly produces the highest accuracy in terms of OA and $\mathcal{K}$. More specifically, by analysing the results obtained by SVM-spe, SP-SVM and SMP, we can find that the proposed superpixelwise smoothing and multiscale Prophet modelling has significantly improved the classification accuracy on the corrected and uncorrected Indian Pines dataset. Consequently, SMP surpasses all others at different training sizes, which has validated the efficacy of our proposed SMP approach in addressing the Hughes phenomenon under very limited training samples.

Table 3.2 The OA (%) and $\mathcal{K}$ (in parentheses) of different strategies in SMP under various numbers of training samples for the Indian Pines dataset with or without removing the noisy and water absorption bands

Samples	Dataset	SVM-spe	2D-EMD	2D-SSA	SMLR-SpATV	MSP-SVMsub	SS-LRR	FS^{2}LRL	SP-SVM	SMP
5	Uncorrected	41.77 (0.35)	54.16 (0.49)	64.70 (0.61)	54.69 (0.50)	62.39 (0.58)	63.51 (0.59)	55.98 (0.51)	73.02 (0.70)	**78.76 (0.76)**
	Corrected	46.85 (0.41)	57.71 (0.53)	61.72 (0.57)	56.08 (0.52)	68.09 (0.68)	60.95 (0.56)	56.13 (0.51)	70.44 (0.67)	**78.18 (0.76)**
10	Uncorrected	49.80 (0.44)	67.35 (0.63)	74.77 (0.72)	73.63 (0.70)	82.01 (0.80)	75.63 (0.73)	67.30 (0.63)	82.40 (0.80)	**89.79 (0.88)**
	Corrected	54.91 (0.50)	71.88 (0.68)	72.33 (0.69)	73.95 (0.71)	83.57 (0.81)	74.26 (0.71)	69.60 (0.66)	81.84 (0.80)	**86.44 (0.85)**
15	Uncorrected	54.15 (0.49)	75.24 (0.72)	81.95 (0.80)	80.12 (0.78)	85.30 (0.83)	81.50 (0.79)	73.88 (0.71)	89.32 (0.87)	**92.35 (0.91)**
	Corrected	59.97 (0.55)	79.45 (0.77)	78.12 (0.75)	80.28 (0.78)	87.69 (0.86)	81.22 (0.79)	75.02 (0.72)	87.90 (0.86)	**91.62 (0.91)**
20	Uncorrected	57.22 (0.52)	79.77 (0.77)	84.87 (0.83)	83.10 (0.81)	88.99 (0.88)	85.11 (0.83)	77.64 (0.75)	91.81 (0.91)	**94.36 (0.94)**
	Corrected	63.44 (0.59)	84.16 (0.83)	81.65 (0.79)	83.12 (0.81)	90.47 (0.89)	83.64 (0.81)	78.95 (0.76)	89.10 (0.88)	**92.73 (0.92)**
25	Uncorrected	58.98 (0.54)	82.71 (0.80)	87.44 (0.86)	86.49 (0.85)	91.04 (0.90)	87.11 (0.85)	79.92 (0.77)	92.51 (0.91)	**94.94 (0.94)**
	Corrected	65.73 (0.62)	86.54 (0.85)	84.86 (0.83)	86.60 (0.85)	91.92 (0.91)	86.01 (0.84)	81.64 (0.79)	92.35 (0.91)	**92.80 (0.91)**
30	Uncorrected	61.29 (0.57)	85.15 (0.83)	89.03 (0.88)	88.05 (0.86)	93.12 (0.92)	87.85 (0.86)	82.35 (0.80)	93.37 (0.92)	**96.22 (0.96)**
	Corrected	67.73 (0.64)	88.53 (0.87)	86.25 (0.84)	88.74 (0.87)	93.70 (0.93)	87.99 (0.86)	82.43 (0.80)	93.35 (0.92)	**95.95 (0.95)**

When comparing the performance of each method on corrected and uncorrected Indian Pines dataset, we can find that in most cases, SVM-spe, 2D-EMD, SMLR-SpATV, MSP-SVMsub and FS^{2}LRL achieve better results on corrected dataset. The 2D-SSA, SP-SVM and the advanced noise reduction method, SS-LRR, can effectively remove the effect of noise while preserving the spectral features. As a result, they have achieved higher accuracy on the uncorrected HSI. For our proposed SMP approach, in almost all cases the results on the uncorrected dataset have outperformed those from the corrected one, with a gain up to 3.35%. Thanks to the proposed superpixelwise smoothing and multiscale Prophet modelling, our SMP model can successfully suppress the noise and extract useful features from the low-SNR bands and water absorption bands. This has provided additional benefits for efficient and effective interpretation of HSI in an automatic way, as no extra work is needed to filter out those unwanted bands.

(2) Visual and class-based performance assessment

Although the superior performance of our SMP has been validated in quantitative assessment, here visual and class-based performance evaluation is used to show how exactly the classification errors has been reduced from the uncorrected dataset. We select the best performing three methods in Table 3.2 with 30 training samples per class, i.e., 2D-SSA, SMLR-SpATV and MSP-SVMsub, for further comparison.

For visual comparison, the classification maps from our approach and the three selected ones on both the uncorrected and corrected dataset are given in Fig.3.6, where black and magenta circles are used to mark respectively the correct and incorrect parts in the classification maps. In Table 3.3, class-by-class classification results are also compared using the OA, average accuracy (AA) and Kappa coefficient with 30 training samples per class are also given.

First of all, as shown in Table 3.3, SMP has achieved the best classification accuracy in 13 out of 16 classes on both the uncorrected and corrected datasets, which is significantly better than all other methods, especially in the classes 3, 5, 10 and 11 (*Corn-min till*, Grass/pasture *Soybeans-no till* and *Soybeans-min till*). Overall, the OA of SMP is about 3% and 2% higher than the second-best on the uncorrected and

corrected datasets, respectively. This has demonstrated again the efficacy of SMP on classification of the Indian Pines dataset with limited and unbalanced samples. Specifically, SMP, 2D-SSA and SMLR-SpATV consistently produce better results on the uncorrected dataset than the corrected one.

Table 3.3 Classification accuracy (%) of all involved methods for the Indian Pines data with 30 training samples per class.

	Uncorrected				Corrected			
Class	2D-SSA	SMLR-SpATV	MSP-SVMsub	SMP	2D-SSA	SMLR-SpATV	MSP-SVMsub	SMP
1	99.86	98.99	**100.00**	**100.00**	99.78	**100.00**	**100.00**	**100.00**
2	82.44	80.47	86.34	**92.55**	79.97	80.84	**94.56**	91.73
3	91.34	85.67	92.50	**98.68**	87.36	87.22	93.13	**98.68**
4	98.74	99.52	99.03	**100.00**	99.05	99.90	**100.00**	**100.00**
5	93.84	91.83	94.70	**100.00**	92.70	92.96	92.72	**100.00**
6	96.35	**98.75**	98.14	97.91	95.85	**99.49**	98.29	94.21
7	**100.00**	100.00	100.00	100.00	100.00	100.00	100.00	100.00
8	99.59	**100.00**	99.78	**100.00**	98.98	**100.00**	100.00	100.00
9	99.67	99.67	**100.00**	**100.00**	98.50	**100.00**	100.00	100.00
10	86.62	87.80	92.04	**97.72**	84.46	86.78	91.30	**97.75**
11	80.97	81.89	90.39	**94.46**	76.42	78.59	88.70	**91.85**
12	87.58	91.82	**93.07**	91.39	86.82	91.60	93.61	91.31
13	99.64	99.98	**100.00**	**100.00**	99.34	99.94	**100.00**	**100.00**
14	96.79	94.68	**97.89**	97.00	92.38	90.45	96.52	**99.46**
15	98.43	98.77	96.91	**100.00**	97.02	99.16	98.03	**100.00**
16	98.89	99.89	**100.00**	**100.00**	98.01	**100.00**	100.00	100.00
OA	89.03	88.74	93.12	**96.22**	86.25	87.59	93.70	**95.95**
$\mathcal{K}$	0.88	0.87	0.92	**0.96**	0.86	0.86	0.93	**0.95**
AA	94.42	94.36	96.30	**98.11**	92.92	94.18	96.68	**97.93**

As seen in Fig. 3.6, with the introduced spatial information, 2D-SSA and SMLR-SpATV have produced much smoother results as shown in Fig. 3.6 (c-f). However, the three classes *Corn-no till*, *Soybeans-min till* and *Soybeans-no till* are seriously misclassified with each other as highlighted in magenta circles. Therein 2D-SSA performs better in classifying these three classes on uncorrected datasets as shown in Fig. 3.6 (c). As for the SMLR-SpATV, it generates better visual results in Grass/trees on uncorrected data. However, both 2D-SSA and SMLR-SpATV fail to preserve detailed structures and fine object boundaries. In particular, several regularly shaped land covers are distorted due to the incorrect edge partitions. For example, there are

some geometrical distortions on the classified *Corn-no till* and *Soybeans-no till* using 2D-SSA and SMLR-SpATV as highlighted in magenta circles in Fig. 3.6 (c-f). With further introduced superpixel segmentation, MSP-SVMsub, has produced improved object boundaries, which is mainly owing to the homogeneous regions produced by SLIC. Though the aforementioned classification errors in Fig. 3.6 (c-f) are corrected to some extent, there are still several small misclassified regions, especially in the *Soybeans-min till* and *Soybeans-no till* regions as highlighted in Fig. 3.6 (g-h). This may be due to improper scale values used in multiscale superpixeling, owing to noise caused high intra-variations in the land cover classes. Comparing the classification maps between Fig. 3.6 (g) and (h), MSP-SVMsub achieves comparably similar results on both the uncorrected and corrected datasets.

Fig. 3.6 Classification maps on the Indian Pines data (30 samples per class): (a) False colour image (R: 831nm, G: 657nm, B: 557nm), (b) Ground truth in 16 classes, (c) 2D-SSA on uncorrected data, (d) 2D-SSA on corrected data, (e) SMLR-SpATV on uncorrected data, (f) SMLR-SpATV on corrected data, (g) MSP-SVMsub on uncorrected data, (h) MSP-SVMsub on corrected data, (i) SMP on uncorrected data and (j) SMP on corrected data.

With regard to our SMP, it has generally produced much smoother and accurate maps and more homogeneous regions compared to its counterparts. As highlighted in the black circles in Fig. 3.6 (i-j), the complex objects with high intra-class variations can still be correctly classified by SMP. Here, SMP performs much better on uncorrected data when discriminating *Corn-no till* and *Soybeans-min till*, *Grass/trees* and *Woods*.

These visual results are consistent with the quantitative results in Table 3.3, which has validated again the efficacy of our SMP in noise-robust feature mining and HSI classification.

3.5.2 Results from the Salinas Dataset

Similarly, the Salinas dataset with or without noisy and water absorption bands, denoted as uncorrected Salinas and corrected Salinas, respectively, are employed for performance evaluation. Relevant results under different numbers of training samples are reported in Table 3.4 for quantitative comparison.

Table 3.4 The OA (%) and K (in parentheses) of different strategies in SMP under various numbers of training samples for the Salinas dataset with or without removing the noisy and water absorption bands

Samples	Dataset	SVM-spe	2D-EMD	2D-SSA	SMLR-SpATV	MSP-SVMsub	SS-LRR	FS^{2}LRL	SP-SVM	SMP
5	Uncorrected	79.79	80.22	82.55	86.54	91.73	84.12	85.64	90.63	**95.40**
		(0.78)	(0.78)	(0.81)	(0.85)	(0.91)	(0.82)	(0.84)	(0.90)	**(0.95)**
	Corrected	80.99	80.70	84.31	86.42	89.18	82.46	83.85	90.94	**93.61**
		(0.79)	(0.79)	(0.83)	(0.85)	(0.88)	(0.81)	(0.82)	(0.90)	**(0.93)**
10	Uncorrected	83.53	83.76	91.03	90.77	95.70	87.33	89.35	95.58	**98.27**
		(0.82)	(0.82)	(0.90)	(0.90)	(0.95)	(0.86)	(0.88)	(0.95)	**(0.98)**
	Corrected	83.62	84.05	91.36	90.77	93.30	87.08	88.93	**96.88**	96.32
		(0.82)	(0.82)	(0.90)	(0.90)	(0.93)	(0.86)	(0.88)	**(0.96)**	(0.96)
15	Uncorrected	85.18	85.36	93.98	92.34	96.09	90.52	91.55	98.05	**99.01**
		(0.84)	(0.84)	(0.93)	(0.92)	(0.96)	(0.89)	(0.91)	(0.98)	**(0.99)**
	Corrected	84.53	85.47	93.46	92.98	96.46	88.97	91.39	98.43	**99.21**
		(0.83)	(0.84)	(0.93)	(0.91)	(0.96)	(0.88)	(0.90)	(0.98)	**(0.99)**
20	Uncorrected	86.27	86.03	95.54	92.89	97.81	92.23	93.51	98.14	**99.60**
		(0.85)	(0.85)	(0.95)	(0.92)	(0.98)	(0.91)	(0.93)	(0.98)	**(0.99)**
	Corrected	86.38	86.33	95.53	93.12	97.49	90.71	93.02	98.67	**99.46**
		(0.85)	(0.85)	(0.95)	(0.92)	(0.97)	(0.90)	(0.92)	(0.99)	**(0.99)**
25	Uncorrected	86.90	86.98	96.22	93,41	97.82	93.25	93.70	98.64	**99.60**
		(0.85)	(0.86)	(0.96)	(0.93)	(0.98)	(0.91)	(0.93)	(0.98)	**(1.00)**
	Corrected	87.00	87.03	96.20	93.40	98.08	91.62	93.67	98.78	**99.04**
		(0.86)	(0.86)	(0.96)	(0.93)	(0.98)	(0.91)	(0.93)	(0.99)	**(0.99)**
30	Uncorrected	87.46	87.36	97.05	94.16	98.59	93.03	94.45	98.81	**99.60**
		(0.86)	(0.86)	(0.97)	(0.93)	(0.98)	(0.92)	(0.94)	(0.99)	**(1.00)**
	Corrected	87.61	87.59	97.03	93.91	98.17	92.14	94.37	98.84	**99.05**
		(0.86)	(0.86)	(0.97)	(0.93)	(0.98)	(0.91)	(0.94)	(0.99)	**(0.99)**

(1) Quantitative evaluation

In Table 3.4, the similar factual conclusions can be made as from the Indian Pines dataset. The difference here is that the addition of various spatial features contributes less than that on the Indian Pines dataset. The possible reason is the high intra-class homogeneity caused by low-level noise and geometrically structured simple agricultural objects in the image. Overall, the proposed SMP remains the best and constantly produces the highest OA and K except one occasion on the corrected dataset with 10 training samples per class. In 5 out of 6 cases, SMP has better results on the uncorrected dataset than the corrected one. These results have clearly shown the efficacy of our SMP for HSI classification, which is again mainly due to combining superpixelwise segmentation and smoothing along with the multiscale Prophet model based noise-robust feature mining.

When comparing the OA and K of each method on the corrected and uncorrected Salinas datasets, in most cases, SVM-spe, 2D-EMD and SP-SVM generate better results on the corrected Salinas than the uncorrected one. However, 2D-SSA performs better on the uncorrected Salinas when the number of training samples per class is larger than 15. As for the SMLR-SpATV and MSP-SVMsub, they have inconsistent results though in more cases achieve better results on the uncorrected dataset. The two denoising approaches, SS-LRR and FS^{2}LRL, and our proposed SMP produce better classification performance on uncorrected Salinas in almost all cases.

By comparing SVM-spe, SP-SVM and SMP, it is obvious that the superpixelwise smoothing fails to suppress the noise in the Salinas dataset, whereas multiscale Prophet modelling has successfully filled the gap to avoid the effects of noisy content in low-SNR bands and water absorption bands. This validates the efficacy our method in noise-robust feature extraction and HSI classification.

(2) Visual and class-based performance assessment

Furthermore, results of class-by-class classification from 2D-SSA, SMLR-SpATV, MSP-SVMsub and SMP with 30 training samples per class are given in Table 3.5, along with the classification maps shown in Fig. 3.7 for visual comparison. In Table

67

3.5, the proposed SMP produces the best results in 12 and 13 out of 16 land cover classes on the uncorrected and corrected dataset, respectively. Surprisingly, on these two datasets, 2D-SSA has generated similar good results as MSP-SVMsub, even without superpixel based spatial constraints.

Table 3.5 Classification accuracy (%) of all involved methods for the Salinas data with 30 training samples per class.

Class	Uncorrected				Corrected			
	2D-SSA	SMLR-SpATV	MSP-SVMsub	SMP	2D-SSA	SMLR-SpATV	MSP-SVMsub	SMP
1	98.55	99.97	99.95	**100.00**	99.29	99.96	99.70	**100.00**
2	98.02	**100.00**	99.22	**100.00**	97.73	**100.00**	99.73	**100.00**
3	99.56	95.71	99.95	**100.00**	99.57	95.95	**100.00**	**100.00**
4	97.30	98.97	98.83	**99.85**	96.51	98.89	98.31	**100.00**
5	97.79	**98.99**	97.51	98.87	97.86	98.73	98.04	**98.87**
6	98.35	**100.00**	97.17	99.67	97.78	**100.00**	99.31	99.68
7	97.54	**99.97**	99.61	99.92	97.44	**99.97**	99.66	99.92
8	93.36	85.66	98.77	**99.04**	92.52	82.72	95.15	**96.38**
9	99.60	**100.00**	**100.00**	**100.00**	99.67	**100.00**	99.43	**100.00**
10	97.81	95.84	98.28	**98.85**	97.52	96.00	97.69	**98.83**
11	98.58	99.90	**100.00**	98.16	98.47	**99.92**	99.42	98.12
12	95.93	99.97	93.09	**100.00**	97.16	99.97	99.63	**100.00**
13	98.40	99.67	97.86	**100.00**	97.19	99.81	99.77	**100.00**
14	96.68	99.62	97.88	**99.81**	97.35	99.20	98.94	**99.81**
15	96.71	82.81	98.19	**100.00**	98.12	80.75	95.03	**100.00**
16	99.76	99.49	98.76	**100.00**	99.63	99.67	98.71	**100.00**
OA	97.05	94.16	98.59	**99.60**	97.03	93.27	97.77	**99.05**
K	0.97	0.93	0.98	**1.00**	0.97	0.93	0.98	**0.99**
AA	97.75	97.29	98.44	**99.64**	97.74	96.97	98.66	**99.48**

The great potential of 2D-SSA will be further investigated in the future. All the approaches in this subsection have achieved better OA on the uncorrected Salinas dataset when using 30 training samples per class. By using the information in water vapor absorption bands, 2D-SSA, SMLR-SpATV and MSP-SVMsub have improved the classification results in 9, 6 and 8 classes, respectively. SMP yields better accuracy in classes #8, #10 and #11 (*Grapes untrained*, *Corn senesced green weeds*, and *Lettuce romaine 4wk*) on uncorrected Salinas dataset than the corrected one.

Regarding the classification maps in Fig. 3.7, it is obvious that the proposed SMP algorithm can generate the smoothest results with higher geometric fidelity and more accurate boundaries on the uncorrected dataset as shown in Fig. 3.7(i). As for the land cover classes with high spectral and spatial similarity, such as *Vinyard untrained* and *Grapes untrained*, SMP can effectively characterize them on uncorrected dataset, seen in black circles in Fig. 3.7(i). On the contrary, all other approaches have produced severe confusion between these two classes on both corrected and uncorrected datasets, as highlighted by magenta circles in Fig. 3.7(c-h). These have clearly shown the added value of the recovered spectral information from the uncorrected dataset.
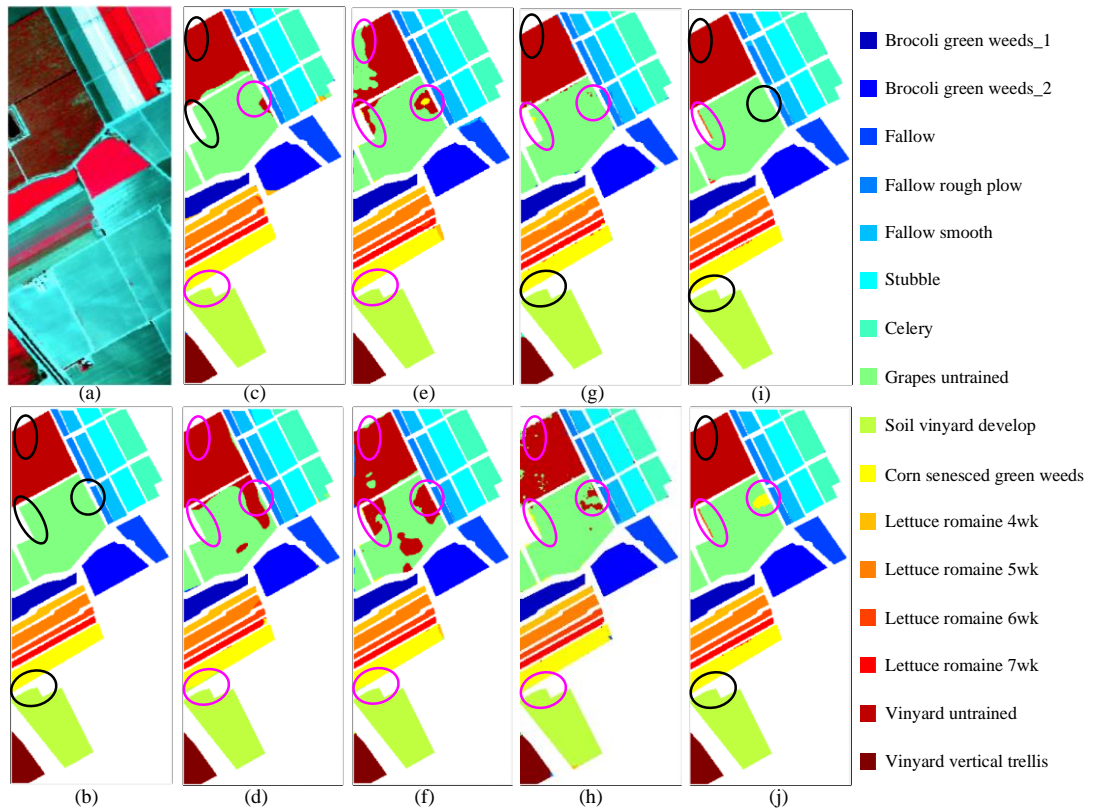
Fig. 3.7 Classification maps on the Salinas dataset (30 samples per class): (a) False colour image (R: 831nm, G: 657nm, B: 557nm), (b) Ground truth in 16 classes, (c) 2D-SSA on uncorrected data, (d) 2D-SSA on corrected data, (e) SMLR-SpATV on uncorrected data, (f) SMLR-SpATV on corrected data, (g) MSP-SVMsub on uncorrected data, (h) MSP-SVMsub on corrected data, (i) SMP on uncorrected data and (j) SMP on corrected data.

Besides, the misclassification between *Corn senesced green weeds* and *Soil vinyard develop* by 2D-SSA and SMLR-SpATV as shown in Fig. 3.7(c-f) are much reduced by the SMP (shown in Fig. 3.7(i-j)) and the MSP-SVMsub on uncorrected dataset, see in Fig. 3.7(g). This may be due to the introduced superpixel segmentation. When

69

comparing the classification maps between Fig. 3.7(c) and (d), Fig. 3.7(e) and (f), Fig. 3.7(g) and (h), it is clear that 2D-SSA, SMLR-SpATV and MSP-SVMsub have all produced better visual results on the uncorrected dataset. Overall, SMP has successfully and accurately classified most of the boundaries in the uncorrected Salinas dataset using a small number of training samples as shown in Fig. 3.7(i), which are consistent with the quantitative results given in Table 3.5.

3.5.3 Results from the PaviaU Dataset

In this subsection, the performance of our proposed SMP is further evaluated using the PaviaU dataset. As the uncorrected dataset is unavailable, we only work on the corrected dataset with the results given below.

(1) Quantitative evaluation

In Table 3.6, our proposed SMP is compared with SVM-spe, 2D-EMD, 2D-SSA, SMLR-SpATV, MSP-SVMsub, SS-LRR and FS^{2}LRL, where class-based classification results are also shown. Similarly, the best quantitative results are labelled in bold for clarity. As seen in Table 3.6, the proposed SMP has produced the best results in terms of the highest OA, K and AA, outperforming the second best by 2.65%, 3% and ~4%, respectively. Nevertheless, SMP produces the best results in 4 out of 9 classes, though other algorithms may have up to three best classified classes. (b)

Fig. 3.8 shows the classification results from the corrected PaviaU dataset using different numbers of training samples for all the involved algorithms. As seen, SMP still achieves the highest OA and K in all the experiments. With a lower number of spectral bands than the other two datasets, the Hughes effect in PaviaU dataset is not apparent [77]. As a result, spectral-spatial classification strategies have shown less contributions than those on the other two datasets. Nevertheless, the superpixel based approaches, MSP-SVMsub and SMP, still exhibit superior performance due to the preserved local homogeneous regions especially when the number of training samples is above 5. In general, the proposed SMP has again produced effective and reliable results on the PaviaU dataset.

Table 3.6 Classification accuracy (%) of all involved methods for the corrected PaviaU data with 30 training samples per class

Class	SVM-spe	2D-EMD	2D-SSA	SMLR-SpATV	MSP-SVMsub	SS-LRR	FS^{2}LRL	SMP
1	74.37	73.64	83.25	86.87	89.73	77.94	79.30	**95.65**
2	78.49	80.31	89.83	87.72	96.03	83.30	89.41	**99.25**
3	79.06	77.85	82.60	86.17	**98.89**	83.23	81.23	94.05
4	92.00	92.55	90.50	93.10	76.90	92.94	**93.64**	92.70
5	99.21	99.23	99.33	**100.00**	100.00	99.17	99.28	98.73
6	82.88	79.71	87.88	92.45	**99.02**	85.58	91.09	94.31
7	90.85	89.63	93.43	99.02	99.92	94.21	95.22	**100.00**
8	78.57	77.99	84.26	86.74	96.96	84.31	88.41	**97.82**
9	99.92	**99.94**	98.99	69.97	64.56	99.86	99.91	94.86
OA	80.85	81.05	88.40	88.71	93.82	84.69	88.57	**96.47**
K	0.75	0.76	0.85	0.85	0.92	0.80	0.85	**0.95**
AA	86.15	85.65	90.01	89.12	91.33	88.95	90.83	**95.27**
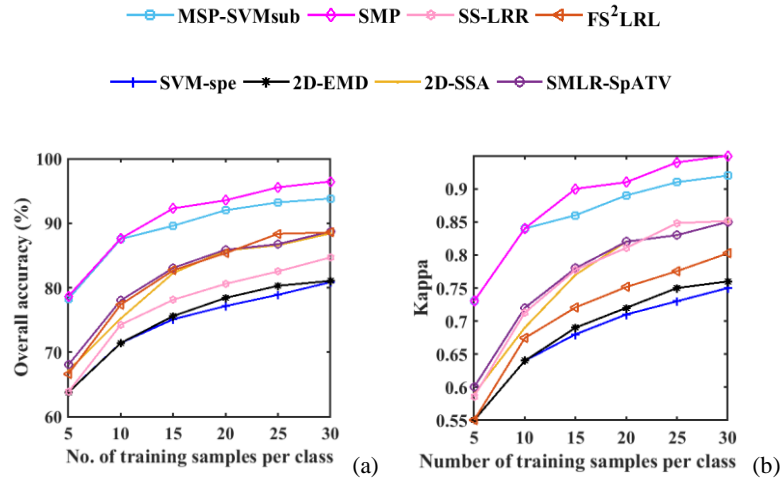
Fig. 3.8 Results from different approaches under various training samples for the corrected PaviaU dataset in terms of OA (a) and Kappa (b).

(2) Visual comparison

Visual comparison of the classification maps from our SMP and other comparing methods on the corrected PaviaU dataset are shown in Fig. 3.9, where black and magenta circles denote correct and incorrect parts in the classification maps for clarity. As illustrated in Fig. 3.9(c-j), *Meadows* are seriously confused with *Trees* or *Bare Soil* when they appear visually densely or sparsely. By combining spatial features in 2D-

SSA, SS-LRR, FS^{2}LRL and SMLR-SpATV, the noisy estimations in the maps of SVM-spe and 2D-EMD are dramatically reduced, and most of the remaining misclassifications are further corrected by MSP-SVMsub and SMP as highlighted in black circles in Fig. 3.9(e-j). These have also validated by the corresponding higher accuracy values on *Meadows* and *Trees* in Table 3.6. As for differing between *Self-Blocking Bricks* and *Gravel*, only SMP and MSP-SVMsub can discriminate these two classes to some extent as shown by the black circles in the Fig. 3.9(g) and (j) and also the quantitative results in Table 3.6. These are mainly owing to the modified subspace SVM classifier in MSP-SVMsub and the multiscale Prophet model in SMP for refined spectral feature mining. In addition, SVM-spe, SMLR-SpATV, MSP-SVMsub and SS-LRR all fail to classify some *Asphalt* edges closing to *Trees* as highlighted in magenta circles in Fig. 3.9(c, f-h). On the contrary, these two classes, affected by spectral mixture of surrounding pixels, are correctly classified by 2D-EMD, 2D-SSA, FS^{2}LRL and our proposed SMP.
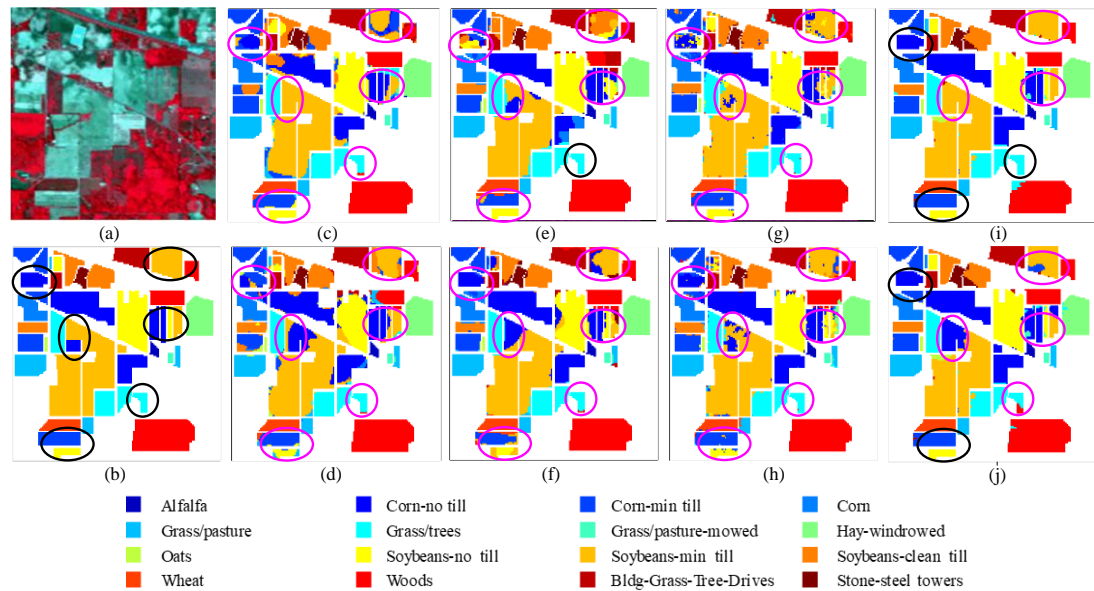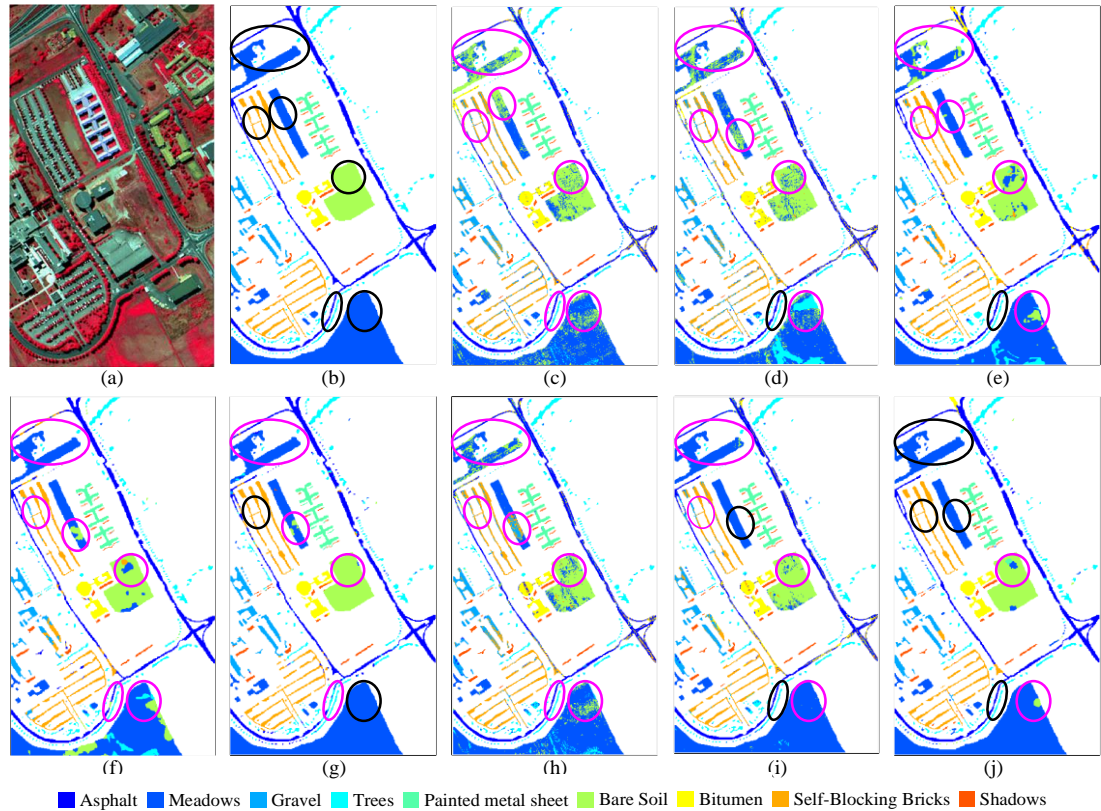

Fig. 3.9 Classification maps on the corrected PaviaU data (30 samples per class): (a) False colour image (R: 834nm, G: 650nm, B: 550nm), (b) Ground truth with 9 classes, (c) SVM-spe, (d) 2D-EMD, (e) 2D-SSA, (f) SMLR-SpATV, (g) MSP-SVMsub, (h) SS-LRR, (i) FS^{2}LRL and (j) Our proposed SMP.

3.5.4 Comparison with Deep Learning Methods

We further compare our SMP with four state-of-the-art deep learning approaches, i.e., CNN [170], CD-CNN [78], DR-CNN [79] and pixel-pair features-based CNN (CNN-PPF) [171]. As recommended in the literatures of these four deep learning methods, in this test, 200 samples are randomly selected from each class as training set and the rest samples are used as testing set. The classification results of these comparing methods on the corrected Indian Pines, Salinas, and PaviaU datasets are obtained from the corresponding literatures and summarized in Table 3.7.

Obviously, for the classification performance on Indian pines and PaviaU datasets, the deep learning approach DR-CNN achieves the best results, while our proposed SMP has produced quite comparable results. However, on Salinas datasets, SMP obtains better results than others. The deep learning models usually require large training size to guarantee classification performance. The proposed method SMP can yield competitive results even when the training size is smaller than 30 according to the classification performance evaluation in Sections 3.5.1-3.5.3. In summary, this has validated again the superiority of our proposed SMP approach in noise-robust spectral-spatial feature extraction and data classification of HSI.

Table 3.7 Comparing of SMP with Four Deep leaning Approaches Using OA (%) on Three Corrected Datasets with the Number of Training Samples.

Corrected Datasets	CNN	CNN-PPF	CD-CNN	DR-CNN	SMP
Indian Pines	90.16%	94.34%	93.61%	**98.54**%	97.64%
Salinas	92.60%	94.80%	95.07%	98.33%	**99.79**%
PaviaU	92.56%	96.48%	95.97%	**99.56**%	98.73%

3.6 Summary

In this chapter, we have proposed a novel spectral-spatial feature mining framework, Superpixelwise Multiscale Prophet model (SMP), for noise-robust feature extraction and effective data classification of HSI. To the best of our knowledge, it is the first time the Prophet model is applied in feature extraction and data classification of the HSI. First, we demonstrate that the Prophet model is able to enhance HSI features in terms of reduced intraclass variance and enlarged interclass diversity. Second, the

superpixelwise image segmentation has found particularly useful for grouping local spectrally similar pixels and reducing the high intra-class heterogeneity and inter-class homogeneity of different land cover classes in HSI. Third, the proposed SMP model has successfully exploited spectral data at different noise levels. As a result, the combined spectral-spatial features can more effectively characterize both the corrected and uncorrected HSI data, especially with very limited training samples. Our SMP model has significantly outperformed a number of state-of-the-art approaches, including several deep learning models along with much more training samples. The improved classification results from the uncorrected datasets have enabled potentially a new and fully automatic roadmap for interpreting HSI where conventional wisdom of prefiltering of unwanted bands can be skipped.

4 Multiscale 2D-SSA and PCA for Spatial-Spectral Noise-Robust Feature Extraction and HSI Classification

4.1 Introduction

In the previous chapter, the multiscale strategy in spectral domain a is employed to suppress noises and improve the HSI classification. In this chapter, we further investigate the combination of spatial and spectral features, in which dimension reduction in spectral domain and multiscale strategy in spatial domain is employed to achieve an effective and fast feature extraction method. Specifically, a novel multiscale 2D-SSA with PCA approach (2D-MSSP) is proposed. We still exploit its capability in processing the uncorrected dataset without removing the noisy bands. In detail, a multiscale 2D-SSA model is firstly applied to original uncorrected HSI dataset to adaptively extract the main information and spatial structures with multiple window sizes. Then, the PCA is utilized to derive informative spectral features and decrease the computational burden for next image processing steps. The extracted multiscale spatial-spectral features are classified by SVM classifier and then fused on the classification maps with a decision-level fusion technique, which can further improve the robustness.

The remainder of this chapter is organized as follows. In Section 4.2, our proposed 2D-MSSP is presented in detail. Section 4.3 describes the experimental setup. Experimental results and analysis are discussed in Section 4.4, with some summaries are drawn in Section 4.5.

4.2 The proposed method

Fig. 4.1 shows the flowchart of proposed 2D-MSSP approach, which has three main stages, i.e., multiscale 2D-SSA for spatial feature extraction, PCA for spectral features extraction, HSI classification and fusion. More detailed implementation of 2D-MSSP is presented as follows.
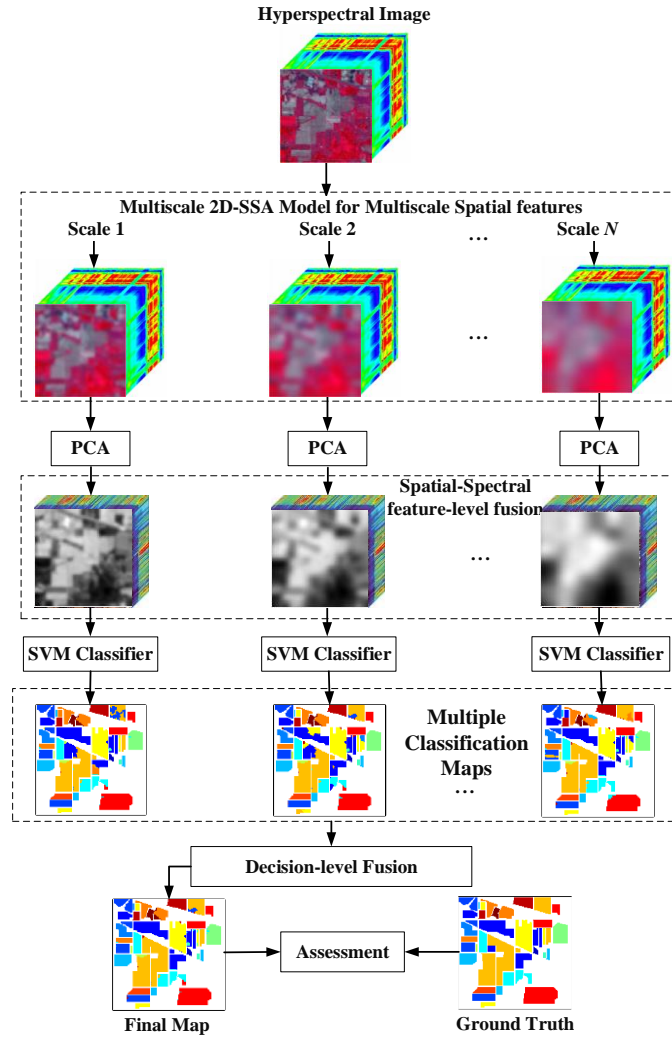
Fig. 4.1 The flowchart of the proposed method.

4.2.1 Spatial-spectral features extraction by 2D-MSSP

The singular spectrum analysis (SSA) is an effective tool for the analysis and forecasting of time-series data [172]. It can decompose a series into several components, i.e., trend, oscillations, and noise. When applying SSA to each spectral band of a hypercube, the 2-D scene can be decomposed and then reconstructed using respective main components with the noise information removal. Specifically, for an image I with a size $N_x \times N_y$, where N_x and N_y represent the band image size, it can be represented by the following matrix:

$$I = \begin{pmatrix} I_{1,1} & I_{1,2} & \cdots & I_{1,N_y} \\ I_{2,1} & I_{2,2} & \cdots & I_{2,N_y} \\ \vdots & \vdots & \ddots & \vdots \\ I_{N_x,1} & I_{N_x,2} & \cdots & I_{N_x,N_y} \end{pmatrix} \tag{4.1}$$

A 2-D window W with a size $L_x \times L_y$ is then defined as:

$$W = \begin{pmatrix} I_{i,j} & I_{i,j+1} & \cdots & I_{i,j+L_y-1} \\ I_{i+1,j} & I_{i+1,j+1} & \cdots & I_{i+1,j+L_y-1} \\ \vdots & \vdots & \ddots & \vdots \\ I_{i+L_x-1,j} & I_{i+L_x-1,j+1} & \cdots & I_{i+L_x-1,j+L_y-1} \end{pmatrix} \tag{4.2}$$

where $L_x \leq N_x$, $L_y \leq N_y$; (i,j) is the spatial position of one pixel in image I. Given a reference position (i,j), the pixels in the corresponding window W can be rearranged into a column vector $A_{i,j} \in \Re^{L_x L_y}$ given below:

$$A_{i,j} = \left(I_{i,j}, I_{i,j+1}, \dots, I_{i,j+L_y-1}, I_{i+1,j}, \dots, I_{i+L_x-1,j+L_y-1} \right)^T \tag{4.3}$$

This 2-D window would raw scan image I from the top left to bottom right in order to exploit all the possible position over the whole image. Thus, the trajectory matrix X of all these possible 2-D window in image I with size $L_x L_y \times (N_x - L_x + 1)(N_y - L_y + 1)$ can be derived by

$$X = \left((A_{1,1})^T, (A_{1,2})^T, \cdots, \left(A_{1,N_y-L_y+1} \right)^T, (A_{2,1})^T, \dots, \left(A_{N_x-L_x+1,N_x-L_x+1} \right)^T \right) \tag{4.4}$$

Note that the trajectory matrix X has a structure of Hankel-block-Hankel (HbH). Here, X can be represented as

$$X = \begin{pmatrix} H_1 & H_2 & \cdots & H_{N_x-L_x+1} \\ H_2 & H_3 & \cdots & H_{N_x-L_x+2} \\ \vdots & \vdots & \ddots & \vdots \\ H_{L_x} & H_{L_x+1} & \cdots & H_{N_x} \end{pmatrix}_{L_x \times (N_x-L_x+1)} \tag{4.5}$$

where each submatrix H_k is Hankel structure as:

$$H_k = \begin{pmatrix} I_{k,1} & I_{k,2} & \cdots & I_{k,N_y-L_y+1} \\ I_{k,2} & I_{k,3} & \cdots & I_{k,N_y-L_y+2} \\ \vdots & \vdots & \ddots & \vdots \\ I_{k,L_y} & I_{k,L_y+1} & \cdots & I_{k,N_y} \end{pmatrix}_{L_y \times (N_y-L_y+1)} \tag{4.6}$$

With the obtained trajectory matrix X, the singular value decomposition (SVD) is implemented to derive the eigenvalues $\left(\lambda_1 \geq \lambda_2 \geq \cdots \geq \lambda_{L_xL_y}\right)$ and the corresponding eigenvectors $\left(U_1, U_2, \dots, U_{L_xL_y}\right)$ of $X(X)^T$, and X can be rewritten as:

$$X = X_1 + X_2 + \cdots + X_r \dots + X_{L_xL_y} \tag{4.7}$$

where the r-th elementary matrix $X_r = \sqrt{\lambda_r}U_rV_r^T$, its principal components $V_r = (X)^T U_r/\sqrt{\lambda_r}$.

Afterwards, the eigenvalue grouping (EVG) is carried out, in which the total set of L_xL_y individual components in (4.7) is grouped into M subsets, denoted as $P = [P_1, P_2, \dots, P_M]$. We can select one or more elementary matrices X_r in each subset to derive the main information of the image without high noisy content. Thus, trajectory matrix X is transformed as:

$$X = X_{P_1} + X_{P_2} + \cdots + X_{P_M} \tag{4.8}$$

Here, X is not necessarily a HbH type matrix. In order to project it into a 2-D signal, a two-step Hankelization process by averaging the antidiagonal values in the matrix is applied first within each block (4.6) and then between blocks (4.5). A Hankelization process is implemented as follows:

$$y_{mn} = \begin{cases} \dfrac{1}{n}\sum\limits_{j=1}^{n} a_{j,n-j+1} & 1 \leq n \leq L \\[3mm] \dfrac{1}{L}\sum\limits_{j=1}^{L} a_{j,n-j+1} & L \leq n \leq K \\[3mm] \dfrac{1}{N-n+1}\sum\limits_{j=n-K+1}^{L} a_{j,n-j+1} & K \leq n \leq N \end{cases} \tag{4.9}$$

where $a_{j,n-j+1}$ refers to the elements of an input matrix and y_{mn} is the output result for Hankelization, $L=L_y$, $K = (N_y - L_y + 1)$ and $N=N_y$ for the case of Hankelization within each block, $L=L_x$, $K = (N_x - L_x + 1)$ and $N=N_x$ for the case of Hankelization between blocks. By repeating two-step Hankelization process for each matrix X_{P_M}, the original image I is reconstructed as：

$$I = y_1 + y_2 + \cdots + y_M = \sum\nolimits_{m=1}^{M} y_m \tag{4.10}$$

As a result, after applying 2D-SSA on each band image I of a HSI data, we finally obtain the reconstructed image $\boldsymbol{I_{spa}}$ with D dimensions, which contain the informative spatial features based on local relevant information in the defined 2-D window.

After extracting the spatial structural content of each band in HSI, PCA is utilized for the main spectral features exploitation and further noise removal as follows:

$$\boldsymbol{I_{spa-spe}} = \mathrm{PCA}(\boldsymbol{I_{spa}})_{N_x \times N_y \times L} \tag{4.11}$$

where L is the number of principal components derived by PCA technique. In this way, the informative content and noisy information even in noisy and water absorption bands can be processed simultaneously in spatial and spectral domain.

In this chapter, multiple window sizes $(N_x \times N_y)$ in 2D-MSSP are utilized. At a given window size, the obtained spatial-spectral features from 2D-MSSP are taken as the input of SVM classifier to generate the classification map. Then, we can get multiple classification maps by using different window sizes. Here, a decision fusion strategy is utilized to generate the final classification result. Specifically, set T scales on the window size, then there would be T classification maps generated, denoted as $S = \{S_1, S_2, ..., S_T\}$. For a given pixel with the spatial position (i, j), its final class label is calculated through majority voting, i.e., the label with the maximum number of appearances within multiple classification maps S:

$$S_{i,j} = \arg\max_{c=1,...,C} \sum\nolimits_{t=1}^{T} F(S_{i,j}^t, c) \tag{4.12}$$

79

where c represents the possible class labels in one HSI data, C is the number of class labels and F is an indicator function given by $F(p,q) = \begin{cases} 1 & \text{if } p = q \\ 0 & \text{otherwise.} \end{cases}$

4.2.2 Noise robustness analysis on 2D-MSSP

In HSI, each band image can be characterized as a sequential spectral vector, which contains high noisy information especially in the water absorption bands [82]. By applying 2D-MSSP, one band image can be decomposed and reconstructed based on the eigenvalues obtained in SVD. In general, the component from the first eigenvalue contains the main information of input data, while noise is usually existed in those small eigenvalues [20]. Therefore, the newly reconstructed HSI data only using more significant components and excluding smaller eigen components can be clearer and more discriminative for image analysis and interpretation.

In 2D-MSSP, the 2-D embedding window size is a key parameter which affects the informativeness and noise level of reconstructed HSI. This parameter directly decides the total number of eigenvalues (components) available. A large window size leads to more components generated. For example, when the window size is $L_x = L_y = 5$, the 2-D embedding window would provide 25 components for each spectral scene. The grouping of these components into a new image denoted as a reconstruction as explained in Section 4.2.1. Thus, when only the basic trend information (the first eigenvalue component) is used for image reconstruction, the reconstructed data with small window size will contain more information while the large one could produce more smoothed results with most of noisy content removed [173].

An example is taken using the 220th spectral band (at 2499nm), which is a water absorption band, from the uncorrected Indian Pines dataset [20], Fig. 4.2 shows the reconstructed scene using first component with different sized 2-D embedding window, along with a clear spectral band (at 667nm) for comparison. As seen from Fig. 4.2(a-b), the 220th band contains much highly noisy content with less detailed information, and that is why many methods remove noisy and water absorption bands for pre-processing. However, these bands may still contain some useful information. As shown in Fig. 4.2(c-d), when applying 2D-SSA to the 220th spectral band, detailed

local spatial structures are preserved, and noisy information is reduced. Besides, the 2D-SSA with a larger 2-D embedding window size generates more smoothed scene with noise and details much reduced. In essence, for HSI data with a high noise level, larger window sizes can remove most of the noisy content. However, if the window size is too large, some important details of the spectral scene may be lost. On the other hand, small window sizes may result in the noise kept which degrades the further image classification. Overall, it shows that our proposed 2D-MSSP can derive the main information and spatial structures of HSI even on the water absorption bands, which demonstrates its robustness to noisy content.

In real cases, the noise level varies throughout the hyperspectral bands [174, 175], which also verified in Fig. 4.2(a-b). Thus, it is challenging to set an optimal window size for all the bands. The proposed multiscale 2D-SSA in this chapter can better solve this problem and further improve the classification performance, which will be further validated in Section 4.4.

(a)   (b)   (c)   (d)
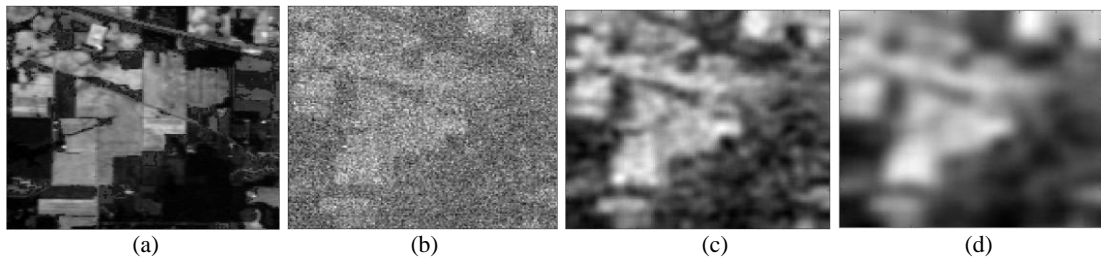
Fig. 4.2 Application of 2D-MSSP to a scene in HSI. (a) Original scene at 667nm. (b) Original scene at 2499nm (a water absorption band); and reconstructed scenes from (b) with $L_x = L_y = 5$ (c) and $L_x = L_y = 10$ (d).

4.3 Datasets and experimental setup

4.3.1 Real Datasets Description

Here we still use three widely used HSI datasets: *1) Indian Pines:* The dataset has 16 types of land-cover classes and 145×145 pixels. In the original dataset, each pixel contains 220 spectral bands. The corrected one discard 20 water absorption bands. *2) SalinasA:* We used a subscene from SalinasA image, denoted SalinasA. This subscene is composed of 86×83 pixels and 6 land-cover classes from 224 spectral bands. The corrected one contains 204 spectral bands. *3) Pavia University:* The dataset is named as PaviaU in this chapter. This scene consists of 610×340 pixels and eight dominant

classes of land covers. This scene is corrected by reducing the available number of bands to 103.

4.3.2 Experimental Settings

To investigate the robustness and classification performance of the proposed method, several state-of-the-art spatial-spectral classification approaches are employed to test on the uncorrected HSI dataset (with no bands removed), and the corrected dataset (with removing the noisy and water-absorption bands). These benchmarks include 2D-SSA [20], multiscale superpixelwise principal component analysis (MSuperPCA) [47], ASMGSSK [76], SMP proposed in Chapter 3, along with two advanced denoising methods, SS-LRR [75] and FS^{2}LRL [82], which show efficacy in classifying uncorrected HSI data. In addition, we directly apply the SVM on raw spectral profiles of HSI as the baseline for classification with spectral-only information (denoted as SVM-spe).

Table 4.1 List of parameter settings for our proposed framework and other benchmarking approaches

Method	Indian Pines, SalinasA	PaviaU
SVM-spe	N/A	N/A
2D-SSA	Window size: 10×10 EVG: 1st	Window size: 5×5 EVG: 1-2nd
MSuperPCA	fundamental superpixel number:100 Scale number: 4	fundamental superpixel number:20 Scale number: 6
ASMGSSK	Filtering degree:0.1 Superpixel number: [176 800, 1600, 3200 800, 1600, 3200]	Filtering degree:0.1 Superpixel number: [200, 400, 800, 1600, 3200, 6400]
SS-LRR	superpixel number: 40	superpixel number: 190
FS^{2}LRL	Subspace dimension: 10 superpixel number: 100 sparse parameter: 0.13 fidelity parameter: 0.040	Subspace dimension: 10 superpixel number: 100 sparse parameter: 0.13 fidelity parameter: 0.040
SMP	τ : [5, 10, 20, 25, 30], Superpixel scale: 150 for Indian Pines Superpixel scale: 600 for SalinasA	τ : [5, 10, 20, 25, 30], Superpixel scale: 100
2D-MSSP	Window size: $\{5 \times 5, 10 \times 10, 20 \times 20, 40 \times 40, 60 \times 60\}$ NPCs: 40	Window size: $\{5 \times 5, 10 \times 10, 20 \times 20, 40 \times 40, 60 \times 60\}$ NPCs: 40

The key parameters of these approaches are set according to their recommended default values [25] as illustrated in Table 4.1. As for our proposed 2D-MSSP, the sizes of 2-D embedding window are set to $\{5 \times 5, 10 \times 10, 20 \times 20, 40 \times 40, 60 \times 60\}$ with five scales. In [3], the 2D-SSA is proposed for feature extraction and data classification in HSI, where different window sizes including $5 \times 5, 10 \times 10, 20 \times 20, 40 \times 40$ and 60×60 are tested. For Indian Pines and Pavia University datasets, the optimal window size is found to be 10×10 and 5×5 to produce the highest classification accuracy. As for the Salinas dataset, the window sizes of 40×40 and 60×60 achieves the best classification. As the optimal window size varies in different datasets, the multi-scale strategy is adopted in the proposed method, aiming to improve the generalization ability on different datasets. The size number of principal components (PCs) selected in the PCA is set to 40 according to the parameter analysis Section 4.3.3. In this chapter, the SVM is adopted as the default classifier for all the involved methods, which are implemented using LIBSVM toolbox [177]. Here, the base kernel function is Gaussian radial basis function (RBF) with the kernel factor and penalty parameter set to 0.125 and 1024 based on the grid search, respectively. Such parameter settings of SVM are kept same in all comparing experiments to ensure a fair comparison.

In order to evaluate the efficacy of the proposed method under various limited and unbalanced training sizes (the number of samples in each class is different because of unbalanced sample distribution), we set the training size varies within $\{1\%, 3\%, 5\%, 10\%\}$ samples per class in the training set using a stratified random scheme from ground truth data. The remaining samples are left for test set. Note that there are some minority classes named *alfalfa*, *grass/pasture-mowed* and *oats* in Indian Pines dataset [178]. The experiments in all datasets are independently repeated ten times, where the averaged results in terms of the overall accuracy (OA), Kappa coefficients (κ) and average accuracy (AA) are employed as quantitative evaluation metrics.

All experiments in this work are implemented using the Matlab 2018a platform on the computer with an Intel (R) Core (TM) i7-8700 CPU (3.20 GHz) and 16.0 GB of memory.

4.3.3 Parameter Analysis

The number of PCs (NPCs) in PCA directly affects the informativeness in the spatial-spectral features, which further influence the final classification results. In this subsection, we discuss the effect of NPCs on the performance of our proposed framework using three corrected datasets. Here, the value of NPCs ranges from 20 to 60 with 5 as the interval. The numbers of training samples are set to 1% per class and the remaining for testing. Meanwhile, all tests are conducted ten times and the corresponding averaged results are recorded to reduce possible biases induced by random sampling.
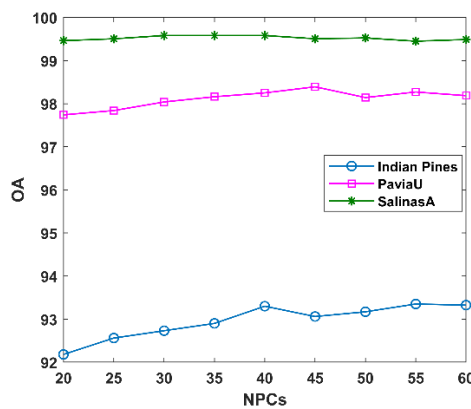
Fig. 4.3 The OA of 2D-MSSP with various numbers of PCs for test datasets.

Fig. 4.3 shows the OA results of the proposed 2D-MSSP by using different values of NPCs on the three datasets. As seen, when using 1% training samples per class, the best NPCs settings on Indian Pines is 40 and 55, while the optimal values on SalinasA fall in the range (30, 40). As for the PaviaU dataset, 2D-MSSP performs best when the NPCs equals to 45. Herein, it is clear that the Indian Pines dataset is more sensitive to the NPCs than other two datasets. This may be due to the fact that the spatial resolution of Indian Pines is much lower and thus its corresponding noises is relatively higher. Therefore, the effect of PCA in noise reduction is more significant on the Indian Pines dataset. Overall, we set NPCs to 40 in all experiments as a trade-off between the efficiency and accuracy in this chapter.

4.4 Results and discussion

In this section, to investigate the robustness of our proposed approach, the experiments are conducted on respectively the uncorrected HSI dataset (without removing any bands), and the corrected dataset (with the noisy and water-absorption bands removed). Besides, the effectiveness of different strategies in 2D-MSSP is also assessed, i.e., the multiscale 2D-SSA, and the PCA technique. To achieve this, we consider two cases: (1) 2D-MSSP with only the multiscale 2D-SSA but not PCA, denoted as 2D-MSSA, and (2) the proposed 2D-MSSP. Here, the baseline SVM-spe is denoted as the method without the above two strategies. Furthermore, our method is also compared with several advanced deep l earning approaches on three datasets.

4.4.1 Results from the Indian Pines Dataset

The quantitative and qualitative performance are evaluated on the corrected and uncorrected Indian Pines datasets. First, the quantitative evaluation in terms of the overall accuracy (OA) and the Kappa coefficient (κ) is conducted between 2D-MSSP and SVM-spe, 2D-SSA [20], MSuperPCA [47], ASMGSSK [76], SS-LRR [75], FS[2]LRL [82], SMP and 2D-MSSA. Then, three superior performing methods are selected to assess the detailed visual and class-based performance comparing with the proposed 2D-MSSP. Note that the best results in tables are labelled in bold face for comparison. As for the visual assessment, the correct or incorrect classification results of different methods are marked in black and magenta circles, respectively.

(1) Quantitative evaluation

From Table 4.2, it is clear that the larger training size leads to higher classification accuracies for all involved methods. Even on these limited and unbalanced training samples, our proposed 2D-MSSP achieve the best performance in terms of OA and κ in all cases, and obtain enough classification accuracy when using 5% training samples. For instance, 2D-MSSP yield about 3% better than the second-best method, SMP proposed in Chapter 3, in OA when using only 1% training samples per class. This validates the superiority of our method in dealing with the Hughes effect. Besides, by comparing SVM_spe with other methods, it is obvious that the spatial feature

introduction (2D-SSA, MSuperPCA, ASMGSSK, SS-LRR, FS²LRL, SMP, 2D-MSSA and 2D-MSSP) can improve the classification performance by only using spectral information. Herein, the SS-LRR and FS²LRL are the denoising methods, which also exhibit promising results on HSI classification. This demonstrates that the noisy content would degrade the image quality and affect the performance of image processing.

Table 4.2 The OA (%) and κ (in parentheses) of different methods on corrected and uncorrected Indian Pines datasets under various training sizes

Samples	Dataset	SVM-spe	2D-SSA	SS-LRR	FS²LRL	MSuper PCA	ASM GSSK	SMP	2D-MSSA	2D-MSSP
1%	Uncorrected	55.10 (0.48)	78.96 (0.76)	76.83 (0.74)	70.18 (0.66)	87.83 (0.86)	87.76 (0.86)	91.05 (0.90)	90.88 (0.90)	**94.32** **(0.94)**
	Corrected	59.14 (0.53)	75.07 (0.72)	76.17 (0.73)	70.72 (0.67)	89.12 (0.87)	87.98 (0.86)	89.81 (0.88)	89.54 (0.88)	**93.08** **(0.92)**
3%	Uncorrected	64.68 (0.60)	91.44 (0.90)	89.04 (0.88)	83.02 (0.81)	95.05 (0.94)	94.61 (0.94)	96.11 (0.96)	96.55 (0.96)	**98.42** **(0.98)**
	Corrected	70.59 (0.66)	89.08 (0.88)	89.25 (0.88)	83.53 (0.81)	95.24 (0.95)	94.63 (0.94)	96.08 (0.96)	96.16 (0.96)	**98.23** **(0.98)**
5%	Uncorrected	69.46 (0.65)	94.76 (0.94)	91.71 (0.91)	87.76 (0.86)	96.42 (0.96)	96.02 (0.95)	95.75 (0.96)	98.03 (0.98)	**99.35** **(0.99)**
	Corrected	74.90 (0.71)	93.55 (0.93)	92.00 (0.91)	88.16 (0.87)	96.56 (0.96)	96.18 (0.96)	96.96 (0.97)	97.57 (0.97)	**99.04** **(0.99)**
10%	Uncorrected	76.13 (0.73)	97.78 (0.97)	94.25 (0.93)	91.80 (0.91)	97.45 (0.97)	97.27 (0.97)	97.13 (0.97)	99.29 (0.99)	**99.77** **(1.00)**
	Corrected	80.98 (0.78)	97.15 (0.97)	94.68 (0.94)	91.96 (0.91)	97.58 (0.97)	97.56 (0.97)	97.20 (0.97)	99.06 (0.99)	**99.67** **(1.00)**

Through analysing the results obtained by SVM-spe, 2D-SSA, 2D-MSSA and 2D-MSSP, we can find that the multiscale 2D-SSA and PCA has significantly enhanced the classification results on the corrected and uncorrected Indian Pines dataset. Specifically, the 2D-MSSP using multiple window sizes has outperformed 2D-SSA which only uses one fixed window size, with a gain up to 15% on uncorrected data and 18% on the corrected one. This is mainly because that the different window sizes can exploit multiscale local spatial features, which are beneficial to model the different sized land cover classes. In addition, by comparing 2D-MSSA and 2D-MSSP, we find that the PCA enables the accuracy improvement up to 3.5%.

As seen in Table 4.2, the involved comparing methods perform differently on the corrected and uncorrected Indian Pines datasets. Concretely, SVM-spe, FS^{2}LRL, MSuperPCA, and ASMGSSK perform better on corrected dataset. On the contrary, 2D-SSA and SMP can mitigate the image degradation from noisy and water absorption bands and produce superior performance on uncorrected Indian Pines dataset in most cases. With regard to our proposed 2D-MSSP, by only using multiscale 2D-SSA, 2D-MSSA is able to achieve better results on the uncorrected datasets, which avoids the noise effects in all cases. Furthermore, the 2D-MSSP obtains superior accuracy on uncorrected dataset to those from the corrected one. This validates the efficacy of 2D-MSSP in noise-robust feature extraction. The operations from multiscale 2D-SSA and PCA can extract discriminative features and reduce noises on both spatial and spectral domain. As a result, 2D-MSSP can be used as an efficient and effective tool for feature extraction and HIS classification without removing unwanted bands.

(2) Visual and class-based performance assessment

In order to analyse the classification performance of each class on corrected and uncorrected datasets, our method is benchmarked with three superior performing methods when using 1% training samples per class as shown in Table 4.2, i.e., 2D-SSA, MSuperPCA and ASMGSSK. Note that the visual and class-based performances of SMP on three HSI datasets are already analysed in Chapter 3, here we emphasize on the evaluation of other comparing methods and 2D-MSSP in this chapter.

From Table 4.3, it is clear that the 2D-MSSP has obtained the best classification accuracy no matter if the noisy and water absorption bands removed or not, where 2D-MSSP produced best results in 15 out of 16 classes on uncorrected dataset while it achieved 11 out of 16 classes on corrected Indian Pines dataset. The performance of 2D-MSSP is about 6.5% better than second-best on uncorrected Indian Pines. Especially, 2D-MSSP significantly suppress its peers especially in the classes 2, 3, 4, 10, 12, 15 and 16 (*Corn-no till*, *Corn-min till*, *Corn*, *Soybeans-no till*, *Soybeans-clean till, Bldg-Grass-Tree-Drives*, *Stone-steel towers*). In addition, 2D-SSA and our proposed 2D-MSSP perform better on uncorrected dataset while MSuperPCA and ASMGSSK produce better results on the corrected one. This validates the noise-robustness of 2D-SSA and 2D-MSSP when training size is 1%. In Indian Pines dataset,

there are some minor classes *alfalfa*, *grass/pasture-mowed* and *oats*, which have the small number of samples for training. When using 1% training size, there are only 5, 3 and 2 samples for training in classes *alfalfa*, *grass/pasture-mowed* and *oats*, respectively. From Table 4.3, we can find that 2D-MSSP and MSuperPCA achieve promising performance in classifying *grass/pasture-mowed* and even realize correct identification of all corresponding pixels of *alfalfa* and *oats*. Overall, 2D-MSSP can effectively identify the large homogeneous regions and some small objects simultaneously.

Table 4.3 Classification accuracy (%) of competitive methods for the Indian Pines data with 1% training samples per class

	Uncorrected				Corrected			
Class	2D-SSA	MSuperPCA	ASMGSSK	2D-MSSP	2D-SSA	MSuperPCA	ASMGSSK	2D-MSSP
1	52.59	**100.00**	83.04	**100.00**	5.41	**100.00**	60.96	**100.00**
2	73.71	84.46	83.57	**90.23**	67.74	85.54	84.74	**95.85**
3	74.59	79.23	83.94	**92.75**	69.37	78.60	83.35	**92.83**
4	78.33	52.88	85.46	**99.15**	71.61	60.57	84.50	**97.91**
5	69.74	80.43	81.63	**82.49**	68.79	**88.31**	82.43	81.78
6	86.36	93.99	87.49	**98.63**	84.37	97.63	88.99	**99.18**
7	92.72	93.09	92.96	**96.30**	91.85	93.09	95.19	**100.00**
8	93.28	97.05	96.17	**100.00**	91.26	96.75	98.33	**98.73**
9	64.04	**100.00**	70.35	**100.00**	55.79	**100.00**	76.14	84.21
10	68.42	84.76	82.80	**91.90**	65.26	86.51	81.05	**91.11**
11	80.79	94.63	95.07	**96.54**	77.73	**96.11**	94.60	94.41
12	61.83	75.32	77.79	**87.34**	53.05	69.64	76.80	**89.91**
13	97.81	**99.50**	86.68	94.11	91.35	**99.52**	91.82	90.79
14	91.99	95.42	94.39	**99.38**	90.71	**96.12**	94.45	95.24
15	76.25	86.29	82.16	**93.27**	68.32	83.22	83.97	**88.04**
16	92.50	47.93	45.11	**97.93**	89.28	73.88	57.86	**96.74**
OA	78.96	87.83	87.76	**94.30**	75.07	89.12	87.98	**93.08**
κ	0.76	0.86	0.86	**0.94**	0.72	0.88	0.86	**0.92**
AA	78.43	85.31	83.04	**95.00**	71.37	87.84	83.45	**93.64**

Fig. 4.4 shows the visual result comparisons between four approaches on uncorrected and corrected datasets using 1% training samples per class, respectively. As shown, these four methods with spatial features have generate more accurate and smoother results. However, there still exist many misclassifications on maps. Specifically, as marked in magenta circles in Fig. 4.4, the classes *Corn-no till* and *Soybeans-min till,*

Soybeans-no till and *Corn-no till* are severely misclassified with each other. As for 2D-SSA, it better identifies these classes on uncorrected datasets as seen in Fig. 4.4(c). Even so, on both uncorrected and corrected data, 2D-SSA yields wrong classifications at the boundaries or small objects. This is mainly because there is only one type of spatial features are extracted in 2D-SSA without considering boundary information. On the contrary, MSuperPCA and ASMGSSK give much better uniformity and boundary location results as illustrated in Fig. 4.4(e-h). This may be due to that they employ the superpixel segmentation techniques which segment the land cover classes into different objects with adaptive shapes and sizes. Though the geometrical distortions in Fig. 4.4(c-d) are much corrected by MSuperPCA and ASMGSSK, there are still several small uncorrected classifications Fig. 4.4(e-h). To be specific, MSuperPCA produces better visual performance on corrected Indian Pines dataset where misclassified regions of *Soybeans-no till* and *Corn-no till* are reduced. However, the classes *Corn-no till* and *Soybeans-min till* are still wrongly discriminated in some areas as highlighted in magenta circles in Fig. 4.4(e-f). Besides, MSuperPCA gains promising performance in identifying Woods on uncorrected data while it better classifies Grass/pasture on the corrected one as marked in black circle in Fig. 4.4(e-f). The ASMGSSK obtain comparably similar results with MSuperPCA. It performs better on corrected data, where classes *Grass/trees* and *Corn-no till* are seriously misclassified on the uncorrected data. With regard to our proposed 2D-MSSP, as shown in Fig. 4.4(i-j), it achieves better visual performance than others with improved object boundaries and spatial consistency. As highlighted in the circles, the results on uncorrected dataset are superior to those on corrected one. The classes *Corn-no till*, *Soybeans-min till, Grass/pasture, Soybeans-no till* are better identified by 2D-MSSP by exploiting more information from uncorrected data. These visual results are consistent with the class-based results in Table 4.3, which again verify the efficacy of our method in noise-robust feature extraction and HSI classification.

4.4.2 Results from the SalinasA Dataset

Similarly, the quantitative and qualitative performance are also assessed on SalinasA dataset with or without noisy and water absorption bands, denoted as uncorrected SalinasA and corrected SalinasA, respectively. The comparisons on these two types of

data between SVM-spe, 2D-SSA, SS-LRR, FS^{2}LRL, MSuperPCA, ASMGSSK, 2D-MSSA, SMP and 2D-MSSP in terms of OA and κ are summarized in Table 4.4. Furthermore, visual and class-based results of comparing methods are also described in detail.
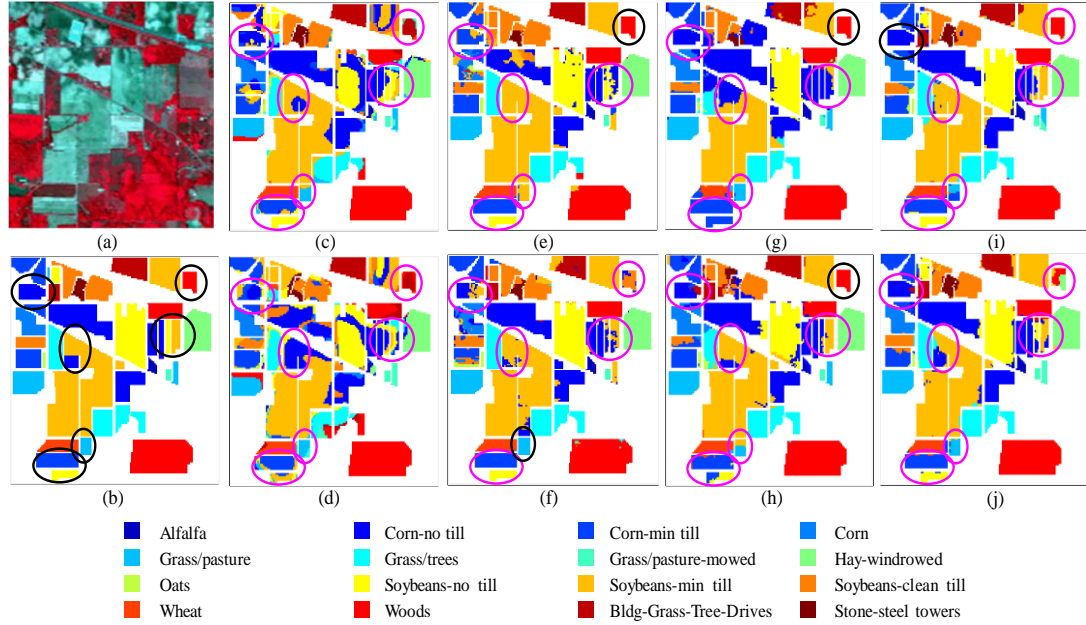
Fig. 4.4 Classification maps on the Indian Pines data (1% samples per class): (a) False colour image (R: 831nm, G: 657nm, B: 557nm), (b) Ground truth in 16 classes, (c) 2D-SSA on uncorrected data (OA=78.96%), (d) 2D-SSA on corrected data (OA=75.07%), (e) MSuperPCA on uncorrected data (OA=87.83%), (f) MSuperPCA on corrected data (OA=89.12%), (g) ASMGSSK on uncorrected data (OA=87.76%), (h) ASMGSSK on corrected data (OA=87.98%), (i) 2D-MSSP on uncorrected data (OA=94.30%) and (j) 2D-MSScorrected data. (OA=93.08%).

(1) Quantitative evaluation

As shown in Table 4.4, all approaches achieve much higher classification results than those on Indian Pines datasets. This mainly due to the high spatial resolution and simple structured land covers in SalinasA image, which leads to low noise level and less spectral and spatial confusion in the scene. As a result, land cover classes are more easily to identify. Overall, the proposed method 2D-MSSP still ranks first on both uncorrected and corrected datasets with the highest OA and κ when the training size is 3%, 5% and 10%. The SMP proposed in Chapter 3 achieves the best results in the case of 1% training size. This demonstrates the efficacy of 2D-MSSP and SMP under various limited training samples. Besides, 2D-MSSP generates better results on

uncorrected dataset when using 1% and 3% training samples per class, and correctly classifies uncorrected and corrected data when the training size is larger than 5%. This validates the noise-robust property of 2D-MSSP, where the superior results are mainly owing to the comprehensive spatial-spectral features even in noisy and water absorption bands.

Table 4.4 The OA (%) and κ (in parentheses) of different methods on the corrected and uncorrected Salinas datasets under various training sizes

Samples	Dataset	SVM-spe	2D-SSA	SS-LRR	FS²LRL	MSuper PCA	ASMGSSK	SMP	2D-MSSA	2D-MSSP
1%	Uncorrected	97.49	99.04	97.67	98.38	88.95	97.29	**99.76**	99.53	99.72
		(0.97)	(0.99)	(0.97)	(0.98)	(0.86)	(0.97)	**(1.00)**	(0.99)	**(1.00)**
	Corrected	97.12	98.86	97.79	97.88	91.81	97.37	**99.59**	99.57	**99.59**
		(0.96)	(0.99)	(0.97)	(0.97)	(0.90)	(0.97)	**(1.00)**	(0.99)	(0.99)
3%	Uncorrected	98.17	99.57	98.67	99.04	97.15	98.56	99.80	99.85	**99.96**
		(0.98)	(0.99)	(0.93)	(0.99)	(0.96)	(0.98)	(1.00)	(1.00)	**(1.00)**
	Corrected	98.34	99.60	98.73	98.91	97.46	98.57	99.79	99.91	**99.94**
		(0.98)	(0.99)	(0.98)	(0.99)	(0.97)	(0.98)	(1.00)	(1.00)	**(1.00)**
5%	Uncorrected	98.72	99.67	99.04	99.41	98.40	99.10	99.83	99.98	**100.00**
		(0.98)	(1.00)	(0.99)	(0.99)	(0.98)	(0.99)	(1.00)	(1.00)	**(1.00)**
	Corrected	98.80	99.71	99.04	99.34	98.54	99.20	99.80	99.94	**100.00**
		(0.99)	(1.00)	(0.99)	(0.99)	(0.98)	(0.99)	(1.00)	(1.00)	**(1.00)**
10%	Uncorrected	99.26	99.83	99.42	99.66	99.27	99.56	99.84	100.00	**100.00**
		(0.99)	(1.00)	(0.99)	(1.00)	(0.99)	(0.99)	(1.00)	(1.00)	**(1.00)**
	Corrected	99.34	99.78	99.50	99.69	99.37	99.59	99.84	100.00	**100.00**
		(0.99)	(1.00)	(0.99)	(1.00)	(0.99)	(0.99)	(1.00)	(1.00)	**(1.00)**

As for other methods, SVM-spe, SS-LRR, MSuperPCA and ASMGSSK produce better results on corrected SalinasA in most cases. The 2D-SSA performs inconsistently on the two kinds of data, where it only achieves better classification performance on uncorrected data when 1% and 10% training samples are used. The denoising method FS²LR yields higher OA and κ on uncorrected SalinasA in most cases. This has validated its efficacy in noise removal and image recovery on the SalinasA HSI data. Meanwhile, 2D-MSSP performs better on corrected data when the training size is larger than 5% per class. The SMP obtain better results on uncorrected data in all cases, which is consistent with the evaluation in Chapter 3.

Through the comparisons between SVM-spe, 2D-SSA, 2D-MSSA and 2D-MSSP, we can find that 2D-SSA has the potential in noise-robust feature extraction especially when training size is 1% and 10%, and the incorporation of multiscale window size (2D-MSSA) improves its ability in suppressing noise. Consequently, by combining the 2D-MSSA and PCA, our approach 2D-MSSP shows strong noise robustness and high classification accuracy on SalinasA image.

(2) Visual and class-based performance assessment

Here, we select three superiror methods on SalinasA, i.e., 2D-SSA, SS-LRR and FS^{2}LRL to compare with our 2D-MSSP in terms of class-based accuracy and classification maps with 1% of training samples per class used. As shown in Table 4.5, our 2D-MSSP still produces the best results on the SalinasA dataset, especially in 4 out of 6 classes on the uncorrected data, and generates the highest accuracy in all classes on the corrected dataset. Especially, 2D-MSSP produces significant better classification accuracy than its peers on uncorrected SalinasA data in the classes #2, #3 and #6 (*Corn senesced green weeds*, *Lettuce romaine 4wk* and *Lettuce romaine 7wk*). With 1% of training samples per class, only the SS-LRR performs better on the corrected data, while 2D-SSA, FS^{2}LRL and 2D-MSSP all have better results on the uncorrected one.

Table 4.5 Classification accuracy (%) of competitive methods on the SalinasA data with 1% training samples per class

	Uncorrected				Corrected			
Class	2D-SSA	MSuperPCA	ASMGSSK	2D-MSSP	2D-SSA	MSuperPCA	ASMGSSK	2D-MSSP
1	99.50	99.53	99.74	**100.00**	99.49	99.53	99.74	**100.00**
2	96.44	96.39	97.85	**99.93**	95.22	96.68	97.55	**99.85**
3	93.48	93.41	94.98	**99.36**	91.85	93.28	93.77	**98.23**
4	99.01	99.62	**99.95**	99.74	99.48	99.76	99.55	**100.00**
5	99.75	**99.76**	99.57	99.55	99.65	99.68	99.52	**99.70**
6	96.57	96.71	97.21	**99.63**	96.60	96.92	96.11	**99.12**
OA	97.49	97.67	98.38	**99.72**	97.12	97.79	97.88	**99.59**
K	0.97	0.97	0.98	**1.00**	0.96	0.97	0.97	**0.99**
AA	97.42	97.57	98.24	**99.70**	97.06	97.64	97.73	**99.48**

The visual results of these four approaches are depicted in Fig. 4.5. As seen, our method 2D-MSSP generates most accurate classification maps with better uniformity and boundary location on uncorrected SalinasA image. From these classification maps in Fig. 4.5, it is clear that the classes *Broccoli green weeds_1*, *Lettuce romaine 4wk* and *Lettuce romaine 5wk*, and the classes *Lettuce romaine 6wk* and *Lettuce romaine 7wk* are easily misclassified with each other. Specifically, SS-LRR and FS^{2}LRL fail to correctly identify them on either uncorrected or corrected data as marked in magenta circles in Fig. 4.5(e-h). The 2D-SSA on corrected dataset (Fig. 4.5(d)), 2D-MSSP on two kinds of datasets (Fig. 4.5(i-j)) can better classify the *Broccoli green weeds_1* and *Lettuce romaine 4wk* as highlighted in the black circles. However, all involved methods fail to correctly classify the classes *Lettuce romaine 6wk* and *Lettuce romaine 7wk.* Fortunately, as depicted in black circles in Fig. 4.5(i-j), the proposed 2D-MSSP can significantly improve the classification performance on these two classes especially on uncorrected datasets. This superiority thanks mainly to the combination of multiscale spatial and spectral features in 2D-MSSP. Overall, 2D-SSA, FS^{2}LRL and 2D-MSSP yield better classification maps on uncorrected SalinasA image, which is consistent with the class-based results.
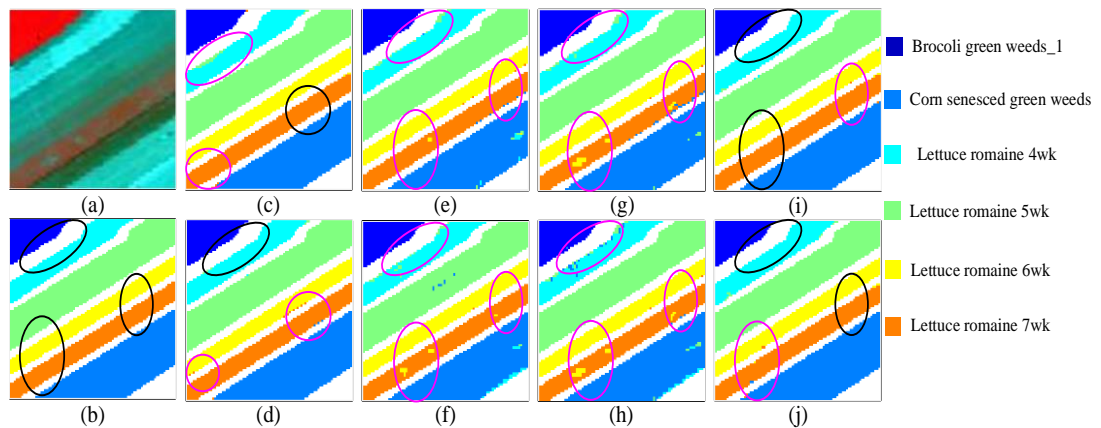
Fig. 4.5 Classification maps on the SalinasA dataset (1% samples per class): (a) False colour image (R: 831nm, G: 657nm, B: 557nm), (b) Ground truth in 16 classes, (c) 2D-SSA on uncorrected data (OA=99.04%), (d) 2D-SSA on corrected data (OA=98.86%), (e) SS-LRR on uncorrected data (OA=97.67%), (f) SS-LRR on corrected data (OA=97.79%), (g) FS2LRL on uncorrected data (OA=98.38%), (h) FS2LRL on corrected data (OA=97.88%), (i) 2D-MSSP on uncorrected data (OA=99.72%) and (j) 2D-MSSP on corrected data. (OA=99.59%)

4.4.3 Results from the PaviaU Dataset

We further analyse the quantitative, visual and class-based results on the PaviaU dataset. Here we only test on the corrected data since the uncorrected one is unavailable. The best results in each row in tables are marked in bold and the correctly or incorrectly classified regions in the classification maps are highlighted with black and magenta circles, respectively.

(1) Quantitative evaluation

Table 4.6 summaries the OA and κ of comparing methods using different training sizes on corrected PaviaU dataset. This image has higher spatial resolution and lower dimension size, which reduces the Hughes phenomenon to some extent [77]. As shown, the classification performances of many approaches with very limited training samples are relatively better than those on Indian Pines dataset. However, there are various types of land cover classes in PaviaU leading it to be a complicated scene. As listed in Table 4.6, our proposed 2D-MSSP still achieves the high classification accuracy and ranks first among these advanced methods in all cases. In addition, the superiority of 2D-MSSP is more significant when the number of training samples is smaller. This again validates the efficacy of proposed strategies in the HSI classification with limited and unbalanced training samples. By using multiscale superpixel segmentation, ASMGSSK significantly improve the classification accuracy, which just follows 2D-MSSP. The SMP proposed in Chapter 3 ranks third among all methods. The two denoising methods and MSuperPCA also exhibit promising performance though they pay more attention on noise removal rather than HSI classification.

In order to investigate the effectiveness of different strategies in our methods, we further compare the results generated by SVM-spe, 2D-SSA, 2D-MSSA and 2D-MSSP. From Table 4.6, it is clear that the spatial features extracted from 2D-SSA can improve the accuracy by only using spectral information in SVM-spe with a gain up to 4.6%. Then through using multiscale spatial feature, the 2D-MSSA further enhances the classification performance with a maximum gain of 2.6%. Finally, by combining multiscale spatial-spectral features from multiscale 2D-SSA and PCA, our proposed method 2D-MSSP achieve high classification accuracy in the PaviaU data.

Table 4.6 The OA (%) and κ (in parentheses) of different methods on the corrected PaviaU dataset under various training sizes

Samples	1%	3%	5%	10%
SVM-spe	88.75 (0.85)	92.12 (0.89)	92.93 (0.91)	93.84 (0.92)
2D-SSA	93.30 (0.91)	96.19 (0.95)	96.87 (0.96)	97.70 (0.97)
SS-LRR	92.12 (0.89)	95.10 (0.93)	95.92 (0.95)	96.71 (0.96)
FS^{2}LRL	93.40 (0.91)	95.86 (0.94)	96.58 (0.95)	97.12 (0.96)
MSuperPCA	95.43 (0.94)	97.66 (0.97)	98.18 (0.98)	98.78 (0.98)
ASMGSSK	98.17 (0.98)	99.11 (0.99)	99.32 (0.99)	99.57 (0.99)
SMP	96.84 (0.96)	98.29 (0.98)	98.56 (0.98)	99.17 (0.99)
2D-MSSA	95.85 (0.94)	97.06 (0.96)	97.92 (0.97)	98.48 (0.98)
2D-MSSP	**98.29 (0.98)**	**99.20 (0.99)**	**99.42 (0.99)**	**99.73 (1.00)**

(2) Visual and class-based performance assessment

Here, three methods, 2D-SSA, MSuperPCA and ASMGSSK are selected to compare with 2D-MSSP in terms of visual and class-based performance. As shown in Table 4.7, the proposed 2D-MSSP achieves best results in terms of OA, κ and AA. As for the class-based performance, it ranks first in 6 out 9 classes, which is followed by ASMGSSK that exhibits superiority in 3 out of 9 classes. The 2D-SSA and MSuperPCA show potential on the identification of class *Shadows*, though it generates inferior results of OA, κ and AA.

The classification maps of ASMGSSK, MSuperPCA, 2D-SSA, and 2D-MSSP are shown in Fig. 4.6. As seen, the classes *Meadows*, *Trees* and *Bare Soil* are easily confused with each other. From Fig. 4.6(c-f), it is clear that the 2D-SSA fails to correctly discriminate the *Meadows* and *Trees* as marked by magenta circles in Fig. 4.6(c). Most of these misclassifications are further corrected by the MSuperPCA, ASMGSSK and 2D-MSSP as shown in black circles in Fig. 4.6(d-e). However, the 2D-SSA, MSuperPCA and ASMGSSK all have difficulty in correctly classifying the *Meadows* and *Bare Soil*. This mainly because that the visually sparse *Meadows* regions are easily to be spectrally confused with *Bare Soil*. As depicted in Fig. 4.6(c-e), many small misclassified areas spread all over *Bare Soil* regions in the classification maps of 2D-SSA and ASMGSSK. With regard to the identification of class *Gravel*, the 2D-SSA seriously misclassifies it with class *Self-Blocking Bricks*, while MSuperPCA,

95

ASMGSSK and 2D-MSSP can better identify it. However, 2D-SSA yields superior classification performance on discrimination of classes *Asphalt* and *Trees* than the other three methods. Overall, our 2D-MSSP yields promising visual performance in PaviaU dataset with better region uniformity and boundary outlining. This validates the efficacy of 2D-MSSP in HSI classification under limited training samples.

Table 4.7 Classification accuracy (%) of competitive methods for the corrected PaviaU data with 1% training samples per class

Class	2D-SSA	MSuperPCA	ASMGSSK	2D-MSSP
1	93.45	94.06	99.06	**99.75**
2	98.82	99.00	99.82	**100.00**
3	72.95	95.94	99.78	**100.00**
4	90.29	72.25	**93.09**	84.44
5	99.29	97.26	98.49	**100.00**
6	87.18	95.05	**100.00**	100.00
7	83.09	97.33	**99.84**	99.77
8	87.76	96.91	98.50	**99.08**
9	98.16	**99.73**	58.61	78.57
OA	93.30	95.43	98.17	**98.29**
$\mathcal{K}$	0.91	0.94	**0.98**	**0.98**
AA	93.45	94.06	94.13	**95.73**

Asphalt Meadows Gravel Trees Painted metal sheet Bare Soil Bitumen Self-Blocking Bricks Shadows
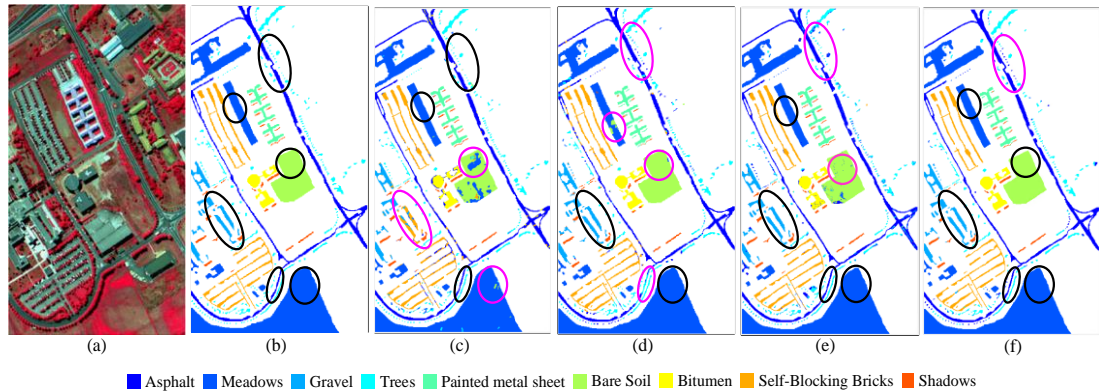
Fig. 4.6 Classification maps on the corrected PaviaU data (1% samples per class): (a) False colour image (R: 834nm, G: 650nm, B: 550nm), (b) Ground truth with 9 classes, (c) 2D-SSA (OA=93.30%), (d) MSuperPCA (OA=95.43%), (e) ASMGSSK (OA=98.17%), (f) 2D-MSSP (OA=98.29%).

4.4.4 Comparing with Deep Learning Methods

In this chapter, we also compare 2D-MSSP with state-of-the-art deep learning approaches, i.e., CNN [170], CD-CNN [78], DR-CNN [79] and CNN-PPF [171]. Similarly, 200 training samples are randomly selected from each class and the rest samples are used as testing set. Since that only the Indian pines and PaviaU are the same datasets used for the comparing deep learning methods and our proposed 2D-MSSP, here the classification results of these methods on the corrected Indian Pines and PaviaU datasets are obtained from the corresponding literatures and summarized in Table 4.8.

As seen in Table 4.8, our 2D-MSSP outperforms the four deep learning approaches with a large training size, i.e., 200 training samples. Deep learning methods usually need more training samples to reach promising performance. As presented in Sections 4.4.1-4.4.3, the training size of 5%, 1% and 3% is enough for 2D-MSSP to achieve a high classification accuracy. Hence, we can conclude that the proposed 2D-MSSP is more advantageous than these state-of-the-art deep learning methods, especially when the training size is limited. This experiment further demonstrates the superiority of our method in HSI classification.

Table 4.8 The OA (%) of 2D-MSSP and four deep leaning methods on three datasets with different training sizes (in parentheses)

Corrected Datasets	CNN	CNN-PPF	CD-CNN	DR-CNN	2D-MSSP
Indian Pines	90.16%	94.34%	93.61%	98.54%	**99.89%**
Salinas	92.60%	94.80%	95.07%	98.33%	**99.99%**
PaviaU	92.56%	96.48%	95.97%	99.56%	**99.87%**

4.5 Summary

In this chapter, we have proposed a novel spatial-spectral method for noise-robust feature extraction and effective HSI classification under limited and unbalanced training size, even without filtering out the unwanted noisy and water absorption bands. First, the 2D-SSA with multiscale embedding window sizes are applied to exploit the multiscale local spatial features at different noise levels. Then, in each scale, the PCA is used to further extract spectral features and remove noisy information. The

comprehensive combination of multiscale spatial-spectral features can effectively characterize image structures and remove noisy content, which can directly deal with the uncorrected HSI data even with very limited training samples. The experimental results on three HSI datasets have validated that our 2D-MSSP model outperforms the other state-of-the-art approaches including several advanced deep learning methods with much larger training size. Especially, the superior classification results on uncorrected datasets provides potential to automatically interpret HSI without prefiltering the noisy bands.

5 Geolocating and Measuring Offshore Infrastructure with Multimodal Satellite Data

In this chapter, by combining Sentinel-1 SAR and Sentinel-2 MSI images, we present a framework for the geolocation and size estimation of offshore energy infrastructure, validated against a ground truth data set of Scottish waters. By combining the advantages of the SAR data and MSI imagery from the Sentinel satellites, an effective method is presented to quickly locate the position of offshore energy infrastructure, along with the further topside area assessment of oil/gas platforms and diameter evaluation of wind turbines.

5.1 Study areas and datasets

5.1.1 Study areas

The study area is the area between the Scotland's Exclusive Economic Zone and the baseline and closing bays (as shown in Fig.5.1). Note that the infrastructure within internal waters is excluded due to the practice of 'parking' oil and gas platforms within internal waters for variable periods, and the corresponding challenge of generating accurate ground-truth data. Most infrastructure is located beyond the baseline and future energy structures are likely to be constructed further offshore [179]. Scotland is located in northwest Europe and surrounded by the North Sea on the east, the North Channel and the Irish Sea on the southwest and the Atlantic Ocean on the north and west. The water depths of the study area vary from shallow coastal waters to more than 2,000 m in some ocean areas. Scottish waters cover approximately 371,915 km2 and contain some of the largest oil reserves in Europe. Offshore hydrocarbon exploitation begins in the 1970's and remains a major activity in Scottish waters. Typical oil and gas installations within Scottish waters include platforms that are either concrete gravity based or fixed steel jackets. Fixed steel jackets can comprise a single integrated platform or two or more bridge-linked platforms, which inevitably increases the difficulty of platform identification in satellite imagery. In recent years, the Scottish

government has also promoted offshore renewable energy. Several Offshore Wind farms have been constructed including Beatrice Offshore Wind farm, Moray East Offshore Wind farm (under construction), HyWind Offshore Wind farm (Aberdeenshire), Kincardine Offshore Wind farm (Aberdeenshire) and Aberdeen Offshore Wind farm (Aberdeen Bay). The Beatrice offshore wind farm with wind turbines located 25km from the Scottish shoreline is the world's deepest offshore wind project at the time of construction.
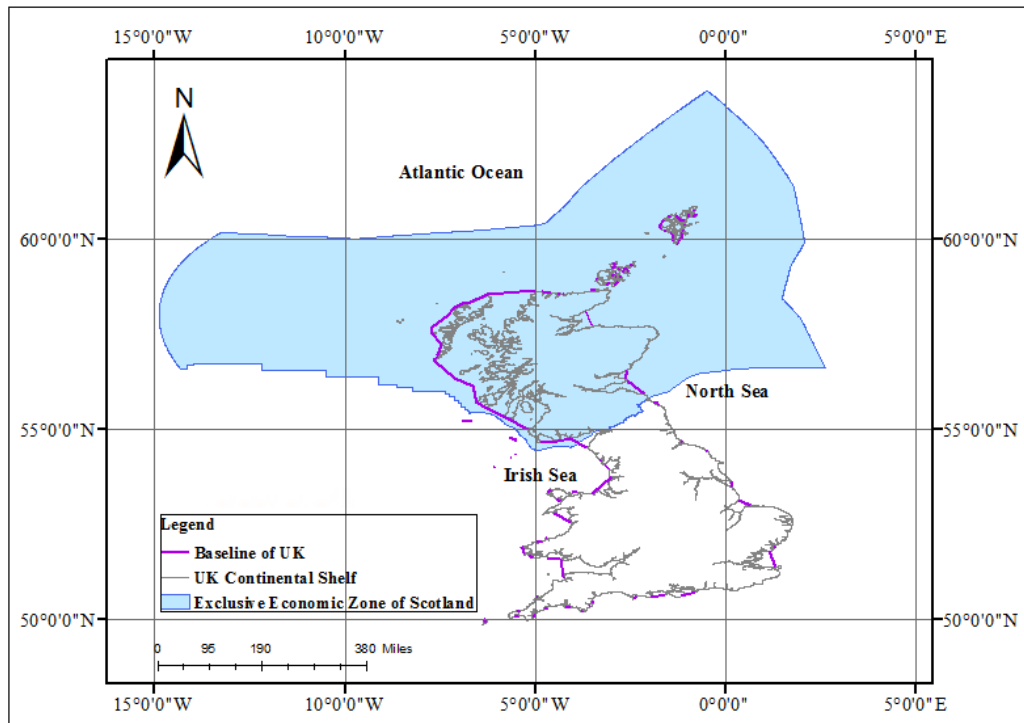
Fig. 5.1 The Scottish Exclusive Economic Zone: location of the study area in the North Sea

5.1.2 Datasets

The data used in this study includes images and auxiliary data. Auxiliary data is used to assemble the ground truth dataset validate the spatial distribution and size of offshore infrastructure, and assess the performance of the proposed method. Image data is employed to identify offshore energy infrastructure in Scottish waters and analyse their sizes.

(1) Ground truth dataset

In this section, a ground truth dataset of offshore energy infrastructure is constructed using: (1) Scottish Waters (200M Limit) - Exclusive Economic Zone (EEZ) [179], (2) The Scotland coastline and baseline [180], (3) The Oslo and Paris Commissions (OSPAR) Inventory of Offshore Installations-2019 [181] , (4) The offshore infrastructure distributions on the UK's Continental Shelf provided by the Oil and Gas Authority (OGA) [182], (5) The sizes measured in Sentinel Hub EO browser [183], (6) The Beatrice Offshore Wind Farm Consent Plan [184]. (7) Development Layout and Specification Plan for Moray East Offshore Wind Farm [185]. (8) The Design Statement for Aberdeen Offshore Wind Farm [186]. (9) The Construction Plan for Hywind Wind Farm [187]. (10) Kincardine Offshore Wind Farm Environmental Scoping Assessment [188].

The summarized ground truth data is given in Tables A.2.1 – A.2.6 of the Appendix 3.

(2) Images for the proposed method

Image data includes Sentinel-1 SAR data and Sentinel-2 MSI data. The European Space Agency (ESA) provides open SAR images released by the Sentinel-1 (Sentinel-1A launched on April 3, 2014 and Sentinel-1B launched on April 25, 2016) and open multispectral images released by the Sentinel-2 (Sentinel-2A launched on June 23, 2015 and Sentinel-2B launched on March 7, 2017). Sentinel-1 operates all-weather and all-day observation at C-band supporting single polarization (HH or VV) and dual polarization (HH+HV or VV+VH). The two-satellite constellation has a revisiting frequency of less than 1 day at the Arctic and 3 days at the equator, and 1-3 days for Europe, Canada and main shipping routes. It has four modes. In this chapter, we use Sentinel-1 data in interferometric Wide Swath (IW) VV+VH polarization with 250 km swath, 5×20 m spatial resolution. Specifically, the orthorectified VH Sentinel-1 images are downloaded. Sentinel-2 is a multispectral sensor working in visible, near-infrared and short-wave infrared bands with spatial resolution of 10m, 20m and 60m, respectively. The satellites have a swath width of 290 km and a revisit time of 5 days under the same viewing conditions. In this chapter, we only use the bands in blue (Band #2), green (Band #3) and red (Band #4) which have spatial resolution of 10m. The downloaded Sentinel-2 Level 2A products and Sentinel-1 orthorectified data are used

directly with no need for further processing. The software and metadata used to generate the results in this chapter are uploaded in Zenodo [189].

5.2 Methodology

The proposed method includes two schemes: location detection and size estimation. Fig 5.2 shows the workflow of the framework. First, the time series (a dataset that tracks a sample over time) Sentinel-1 data are processed through three strategies to detect the 'guide area', or approximate contour position of possible offshore infrastructure. Then, using this 'guide area' to quickly locate the offshore candidates in locally cloud free Sentinel-2 data. Finally, three steps are employed based on clear shape and structural information on Sentinel-2 to refine the location and estimate the size of each structure.
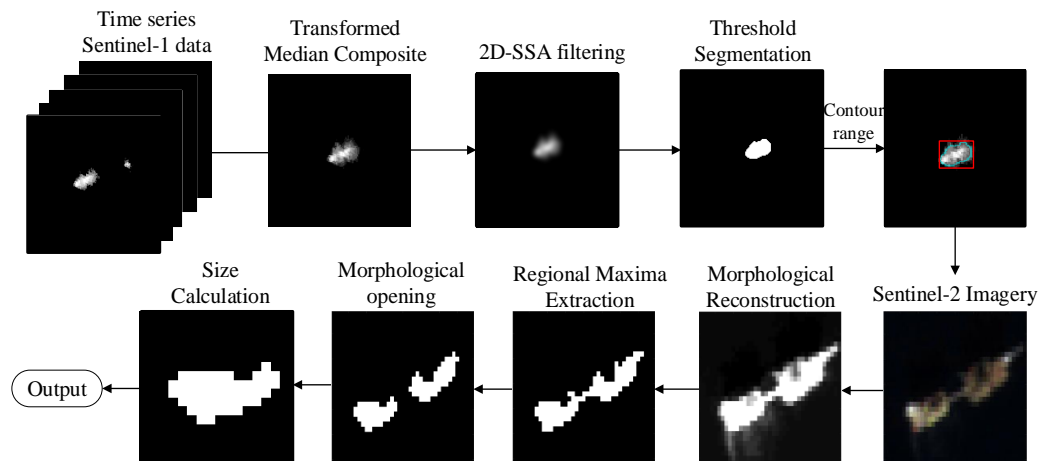
Fig. 5.2 The flowchart of the proposed method, note that the Sentinel-2 image area is shown as the red box in final Sentinel-1 image.

5.2.1 Detection of objects of interest

5.2.1.1 Contour detection in Sentinel-1 data

In SAR images, oil/gas platforms can be easily confused with the wake generated in the surrounding water. Due to this, moving vessels, and signal noise can lead to misidentified of fixed infrastructure. However, in time-series data offshore infrastructure has a temporally invariant position. Temporal changes can help to address the challenges of the prevalence of noises and vessels on the ocean. In this

section, for the robust identification of offshore infrastructure from SAR images, three principal steps (median composite, 2D-SSA filtering and threshold segmentation) are designed to process Sentinel-1 SAR imagery, remove vessels and noise, and output the location range of offshore infrastructure.

(1) Transformed Median Composite for noise removal

For each scene, five Sentinel-1 images from June 2020 to January 2022 are used to compose the time series. According to the position-invariant characteristic of offshore infrastructure, we directly calculate the median intensity value of each pixel from five time-series images to form a median composite image. Among the time-series image, the platforms and wind turbines have a higher occurrence frequency than the moving objects. As a result, on the transformed median composite image, due to the low occurrence frequency, the vessels and speckle noises disappear. We take the platform Clair, and the linked platform consisting of Clair Ridge Drilling and Process (DP) and Clair Ridge quarters and utilities (QU) as an example. As shown in Figs.5.3 (a-e), different vessels (marked with red circles) appear on the Sentinel-1 data at different dates. Some ships are usually in similar locations near the oil/gas platform. This increases the challenge to remove them from the images. Using the subtle position change, the median composite operation successfully removes these ships and reduces noise as depicted in Fig.5.3 (f). Overall, the background ocean noise is suppressed yet the offshore infrastructure is accentuated. Fig. 5.4 shows the wind turbines in the Beatrice offshore wind farm in Sentinel-1 image at different dates. It is clear from Figs. 5.4 (a-e) that, as expected, the blade part of wind turbine changes direction over time. By considering the wind turbine at different dates via the median composite operation, the main structures of these rotating objects are maintained with background noises removed.

(2) 2D-Singular Spectrum Analysis (SSA) Filtering for image smooth

The transformed median composite can minimize the high brightness noises to some extent. However, there is still a large amount of noise remaining in the image, especially the water wakes around the offshore infrastructure, which can seriously affect the subsequent target detection [190]. In order to improve the location

103

interpretability of these infrastructure, noises must be filtered while keeping more edge details and clearer contour. The 2D-SSA method is an effective spatial feature extraction tool [20]. For a grayscale image, the 2D-SSA method can decompose the image into several components, based on the spatial information, in which the first component contains the main information and spatial structures of the input grayscale image. This 2D-SSA method is also effective for noise-robust feature extraction [191]. Hence, in this section, we employ the 2D-SSA to filter out the noises and accentuate the structural and contour information of offshore infrastructure.

In the 2D-SSA filtering algorithm, the degree of filtering of SAR images is controlled by two parameters, the number of components and the size of the filtering window. In this chapter, we use the first component and window size 5×5 to remove the noises and smooth the image as much as possible. The determination of these parameters is illustrated in Figs. A.3.1-A.3.2 of the Appendix 3.
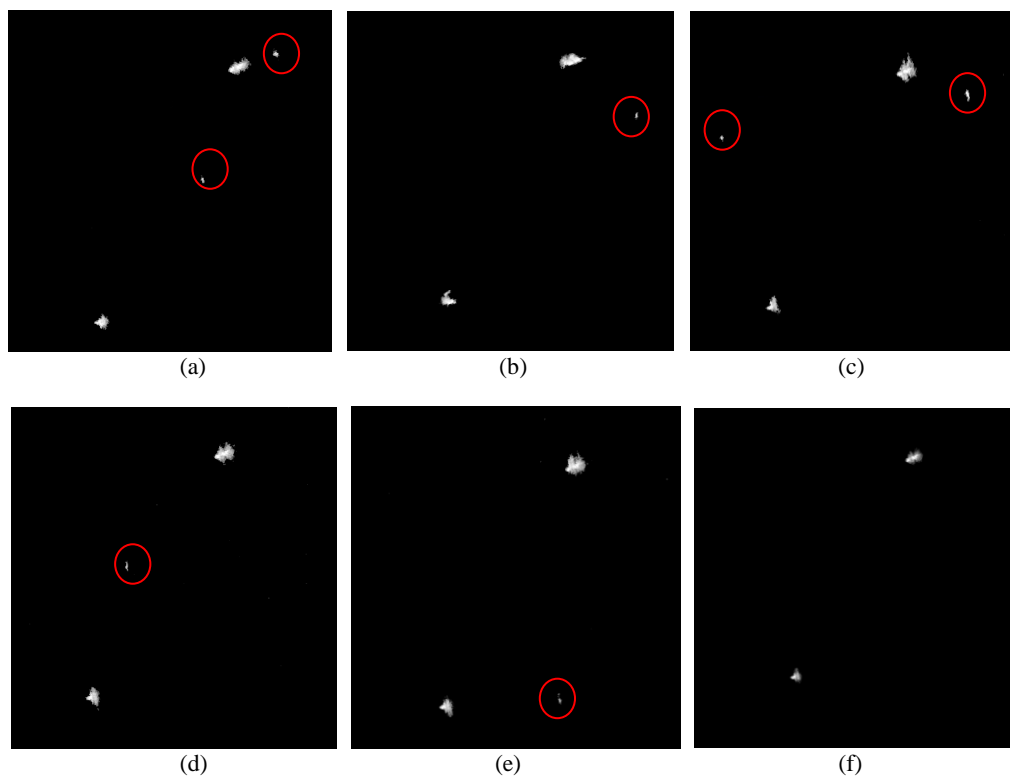
Fig. 5.3 Offshore platforms and false positives (vessels and noises) in the Sentinel-1 data: (a) imaged on Jun. 20, 2020; (b) imaged on Aug. 19, 2020; (c) imaged on Oct. 18, 2020; (d) imaged on Dec. 17, 2020; (e) imaged on Feb. 15, 2021; (f) the transformed median composite image of five time-series data.
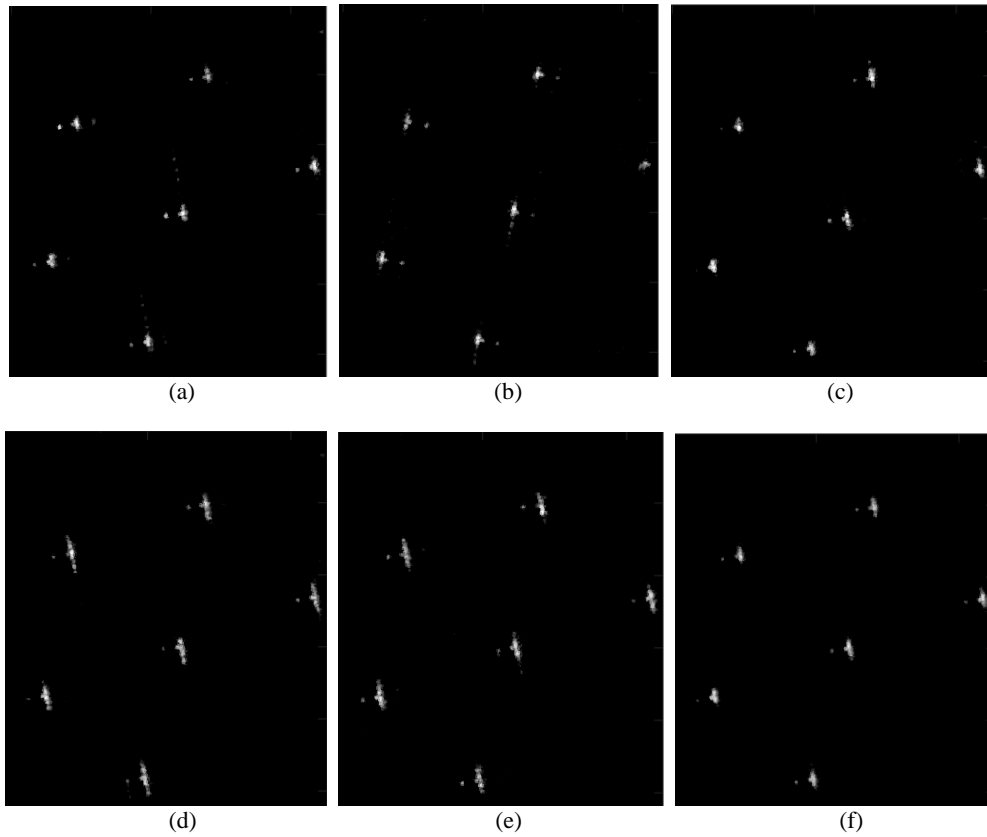
Fig. 5.4 Offshore wind turbines in Beatrice wind farm in the Sentinel-1 data: (a) imaged on Jun. 20, 2020; (b) imaged on Aug. 19, 2020; (c) imaged on Oct. 18, 2020; (d) imaged on Dec. 17, 2020; (e) imaged on Feb. 15, 2021; (f) the transformed median composite image of five time-series data.

(3) Threshold Segmentation for object detection

After obtaining a filtered image, an adaptive threshold value is applied to extract the pixels with higher brightness. Rather than using a fixed cut-off value for all scenes, here we employ the widely used method, OTSU [192-194] to adaptively calculate the optimal threshold for each image by maximizing the weighted sum of between-class variance of foreground and background. First, OTSU is applied to obtain the threshold value. Then, the pixels with intensity values higher than threshold are considered as candidate pixels for offshore infrastructure. In Fig. 5.5, we apply the OTSU method for the threshold segmentation on 2D-SSA filtered images of the linked platforms Clair Ridge DP and Clair Ridge QU, and the wind turbine BE-A5 in Beatrice wind farm. From Figs. 5.5 (a) and (f), there is lots of noise remaining in the median composite image, especially on the edges of the object. We can find from Figs. 5.5 (c) and (h) that the 2D-SSA filter can effectively smooth the median composite image especially

on the edge area. When applying the threshold segmentation, the detection result on 2D-SSA filtered image as shown in Figs. 5.5 (d) and (i) is better than that in Figs.5.5 (b) and (g), where many noises are generated at the edges, even on the ocean background (marked with red circle). Based on the detection result in Figs. 5.5 (d) and (i), the contour range can be acquired as shown in Figs. 5.5 (e) and (j). From Fig. 5.5, for the different kinds of offshore infrastructure with varying characteristics, the OTSU method exhibits effective performance in selecting a proper threshold to extract the contour ranges. However, due to the low spatial resolution, it is difficult to detect the location of each platform from the linked platform's structure as shown in Figs. 5.5 (a-e). That is, the linked platforms are identified as one object.

(a) (b) (c) (d) (e)

(f) (g) (h) (i) (j)
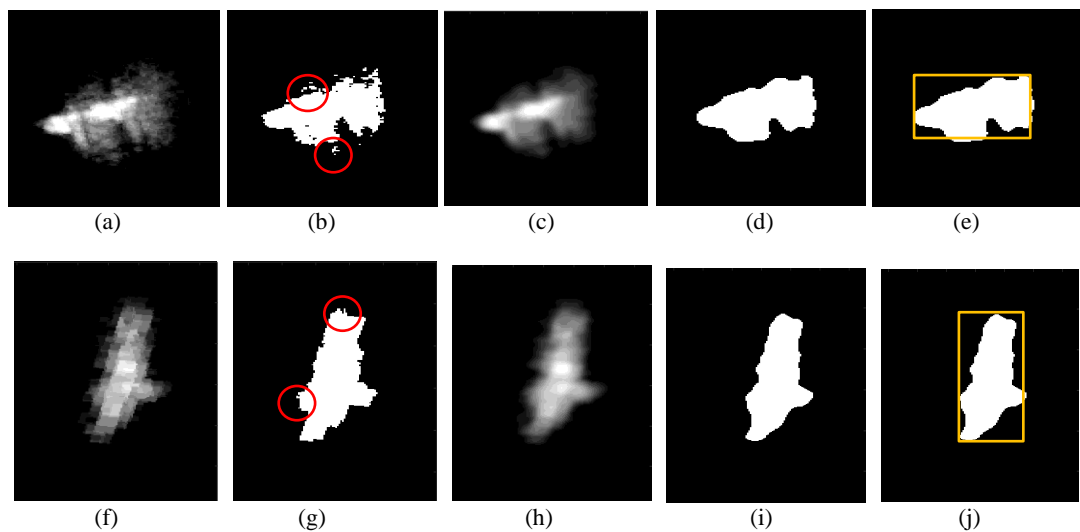
Fig. 5.5 The 2D-SSA filtering and threshold segmentation results: (a) The median composite image of the linked platforms Clair Ridge DP and Clair Ridge QU; (b) Threshold segmentation results on (a); (c) The 2D-SSA filtered image of (a); (d) Threshold segmentation results on (c); (e) The detected contour range on (d); (f) The median composite image of the wind turbine BE-A5; (g) Threshold segmentation results on (f); (h) The 2D-SSA filtered image of (f); (i) Threshold segmentation results on (h); (j) The detected contour range on (i).

5.2.1.2 Precise location detection on Sentinel-2 data

The Sentinel-2 Level 2A true colour data without cloud-cover for different offshore infrastructure from March 2020 to January 2022 are used. Knowing the approximate location, structural features of offshore infrastructure can now be extracted from Sentinel-2 images (Fig. 5.6 (b)). From Fig.5.6 (a) and (b), it is clear that the Sentinel-1 detection has indicated a larger size than in the Sentinel-2 image. This is mainly due to the wake detected around the oil/gas platforms in the Sentinel-1 data. Given this, in

106

this section, the detected contour range on Sentinel-1 data is recognized as a 'guide area' to quickly locate the offshore candidates in Sentinel-2 data. Then, the pixels within the each 'guide area' on Sentinel-2 data are further analysed to acquire the precise location, and to locate single platforms within linked structures.

Here, we only use the blue (Band #2), green (Band #3) and red (Band #4) bands with higher spatial resolution of Sentinel-2, i.e., the true colour image of Sentinel-2 data. The improved spatial resolution can help to detect more structural information and boundary details, which is beneficial for the next location calculation and further size evaluation. Then, morphological reconstruction techniques [195, 196] are applied on Sentinel-2 image to remove small blemishes on the surface of infrastructure without affecting the overall shapes. Specifically, the opening reconstruction operation is first performed by using the morphological erosion and reconstruction. The erosion aims to eliminate the maximum noise that is smaller than predefined structural elements. Then, through using the original input image before erosion as a mask, the reconstruction operator is used to maintain the overall shapes. And then, the closing reconstruction operation is performed by using the morphological dilation and reconstruction. This step can remove the dark noise and the irregular interference that are smaller than the structural elements [197]. In this chapter, we use a disc structural element for experiment because it satisfies the rotation invariance which avoids the distortion of image features [197]. Through the reconstruction-based opening and closing operations, the local maximum and minimum are modified, i.e., the intensity of target reaches the local maximum. As shown in Fig. 5.6 (d), the surfaces of two platforms have high homogeneity and exhibit local maxima in the image, while the boundary details are maintained. Then, by identifying the regional intensity maxima, the two platforms can be easily extracted, as shown in Fig. 5.6 (e). Apart from the single oil/gas infrastructure and wind turbine, there are some platforms linked with bridges. In order to exclude the bridge parts between platforms, a morphological opening operation is further applied on the binary image Fig. 5.6 (e) with a small disc structural element. This operation is implemented by an erosion followed by a dilation, which performs effectively in removing small objects from the foreground edges and placing them in the background [198]. Specifically, the erosion operation can remove pixels of bridges but also affects the edges of the oil/gas platform. The following

dilation operation can re-add the pixels on edges, which keeps the complete structures of platforms. This is important especially for the further area evaluation of topside of oil/gas platforms. As depicted in Fig. 5.6 (f), the linked two platforms are successfully separated. Though there is not the issue of bridges in other oil/gas infrastructure and wind turbines, this operation does not influence their location detection.

In this chapter, an adaptive radius value of the disc structural element in morphological reconstruction operation is employed. That is, the radius value is set to 2 for infrastructure with the 'guide area' in Sentinel-2 image less than 18 pixels in length or width, while the value of 3 is used for the larger infrastructure. The details on the determination of this parameter are given in Fig. A.3.3 of the Appendix 3. The radius value of disc structural element in morphological opening operation is set to 1. This step aims to remove the thin bridges between the linked platforms. The minimum value of radius is enough to achieve this goal.

| (a) | (b) | (c) | (d) | (e) | (f) |
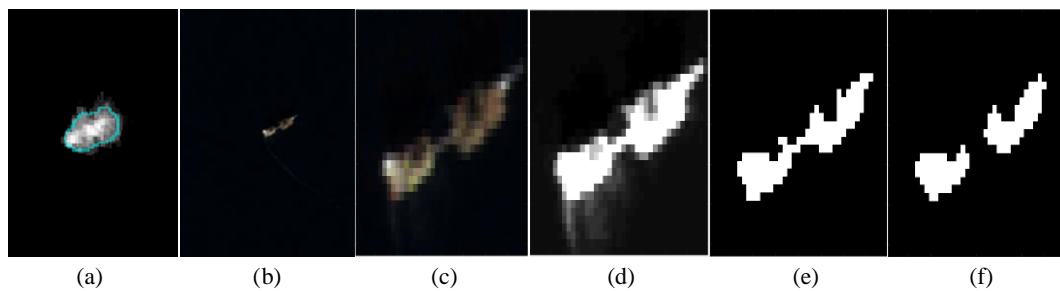
Fig. 5.6. The platform identification from the linked structure of Clair Ridge DP and Clair Ridge QU. (a) The linked structure in Sentinel-1 data covered the latitude from 59.53°N to 59.60°N and longitude from 1.58°W to 1.43°W with contour marked in cyan line, (b) The linked structure in Sentinel-2 true colour image covered the same latitude and longitude range with (a), (c) The image of (b) in 'guide area', (d) The linked structure after morphological reconstruction operation, (e) The detected local maximum results, (f) The separated platforms detection using morphological opening operator.

5.2.2 Size detection in Sentinel-2

In this section, based on the detection results in Section 5.2.1, the topside area of oil/gas platforms and diameter length of wind turbine, is further evaluated.

5.2.2.1 Determining the topside area of oil/gas platforms

In the Sentinel-2 images, the topside area (defined at the planform area above sea level) of the oil/gas platform can be calculated based on the image spatial resolution. Given

the spatial resolution is r (meter), the topside area of the corresponding surface, s, of one pixel in Sentinel-2 image is defined as follows:

$$s = r^2 \qquad (5.1)$$

After the extraction of each platform, the number of identified pixels is then counted. From Equation (5.1), the topside area of the identified platform is calculated as

$$S = \sum_{n=1}^{N}(s_n) \qquad (5.2)$$

where S donates the topside area of one oil/gas platform and N is the number of detected pixels on Sentinel-2 data.

5.2.2.2 Estimating the diameter of wind turbines

Wind turbines in Sentinel-2 images have small topside area, with slender blades. Fig. 5.7 (a) shows the diagram of the wind turbine structures and diameter dimension, and so rather than evaluating the topside area, this chapter aims to extract the diameter size of the wind turbine. In the Sentinel-2 image, we can observe the structures of blades (highlighted with a yellow rectangle in Fig. 5.7 (c)) and nacelle (marked with red circle in Fig. 5.7 (c)) of the wind turbine. Due to the rotation of the turbine, the blades may not present their maximum lengths on image, which can lead to errors in measuring the diameter. Therefore, in this chapter, for each wind turbine, the Sentinel-2 image that presenting long blades is selected. The diameter length is calculated as the twice of the length of the longer blade of one wind turbine. In order to realize this, a morphological construction operation with the structural element size of 2 is applied on Sentinel-2 image. The large structural element would lead to the important feature loss of wind turbine during the detection. Then, regional maxima extraction operation is employed to detect the whole structure of wind turbine, on which the location of two blades can be identified by setting a bounding box as depicted in Fig. 5.7 (d). Then we use a morphological erosion operation with disc structural element to erode the slender blades and detect the centre of nacelle parts. The radius value is empirically set to 2. As shown in Fig. 5.7 (d), the detected whole wind turbine structure is highlighted in grey and the pixels of nacelle centre parts detected by erosion operation are marked in

white. Through using the locations of nacelle pixels and bounding box, the diameter length is acquired.
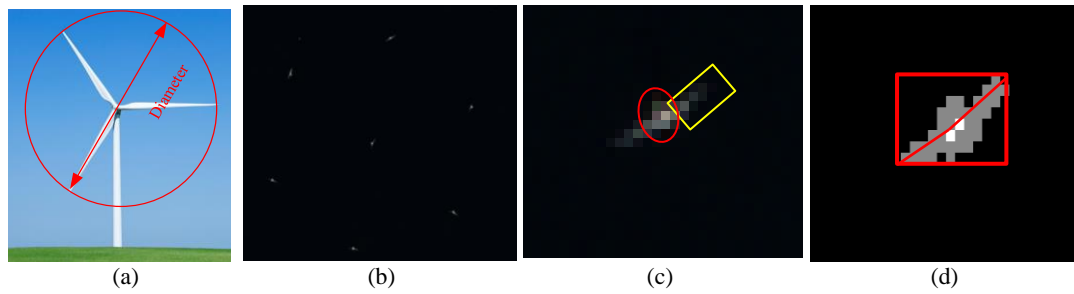
Fig. 5.7. The diameter length evaluation of wind turbines: (a) Wind turbines diagram; (b)The true color Sentinel-2 image of some wind turbines; (c) One zoomed in wind turbine with blade highlighted with yellow rectangular and nacelle marked with red circle. (d) The detected wind turbine structure and bounding box settings.

5.2.3 Postprocessing and validation

A mask generated using EEZ and baseline data is employed. The performance of the proposed method is investigated including the accuracy evaluation on the location and size detection of offshore infrastructure in the study area. In order to quantitatively evaluate the performance of the proposed method on location detection of offshore energy infrastructure, the overall accuracy, detection probability, commission error rate and omission error rate are employed. The overall accuracy is calculated as the ratio between the number of correctly detected infrastructure and the actual total number in ground truth. The detection probability of is the percentage of correctly identified number for each type of offshore infrastructure. The commission error rate refers to the ratio between the number of misidentified infrastructure and the total number. The omission error rate indicates the proportion of the failed to extracted infrastructure number to the total number. In addition, for the size detection accuracy, the size error (SE) and mean size error (MSE) are calculated. The SE indicates the difference between the extracted size by the proposed method and the actual size of each infrastructure. The MSE denotes the average SE value for all extracted offshore infrastructure. Since that the actual size of different offshore infrastructure is varying, the size error rate (SER) is also computed as the ratio of SE and actual size, as well as the mean size error rate (MSER) referring to the average SER for all detected infrastructure. The proposed method is implemented using the Matlab 2018a platform

on a computer with an Intel (R) Core (TM) i7-8700 CPU (3.20 GHz) and 16.0 GB of memory.

5.3 Results

5.3.1 Detection accuracy analysis

The location detection accuracy of the proposed method is first evaluated. If the ground truth location of one offshore installation is within the detected contour range, then it is considered to be correctly identified. More illustrations on this are given in Fig. A.3.4 of the Appendix 3. Otherwise, this detection is regard as an error in location detection. If other objects, like noises or ships, are extracted as offshore energy infrastructure, these detections are recognized as misidentifications. In the ground truth data, there are 102 oil/gas platforms, 19 semi-permanent objects, 86 wind turbines and two offshore transformer modules (OTMs) in the Beatrice wind farm, 100 wind turbines and three offshore substation platforms (OSP) in Moray East wind farm, 5 wind turbines in HyWind wind farm, 5 wind turbines in Kincardine wind farm and 11 wind turbines in Aberdeen wind farm. That is, there are 333 different bits of offshore infrastructure in the study area. By combining the Sentinel-1 SAR data and Sentinel-2 MSI data, our method correctly detects 329 objects with four omissions and zero misidentification. The four omissions are all from bridge-linked platforms and will be discussed later. Thus, for all offshore infrastructure in Scottish waters, the overall accuracy is 98.80% and the commission error rate is 0%. Specifically, the detection probability is 100% and 96.69% for offshore wind turbines and oil/gas infrastructure, respectively. More details on these omissions are considered in Section 5.4. Fig. 5.8 illustrates the spatial distribution of the detection results, while the detected contour range details is given in Tables A.2.7-A.2.12 of the Appendix 2. The proposed method has detected various offshore infrastructure including oil/gas platforms, wind turbines and some semi-permanent objects like floating production storage and offloading (FPSO) vessels and floating storage unit (FSU). As shown in Fig. 5.8, the correct identification offshore infrastructure is marked with red dot and omissions are denoted by yellow dots. The zoomed in images for areas A and B of Fig. 5.8 illustrate the detected spatial distributions of offshore structures in the west and east of Shetland, respectively. The zoomed in images of areas C and D show the detection in the east

and south-east part of EEZ, from which we can find the distribution of omitted structures. The zoomed in image for area E presents the wind turbines distribution in the Beatrice offshore wind farm and Moray East offshore wind farm. The zoomed in image for area F shows the spatial distribution of infrastructure in Aberdeen offshore wind farm and Kincardine offshore wind farm. From Fig. 5.8, it is clear that most offshore infrastructure are located in the eastern waters of Scotland. This intensive distribution results in more background noise and moving vessels. Meanwhile all the wind turbines are all correctly identified.
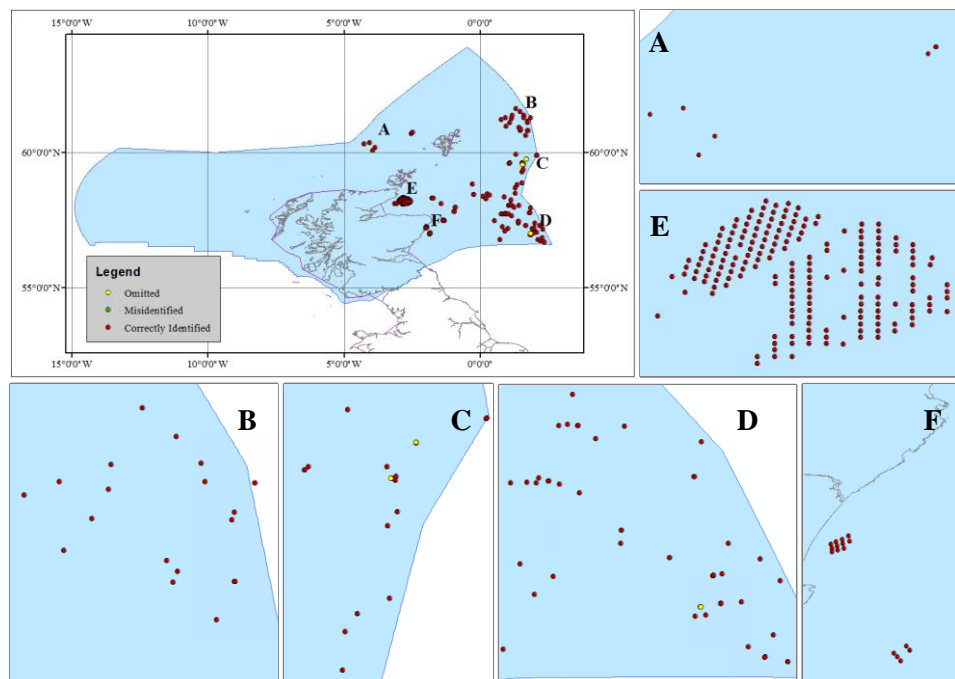
Fig. 5.8. Offshore infrastructure detection results by our proposed method.

5.3.2 Evaluation of estimated size accuracy

5.3.2.1 Size accuracy of the topside of oil/gas platform and semi-permanent objects

The calculated topside area of all correctly identified oil/gas platforms and semi-permanent infrastructure are listed in Table A.2.13 of the Appendix 2. The size evaluation accuracies are summarized in Table 5.1 and Table 5.2. Since the spatial resolution is 10 meters, the area size of the corresponding surface for one pixel is 100 square meters (m2). As shown in the tables, our proposed strategies for evaluating the topside area achieve promising results. Our method has detected 19 semi-permanent

objects and 98 oil/gas platforms. Among them, there are 12 detected rigs, i.e., Ninian north, Northern Producer, Brent Bravo, Brent Delta, Beatrice Charlie, Betrice Alpha Drilling, Beatrice Alpha Production, Beatrice Bravo, Manifold and Compression Platform 01 (MCP01), Frigg Treatment platform 1 (TP1), Frigg Concrete drilling platform 1 and Frigg Treatment Compression Platform 2 (TCP 2), have undergone decommissioning in recent years with many structures have been removed or partially removed. For these decommissioning structures, accurate detection of cut legs above the water is of minor importance in documenting offshore energy infrastructure, as this is a temporary state during the decommissioning process. Final decommissioning in the North Sea requires that all platforms are either fully removed, or cut to footing below the sea surface with no surface elements remaining. In this chapter, we exclude such objects in size evaluation. Therefore, the topside sizes of 86 oil/gas platforms and 19 semi-permanent objects are evaluated here.

As shown in Table 5.1, on 18 out of 86 rigs (the probability of 20.93%), the size error is lower than 100 square meters, i.e., less than one pixel in Sentinel-2 images. On 69 oil/gas platforms with the probability of 80.23%, the SE is lower than 300 square meters, i.e., 3 pixels. On the other hand, more than 5 pixels SE is generated on one rig, namely Bruce Process, Utilities and Quarters (PUQ). This platform is linked with Bruce Compression Reception (CR) and Bruce Drilling. The linked rigs usually exhibit large contour range in Sentinel-1 data, which leads to high radius value setting of structural element in morphological reconstruction operation. The smaller one in the linked rigs will be recognized as a larger size than its actual area value (The effects of radius settings on size estimate of offshore infrastructure can be found in Fig. A.3.3 of the Appendix 3). Overall, the MSE on the oil/gas platforms is 204.1 m2, i.e., about 2 pixels in Sentinel-2 images. This validates the effectiveness of our proposed method. With regard to the SER given in Table 5.2, there are six infrastructure (probability of 6.98%) on which the SER is lower than 1%, while 76 structures (probability of 88.37%) have SER smaller than 10%. On three infrastructure (probability of 3.49%), the SER is larger than 20%, which includes Beryl Alpha, Beryl Single Point Mooring (SPM)-3 and Forties Unity with SER of 21.57%, 30.56% and 23.46%, respectively. Here, Beryl Alpha platform is a linked rig. The Beryl SPM-3 and Forties Unity have small topside sizes. Thus, even they show small size error around 3 pixels in Sentinel-2 image, the

size error rates are still high and further increase the mean size error rate. On the contrary, the mentioned above infrastructure Bruce PUQ which shows high size error presents smaller size error rate than 13%. This is mainly because that it has a large actual topside size. These results further validate the challenges of estimating size on linked rigs. More details on the infrastructure with large SE and SER are discussed in Section 5.4.

Table 5.1 The number of offshore infrastructure with different size error (SE) and the mean size error (MSE) for all oil/gas platforms and semi-permanent objects.

	SE < 100 m^2	SE < 300 m^2	SE > 500 m^2	MSE
Oil/gas platform	18	69	1	204.1
semi-permanent object	1	7	9	1270.6

Table 5.2 The number of offshore infrastructure with different size error rate (SER) and the mean size error rate (MSER) for all oil/gas platforms and semi-permanent objects.

	SER < 1%	SER < 10%	SER > 20%	MSER
Oil/gas platform	6	76	3	5.64%
semi-permanent object	1	15	4	14.02%

As for the topside area estimate of semi-permanent objects, only one out of 19 (probability of 5.26%) are achieved lower SE than one pixel in Sentinel-2 images, while 7 out of 19 (probability of 36.84%) are obtained lower error than 300 square meters (3 pixels in Sentinel-2 image). There are 9 objects (probability of 47.37%) detected higher SE than 500 square meters (5 pixels in Sentinel-2 image). In contrast to the oil/gas platforms with fixed location, the semi-permanent objects would drift with waves. In the Sentinel-1 time-series images, only the parts of semi-permanent objects with high repetition are detected. Therefore, the detected contour range in Sentinel-1 is too small to extract the whole size of these objects in Sentinel-2. The obtained mean size error is 1270.6 square meters (around 13 pixels in Sentinel-2 image), which is higher than that of oil/gas platforms. Similarly, these semi-permanent structures present high MSER of 14.02% as listed in Table 5.2. Here, 4 objects (probability of 21.05%) show higher SER than 20% including Alba FPSO, FPF1 FPSO,

Pierce FPSO and Culzean FPSO. Our method only detects their partial structures due to the limited contour range. They also show higher SE than 5 pixels in Sentinel-2 image, which significantly increase the MSE and MSER results for semi-permanent objects. However, the other 15 (probability of 78.95%) semi-permanent objects all show lower SER than 10%. That is, most semi-permanent objects can achieve promising SER result.

5.3.2.2 Accuracy of estimated diameter of the wind turbines

In order to evaluate the diameter length, the different Sentinel-2 images with wind turbines presenting blades of the maximum length are selected. Due to the spatial resolution of 10 meters, the calculated length which is less than one pixel is presented as ± 5 meters. Table 5.3 summarizes the evaluation results of diameter length for wind turbines. The detected results in all wind farms are given in Table A.2.14-2.18 of the Appendix 2. The actual diameter length in different wind farms is varying in the Scottish waters. Specifically, the actual sizes of diameters in Beatrice offshore wind farm, Moray East offshore wind farm, HyWind offshore wind farm, Kincardine offshore wind farm and Aberdeen offshore wind farm (Aberdeen Bay) are 154 meters, 164 meters, 154 meters, 164 meters and 150 meters, respectively.

Table 5.3 The number of wind turbines with different diameter lengths and the MSE (MSER in parentheses) for all wind turbines in each wind farm.

Name (The number of wind turbines)	SE≤5±5m	SE≤10±5m	SE≤20±5m	SE≤30±5m	MSE (MSER)
Beatrice (86)	22	55	86	86	9.8 ± 5 m (6.36%)
Moray East (100)	10	54	94	100	11.3 ± 5 m (6.91%)
HyWind (5)	0	5	5	5	8.4 ± 5 m (5.45%)
Kincardine (5)	0	4	5	5	8.8 ± 5 m (5.37%)
Aberdeen (11)	10	10	11	11	5.9 ± 5 m (3.94%)
Summary (207)	42	128	201	207	10.3 ± 5 m (6.45%)

In the Beatrice offshore wind farm, there are 86 wind turbines apart from the two OTMs. Among them, the size error of diameter length estimate on 22 wind turbines with the probability of 25.58% realizes less than 5 ± 5 meters (SER < 3.25%). On 55 wind turbines, the errors are lower than 10 ± 5 meters (SER < 6.49%). In addition, the SE of all wind turbines in Beatrice Offshore Wind farm is lower than 20 ± 5 meters (SER < 12.99%), i.e., 2 pixels in Sentinel-2 images. Overall, the MSE of wind turbines in Beatrice Offshore Wind farm is 9.8 ± 5 meters (MSER is 6.36%), which is around one pixel in the Sentinel-2 images. In Moray East offshore wind farm, there are 100 wind turbines and three OSPs. On 10 out of 100 wind turbines (the probability is 10%), the SE is lower than 5 ± 5 meters (SER < 3.05%). There are 54 wind turbines (the probability is 54%) with SE lower than 10 ± 5 meters (SER < 6.10%) and 94 wind turbines with SE lower than 20 ± 5 meters (SER < 12.20%). No wind turbine is estimated with SE larger than 30 ± 5 meters. The MSE is around one pixel in Sentinel-2 image. For the HyWind offshore wind farm and Kincardine offshore wind farm, the proposed method fails to evaluate the diameter length with SE lower than 5 ± 5 meters. However, all wind turbines in HyWind offshore wind farm show SE lower than 10 ± 5 meters (SER < 6.49%). The MSE is less than one pixel in Sentinel-2 image. In the Kincardine offshore wind farm, all wind turbines present SE lower than 20 ± 5 meters (SER < 12.20%), while most wind turbines (the probability is 80%) are estimated with SE lower than 10 ± 5 meters, i.e., SER smaller than 6.10%. In Aberdeen offshore wind farm, on 10 out of 11 wind turbines (the probability is 90.91%), the SE is lower than 5 ± 5 meters (SER < 3.33%). One wind turbine shows a larger SE than 10 ± 5 meters (SER > 6.67%).

In summary, there are 207 wind turbines in the study area. On more than half (the probability is 61.84%) of wind turbines, the SE is lower than 10 ± 5 meters. Most wind turbines show SE lower than 20 ± 5 meters, i.e., two pixels in the Sentinel-2 image. The MSE and MSER for wind turbines in the whole Scottish waters are 10.3 ± 5 meters and 6.45%, respectively. Though the wind turbine has different diameter length in different offshore wind farm, their MSEs are all less than 20 ± 5 meters and MSERs are lower than 7%. These results further validate the effectiveness of our proposed

method in the size evaluation of offshore infrastructure. It provides the potential for monitoring and analysing the wind turbine blades in the future.

5.4 Discussion

Fig. 5.9 shows the cases of omissions in the location detection and infrastructure with large size error in Sentinel-1 (Fig. 5.9. (a)), Sentinel-2 (Fig. 5.9. (b)) and final detection results (Fig. 5.9. (c)). For the location detection, there are four omissions that all from platform complexes, i.e., linked oil/gas platforms with bridges. As shown in Fig. 5.9 (b), our method fails to identify the platform Beryl flare in the infrastructure #1 and platforms Elgin A WHP and Elgin B WHP in the infrastructure #3 (marked in yellow circle). These three omissions are omitted in the regional maxima extraction operation. Their intensity values are not modified as local maxima in the proposed morphological reconstruction operation, which is mainly due to the high intensity heterogeneity in the platforms and linked bridges. In this study, the structural element used in the morphological reconstruction operation is set to a fixed value for each infrastructure, which fails to deal with the complex intensity variety within the linked gas/oil platforms with bridges. In the infrastructure #2, which consists of platforms Bruce PUQ, Bruce CR and Bruce D, the platforms Bruce CR and Bruce D are identified as one structure. It is clear from Fig. 5.9 (b) that these two platforms are very close to each other. In the proposed method, the morphological opening operation which sequentially erode and dilate pixels, re-links these two platforms finally.

On some offshore infrastructure the size error is large. The infrastructure #4 is the Beryl SPM -3, which has significant smaller size than the oil/gas platform. Due to the small size, weak intensity and 2D-SSA filter used in the proposed method, the detected contour range is limited in Sentinel-1 data. As shown in Fig. 5.9 (c), based on the 'guide area' obtained from Sentinel-1 data, only part of the structure is detected and evaluated in Sentinel-2 image. As a result, the structure is successfully detected whereas large size error rate appears. In contrast to the fixed position of oil/gas platform and wind turbine, most semi-permanent objects are floating steel, which makes them easily drift with waves. After the median composite, only the area with high appearance frequency of these floating objects can be detected as the contour range, which inevitably narrows the 'guide area' in Sentinel-2 images. The detection

result of infrastructure #5, namely Haewene Brim FPSO, is illustrated in Fig. 5.9. By comparing Fig. 5.9 (a) and Fig. 5.9 (b), it is clear that this FPSO has shifted a bit over time. As a result, only a small part is extracted as shown in Fig. 5.9 (c), which significantly increases the size error evaluation. The infrastructure #6 is the wind turbine BE-G12 in the Beatrice offshore wind farm. As shown, the proposed method fails to extract the nacelle part correctly, which leads to the error in blade length estimate and finally obtain a short diameter size. For most wind turbines, the generated size error is mainly due to the inaccurate detected location of nacelle parts.
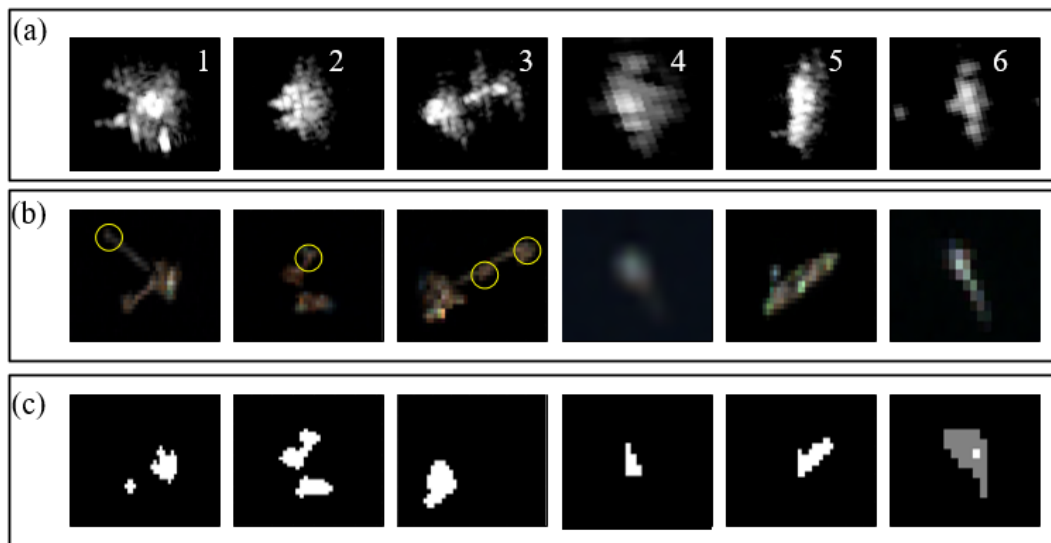
Fig. 5.9. The different kinds of offshore infrastructure in Sentinel-1 (a), Sentinel-2 (b) and detection results (c).

5.5 Summary

By combining the Sentinel-1 and Sentinel-2 data, the locations and sizes of oil/gas platforms, wind turbines and semi-permanent objects can be more accurately extracted than only using one modality of data. As for the location detection, all the wind turbines and semi-permanent objects had been successfully identified whilst four rigs in linked oil/gas platform were omitted. A detection accuracy of 98.80% was achieved for 333 offshore infrastructure in Scottish waters. The mean size errors for wind turbine, oil/gas platform and semi-permanent object were around 1, 2 and 13 pixels, respectively in the Sentinel-2 image, whereas the size error rate was less than 10% for most of structures. These results demonstrated that our proposed method was effective

for the automatic offshore infrastructure detection and evaluation in a vast sea area, which met the needs for practical applications.

6   Conclusion and future work

6.1 Conclusion

The general objective of this thesis is to develop new methods for effective Earth observations, where the advantages and limitations of the hyperspectral images, multispectral images and SAR data are fully explored. Accordingly, novel feature extraction methods are proposed for the classification of HSI data and object identification on SAR and MSI data as presented in Chapters 3, 4 and 5, respectively. The main contributions of this thesis as presented in these chapters can be summarized as follows.

1) In Chapter 3, a novel superpixelwise multi-scale Prophet model (SMP) is proposed for the feature extraction and data classification of hyperspectral images. It is the first time that the Prophet model is applied to HSI analysis, which shows exceptional ability in increasing the interclass diversity and intraclass similarity of HSI data. Besides, it can extract the noise-robust trend components from the uncorrected HSI dataset without removing water-absorption and noisy bands. By combining the spatial features obtained from superpixels and multiscale spectral features derived by the Prophet model and the multiscale strategy, the proposed method can adaptively extract multiscale trend components based on the characteristics of the input data. The fusion of trend components in different scales can extract effective features under unknown noise levels, which is beneficial to HSI classification. With both superpixelwise spatial-spectral feature-level fusion and decision-level fusion, the proposed framework is found to be effective for HSI classification even under limited training samples, which has outperformed a number of state-of-the-art approaches including conventional spectral-spatial classifiers, HSI noise removal methods and several deep learning models as evaluated on three publicly available datasets.

2) Chapter 4 presents a noise-robust feature extraction and dimension reduction method, namely multi-scale 2D-SSA with PCA approach (2D-MSSP). The multiscale strategy is used to extract spatial features in different scales, which can effectively

obtain the discriminative features under various noise levels. This is beneficial to the classification of complicated HSI datasets in high dimensions. By combining with the PCA technique in the spectral domain, the proposed 2D-MSSP model can simultaneously derive the informative spatial-spectral features whilst removing the noisy content and reducing the computational burden. Therefore, it is an effective and efficient noise-robust model for feature extraction and classification of HSI especially on the uncorrected HSI datasets without removing severely noisy and water absorption bands. Through integrating feature-level and decision-level fusion, our 2D-MSSP method can achieve effective classification with limited training data. Results on three publicly available datasets have validated its superiority, which outperforms several state-of-the-art spatial-spectral classifiers and even deep learning models.

3) In Chapter 5, an effective and efficient approach combining the Sentinel-1 SAR and Sentinel-2 MSI data is proposed for the geolocating and measuring of offshore infrastructure in Scottish waters, where the advantages and limitations of MSI and SAR data are fully analysed. For each scene, only five Sentinel-1 time series data and one Sentinel-2 image is utilised. The spectral features through median composite strategy and spatial structural features via 2D-SSA filtering are extracted on the Sentinel-1 data, along with the adaptive thresholding segmentation using OTSU. The Sentinel-2 images have high spatial and spectral resolutions. The morphological operations used can better smooth image details and derive the structural information of offshore infrastructure, especially the linked ones. Quantitative evaluation by comparing with the actual spatial location of offshore installations have fully validated the promising performance of the proposed method.

6.2 Future Work

Although the proposed approaches have achieved improved performance over a number of state-of-the-arts, due to limited time and resources, especially the effect of the pandemic, there remain various limitations in different aspects that can be further enhanced in the future work as detailed below.

1) The proposed SMP method in Chapter 3 has validated the potential of the Prophet model in hyperspectral imaging. Although the Prophet model can decompose the

signal into several components including trend, periodic seasonality, holiday effects and errors as described in Chapter 3.2, in this thesis, only the trend components are taken into consideration for feature extraction. As the spectra in HSI does not present periodic changes, the adjacent bands of one pixel vector or the neighbouring pixels in one band image usually show high similarity. Therefore, it is recommended that future work can focus on the investigation of quasi-periodic seasonality of HSI data to better understand the intensity changes in spectral and spatial domain. This can be combined with band grouping, band selection and image segmentation approaches to derive more discriminative features [199, 200]. In addition, the Prophet model also shows promising capability in filtering outliers to recover the missing data by prediction. This will also be explored as the future work, which can be particularly useful in some interested applications of HSI, such as missing data prediction and recovery, and HSI reconstruction [201].

Besides, for the superpixel segmentation used in Chapter 3 to characterize the spatial distributions of objects, the superpixel scale is set to a constant by trials. However, ideally, this should be adaptively determined to different datasets. This scale value would change when applied the proposed method on the other scene. Hence, in future research, automatic and adaptive determination of the superpixel scale on the basis of the properties of objects, such as its texture, contrast or entropy values, will be explored.

2) Similar to the Prophet model, the 2D-SSA used in Chapter 4 is also a signal decomposition technique, which can reconstruct the HSI data without removing the noisy bands. The 2D-SSA also presents its ability in extracting the structural information from severely noisy and water absorption bands. The difference between the Prophet model and 2D-SSA is that the number of decomposed components in 2D-SSA can be adjusted. This enables the detailed investigation of the subtle difference between different components. It is recommended that the adaptive choice on the number of decomposed components is desirable for the further analysis.

In addition, the window size is also another key parameter that affects the performance of 2D-SSA, which is usually set to a fix size with a regular shape, e.g. rectangle [20]. However, the objects on HSI images are always irregularly shaped and inconsistently

sized. Thus, the regular window setting for deriving spatial features from complex HSI scenes becomes unsuitable. In Chapter 4, the multiscale strategy is applied to alleviate this issue. In the future, an adaptive window setting can be employed in 2D-SSA for further improved performance. Besides, with regard to the classifier, the ensemble learning will be explored to improve the classification performance instead of the majority voting in multiple classification maps.

3) In Chapter 5, it indicates that combination of the Sentinel-1 and Sentinel-2 images have great potential for monitoring the spatial location and size of different offshore infrastructure. That is, this method can be applied for mapping the global offshore infrastructure and quantifying the contribution of offshore energy infrastructure to ocean sprawl. Further, through mapping these infrastructure in different times, we can understand how the global use of marine space is changing and further provide insights for global marine management.

Although this current work has progressed well on the automatic location and size extraction of offshore infrastructure, there are still several aspects for further improvements in the future, such as the adaptive radius of the structural element in morphological operations, which can improve the accuracy of estimated sizes. In addition, the improvements for distinguishing temporary and semi-permanent objects, such as FPSO, from the oil/gas platforms, could be further refined, especially for possible identification of different types of platforms as well as the mapping of uninhabited offshore islands or even global ocean areas.

References

[1]   A. S. Belward and J. O. Skøien, "Who launched what, when and why; trends in global land-cover observation capacity from civilian earth observation satellites," *ISPRS Journal of Photogrammetry Remote Sensing,* vol. 103, pp. 115-128, 2015.

[2]   P. Kansakar and F. Hossain, "A review of applications of satellite earth observation data for global societal benefit and stewardship of planet earth," *Space Policy,* vol. 36, pp. 46-54, 2016.

[3]   C. Toth and G. Jozkow, "Remote sensing platforms and sensors: A survey," *ISPRS Journal of Photogrammetry Remote Sensing,* vol. 115, pp. 22-36, 2016.

[4]   H. Eija *et al.*, "Digital Airborne Photogrammetry—A New Tool for Quantitative Remote Sensing?—A State-of-the-Art Review On Radiometric Aspects of Digital Photogrammetric Images," *Remote Sensing,* vol. 1, no. 3, pp. 577-605, 2009.

[5]   X. Jin *et al.*, "Estimates of plant density of wheat crops at emergence from very low altitude UAV imagery," *Remote Sensing of Environment,* vol. 198, pp. 105-114, 2017.

[6]   A. Zhang *et al.*, "Coastal wetland mapping with Sentinel-2 MSI imagery based on gravitational optimized multilayer perceptron and morphological attribute profiles," *Remote Sensing,* vol. 11, no. 8, p. 952, 2019.

[7]   B. Tu *et al.*, "Hyperspectral image classification via weighted joint nearest neighbor and sparse representation," *IEEE Journal of Selected Topics in Applied Earth Observations Remote Sensing,* vol. 11, no. 11, pp. 4063-4075, 2018.

[8]   F. Tian *et al.*, "Remote sensing of vegetation dynamics in drylands: Evaluating vegetation optical depth (VOD) using AVHRR NDVI and in situ green biomass data over West African Sahel," *Remote Sensing of Environment,* no. 177, pp. 265-276, 2016.

[9]   Y. Zhou *et al.*, "Positive effects of ecological restoration policies on the vegetation dynamics in a typical ecologically vulnerable area of China," *Ecological Engineering,* vol. 159, p. 106087, 2020.

[10]   G. Mohammad *et al.*, "A Comprehensive Review on Water Quality Parameters Estimation Using Remote Sensing Techniques," *Sensors,* vol. 16, no. 8, p. 1298, 2016.

[11]   S. Singh *et al.*, "Remote sensing and GIS based analysis of temporal land use/land cover and water quality changes in Harike wetland ecosystem, Punjab, India," *Journal of Environmental Management,* vol. 262, p. 110355, 2020.

[12]   H. Hou *et al.*, "Spatiotemporal analysis of urban growth in three African capital cities: A grid-cell-based analysis using remote sensing data," *Journal of African Earth Sciences,* vol. 123, pp. 381-391, 2016.

[13]   O. Derya, "Urban Growth Simulation of Atakum (Samsun, Turkey) Using Cellular Automata-Markov Chain and Multi-Layer Perceptron-Markov Chain Models," *Remote Sensing,* vol. 7, no. 5, pp. 5918-5950, 2015.

[14]   S. Mohan, "Potentials and applications of Microwave remote sensing," in *National Seminar on New Challenges In Remote Sensing Technology With Emphasis on Microwave data*, 2013.

[15] F. Brown, "Review of oil spill remote sensing," *Spill Science Technology Bulletin,* vol. 4, no. 4, pp. 199-208, 1997.

[16] F. Brown, "Review of oil spill remote sensing," *Spill Science Technology Bulletin,* vol. 4, no. 4, pp. 199-208, 1997.

[16] I. H. Woodhouse, *Introduction to microwave remote sensing.* CRC press, 2017.

[17] H. Rueda-Chacon *et al.*, "Compressive spectral image fusion via a single aperture high throughput imaging system," *Scientific Reports,* vol. 11, no. 1, pp. 1-12, 2021.

[18] H. Liang, "Advances in multispectral and hyperspectral imaging for archaeology and art conservation," *Applied Physics A,* vol. 106, no. 2, pp. 309-323, 2012.

[19] R. Qureshi *et al.*, "Hyperspectral Document Image Processing: Applications, Challenges and Future Prospects," *Pattern Recognition,* vol. 90, pp. 12-22, 2019.

[20] J. Zabalza *et al.*, "Novel two-dimensional singular spectrum analysis for effective feature extraction and data classification in hyperspectral imaging," *IEEE Transactions on Geoscience and Remote Sensing,* vol. 53, no. 8, pp. 4418-4433, 2015.

[21] G. Li *et al.*, "Hyperspectral prediction of leaf area index of winter wheat in irrigated and rainfed fields," *Plos One,* vol. 12, no. 8, p. e0183338, 2017.

[22] X. Jia *et al.*, "Feature mining for hyperspectral image classification," *Proceedings of the IEEE,* vol. 101, no. 3, pp. 676-697, 2013.

[23] R. E. Bellman, *Adaptive control processes.* Princeton university press, 2015.

[24] Hughes and G., "On the mean accuracy of statistical pattern recognizers," *IEEE transactions on information theory,* vol. 14, no. 1, pp. 55-63, 1968.

[25] J. Zabalza *et al.*, "Singular spectrum analysis for effective feature extraction in hyperspectral imaging," *IEEE Geoscience and Remote Sensing Letters,* vol. 11, no. 11, pp. 1886-1890, 2014.

[26] Z. Chen *et al.*, "Self-Attention-Based Conditional Variational Auto-Encoder Generative Adversarial Networks for Hyperspectral Classification," *Remote Sensing,* vol. 13, no. 16, pp. 3316, 2021.

[27] S. Jia *et al.*, "Spatial-spectral-combined sparse representation-based classification for hyperspectral imagery," *Soft Computing - A Fusion of Foundations, Methodologies and Applications,* vol. 20, no. 12, pp. 4659-4668, 2016.

[28] Y. Fu *et al.*, "Adaptive spatial-spectral dictionary learning for hyperspectral image restoration," *International Journal of Computer Vision,* vol. 122, no. 2, pp. 228-245, 2017.

[29] Y. Liu *et al.*, "Automatic extraction of offshore platforms using time-series Landsat-8 Operational Land Imager data," *Remote Sensing of Environment,* vol. 175, pp. 73-91, 2016.

[30] R. Dwivedi, "Active Remote Sensing," in *Geospatial Technologies for Land Degradation Assessment and Management*: CRC Press, 2018, pp. 67-96.

[31] X. Shen *et al.*, "Inundation extent mapping by synthetic aperture radar: a review," *Remote Sensing,* vol. 11, no. 7, p. 879, 2019.

[32] T. T. Nguyen *et al.*, "A novel intelligence approach based active and ensemble learning for agricultural soil organic carbon prediction using multispectral and SAR data fusion," *Science of The Total Environment,* vol. 804, p. 150187, 2022.

[33]   Q. Li *et al.*, "Mapping multi-layered mangroves from multispectral, hyperspectral, and LiDAR data," *Remote Sensing of Environment,* vol. 258, p. 112403, 2021.

[34]   Y. Chen and L. Bruzzone, "Self-supervised SAR-optical Data Fusion of Sentinel-1/-2 Images," *IEEE Transactions on Geoscience Remote Sensing,* vol. 60, p. 5406011, 2022.

[35]   S. Casadio *et al.*, "Use of ATSR and SAR measurements for the monitoring and characterisation of night-time gas flaring from off-shore platforms: The North Sea test case," *Remote Sensing of Environment,* vol. 123, pp. 175-186, 2012.

[36]   Y. Liu *et al.*, "Assessment of offshore oil/gas platform status in the northern Gulf of Mexico using multi-source satellite time-series images," *Remote Sensing of Environment,* vol. 208, pp. 63-81, 2018.

[37]   P. E. Posen *et al.*, "Evaluating differences in marine spatial data resolution and robustness: A North Sea case study," *Ocean Coast. Manage.,* vol. 192, pp. 105-206, 2020.

[38]   L. A. Henry *et al.*, "Ocean sprawl facilitates dispersal and connectivity of protected species," *Scientific reports of cetacean research,* vol. 8, no. 1, pp. 1-11, 2018.

[39]   T. Zhang *et al.*, "Global offshore wind turbine dataset," *Scientific Data,* vol. 8, no. 1, p. 191, 2021.

[40]   V. Parente *et al.*, "Offshore decommissioning issues: Deductibility and transferability," *Energy Policy,* vol. 34, no. 15, pp. 1992-2001, 2006.

[41]   Y. Wang and H. Liu, "A Hierarchical Ship Detection Scheme for High-Resolution SAR Images," *IEEE Transactions on Geoscience Remote Sensing,* vol. 50, no. 10, pp. 4173-4184, 2012.

[42]   B. A. Wong *et al.*, "Automating offshore infrastructure extractions using synthetic aperture radar & Google Earth Engine," *Remote Sensing of Environment,* vol. 233, p. 111412, 2019.

[43]   I. Jlliffe, *Principal Component Analysis* (no. 27). Springer 1986, pp. 231-246.

[44]   G. Chen and S. Qian, "Denoising of Hyperspectral Imagery Using Principal Component Analysis and Wavelet Shrinkage," *IEEE Transactions on Geoscience Remote Sensing,* vol. 49, no. 3, pp. 973-980, 2011.

[45]   Z. Y. Liu *et al.*, "Hyperspectral discrimination of foliar biotic damages in rice using principal component analysis and probabilistic neural network," *Precision Agriculture,* vol. 19, no. 6, pp. 973-991, 2018.

[46]   D. W. Sun, *Hyperspectral Imaging for Food Quality Analysis and Control* (Hyperspectral Imaging for Food Quality Analysis). 2010.

[47]   J. Jiang *et al.*, "SuperPCA: A superpixelwise PCA approach for unsupervised feature extraction of hyperspectral imagery," *IEEE Transactions on Geoscience Remote Sensing,* vol. 56, no. 8, pp. 4581-4593, 2018.

[48]   Y. Wang and Y. Zhang, "Nonnegative Matrix Factorization," *IEEE Transactions on Knowledge Data Engineering,* vol. 25, no. 6, pp. 1336-1353, 2013.

[49]   B. Yousefi *et al.*, "Continuum removal for ground-based LWIR hyperspectral infrared imagery applying non-negative matrix factorization," *Applied Optics,* vol. 57, no. 21, pp. 6219-6228, 2018.

[50] P. S. Prasad, *Independent Component Analysis*. Cambridge University Press, 2001.

[51] P. Mishra *et al.*, "Application of independent components analysis with the JADE algorithm and NIR hyperspectral imaging for revealing food adulteration," *Journal of Food Engineering,* vol. 168, pp. 7-15, 2016.

[52] A. A. Nielsen, "Kernel Maximum Autocorrelation Factor and Minimum Noise Fraction Transformations," *IEEE Transactions on Image Processing,* vol. 20, no. 3, pp. 612-624, 2011.

[53] J. Shawetaylor and N. Cristianini, *Kernel Methods for Pattern Analysis: Pattern analysis*. UK: Cambridge Univ. Press, 2004.

[54] B. Scholkopf and A. Smola, "Kernel Principal Component Analysis," in *International Conference on Artificial Neural Networks*, Berlin, Heidelberg, 1997: Springer.

[55] A. Khan *et al.*, "Dimensionality reduction of hyperspectral images using kernel ICA," *Sensing for Agriculture Food Quality Safety and Health,* vol. 7315, pp. 213-220, 2009.

[56] L. Gao *et al.*, "Optimized Kernel Minimum Noise Fraction Transformation for Hyperspectral Image Classification," *Remote Sensing,* vol. 9, no. 6, pp. 548, 2017.

[57] Y. Gu *et al.*, "Multiple Kernel Learning via Low-Rank Nonnegative Matrix Factorization for Classification of Hyperspectral Imagery," *IEEE Journal of Selected Topics in Applied Earth Observations Remote Sensing,* vol. 8, no. 6, pp. 2739-2751, 2017.

[58] J. Zabalza *et al.*, "Fast Implementation of Singular Spectrum Analysis for Effective Feature Extraction in Hyperspectral Imaging," *IEEE Journal of Selected Topics in Applied Earth Observations Remote Sensing,* vol. 8, no. 6, pp. 2845-2853, 2015.

[59] B. Demir and S. Erturk, "Empirical Mode Decomposition of Hyperspectral Images for Support Vector Machine Classification," *IEEE Transactions on Geoscience Remote Sensing,* vol. 48, no. 11, pp. 4071-4084, 2010.

[60] J. Zabalza *et al.*, "Singular Spectrum Analysis for Effective Feature Extraction in Hyperspectral Imaging," *IEEE Geoscience and Remote Sensing Letters,* vol. 11, no. 11, pp. 1886-1890, 2014.

[61] Z. He *et al.*, "Optimized Ensemble EMD-Based Spectral Features for Hyperspectral Image Classification," *IEEE Transactions on Instrumentation Measurement & Control,* vol. 63, no. 5, pp. 1041-1056, 2014.

[62] Z. Wu and N. E. Huang, "Ensemble empirical mode decomposition: a noise-assisted data analysis method," *Advances in adaptive data analysis,* vol. 1, no. 01, pp. 1-41, 2009.

[63] J. A. Richards and X. Jia, *Remote Sensing Digital Image Analysis*. New York: Springer-Verlag, 1999.

[64] A. J. Izenman, "Linear discriminant analysis," in *Modern multivariate statistical techniques*: Springer, 2013, pp. 237-280.

[65] F. K. and M. J. M., "Nonparametric Discriminant Analysis," *IEEE Transactions On Pattern Analysis and Machine Intelligence,* no. 6, pp. 671-678, 1983.

[66]   B. C. Kuo *et al.*, "Nonparametric Weighted Feature Extraction for Classification," *IEEE Transactions on Geoscience Remote Sensing,* vol. 42, no. 5, pp. 1096-1105, 2004.

[67]   L. Wei *et al.*, "Locality-preserving discriminant analysis in kernelinduced feature spaces for hyperspectral image classification," *IEEE Geoscience and Remote Sensing Letters* vol. 8, no. 5, pp. 894-898, 2011.

[68]   B.-C. Kuo *et al.*, "Kernel Nonparametric Weighted Feature Extraction for Hyperspectral Image Classification," *IEEE Transactions on Geoscience Remote Sensing,* vol. 47, no. 4, pp. 1139-1155, 2009.

[69]   J. Feng *et al.*, "Marginal stacked autoencoder with adaptively-spatial regularization for hyperspectral image classification," *IEEE Journal of Selected Topics in Applied Earth Observations Remote Sensing,* vol. 11, no. 9, pp. 3297-3311, 2018.

[70]   T. Zhang *et al.*, "JL-GFDN: A Novel Gabor Filter-Based Deep Network Using Joint Spectral-Spatial Local Binary Pattern for Hyperspectral Image Classification," *Remote Sensing,* vol. 12, no. 12, pp. 2016, 2020.

[71]   C. Shi and C.-M. Pun, "3D multi-resolution wavelet convolutional neural networks for hyperspectral image classification," *Information Sciences,* vol. 420, pp. 49-65, 2017.

[72]   X. Zhang *et al.*, "Multifeature hyperspectral image classification with local and nonlocal spatial information via Markov random field in semantic space," *IEEE Transactions on Geoscience Remote Sensing,* vol. 56, no. 3, pp. 1409-1424, 2017.

[73]   L. Sun *et al.*, "Supervised spectral–spatial hyperspectral image classification with weighted Markov random fields," *IEEE Transactions on Geoscience and Remote Sensing,* vol. 53, no. 3, pp. 1490-1503, 2014.

[74]   L. Fang *et al.*, "Classification of hyperspectral images by exploiting spectral–spatial information of superpixel via multiple kernels," *IEEE transactions on geoscience and remote sensing,* vol. 53, no. 12, pp. 6663-6674, 2015.

[75]   F. Fan *et al.*, "Hyperspectral image denoising with superpixel segmentation and low-rank representation," *Information Sciences,* vol. 397, pp. 48-68, 2017.

[76]   L. Sun *et al.*, "Adjacent superpixel-based multiscale spatial-spectral kernel for hyperspectral classification," *IEEE Journal of Selected Topics in Applied Earth Observations and Remote Sensing,* vol. 12, no. 6, pp. 1905-1919, 2019.

[77]   H. Yu *et al.*, "Multiscale superpixel-level subspace-based support vector machines for hyperspectral image classification," *IEEE Geoscience and Remote Sensing Letters,* vol. 14, no. 11, pp. 2142-2146, 2017.

[78]   H. Lee and H. Kwon, "Going deeper with contextual CNN for hyperspectral image classification," *IEEE Transactions on Image Processing,* vol. 26, no. 10, pp. 4843-4855, 2017.

[79]   M. Zhang *et al.*, "Diverse region-based CNN for hyperspectral image classification," *IEEE Transactions on Image Processing,* vol. 27, no. 6, pp. 2623-2634, 2018.

[80]   Z. Zhong *et al.*, "Generative adversarial networks and conditional random fields for hyperspectral image classification," *IEEE transactions on cybernetics,* vol. 50, no. 7, pp. 3318-3329, 2019.

[81] R. Hang *et al.*, "Cascaded recurrent neural networks for hyperspectral image classification," *IEEE Transactions on Geoscience and Remote Sensing,* vol. 57, no. 8, pp. 5384-5394, 2019.

[82] L. Sun *et al.*, "Fast superpixel based subspace low rank learning method for hyperspectral denoising," *IEEE Access,* vol. 6, pp. 12031-12043, 2018.

[83] W. He *et al.*, "Hyperspectral image denoising via noise-adjusted iterative low-rank matrix approximation," *IEEE Journal of Selected Topics in Applied Earth Observations and Remote Sensing,* vol. 8, no. 6, pp. 3050-3061, 2015.

[84] U. Shaham *et al.*, "SpectralNet: Spectral Clustering using Deep Neural Networks," in *Proc. Int. conf. learn. Representations*, 2018.

[85] E. Torti *et al.*, "Parallel K-means clustering for brain cancer detection using hyperspectral images," *Electronics,* vol. 7, no. 11, pp. 283, 2018.

[86] P. Azimpour *et al.*, "Hyperspectral image clustering with Albedo recovery Fuzzy C-Means," *International Journal of Remote Sensing,* vol. 41, no. 16, pp. 6117-6134, 2020.

[87] B. Tu *et al.*, "Hyperspectral anomaly detection via density peak clustering," *Pattern Recognition Letters,* vol. 129, pp. 144-149, 2020.

[88] H. Xie *et al.*, "Unsupervised Hyperspectral Remote Sensing Image Clustering Based on Adaptive Density," *IEEE Geoence Remote Sensing Letters,* vol. 15, no. 4, pp. 632-636, 2018.

[89] Y. Zhao *et al.*, "Fast spectral clustering for unsupervised hyperspectral image classification," *Remote Sensing,* vol. 11, no. 4, p. 399, 2019.

[90] S. Bhattacharyya *et al.*, "Multilevel Quantum Inspired Fractional Order Ant Colony Optimization for Automatic Clustering of Hyperspectral Images," in *2020 IEEE Congress on Evolutionary Computation (CEC)*, 2020, pp. 1-8.

[91] T. Dutta *et al.*, *Automatic Clustering of Hyperspectral Images Using Qutrit Based Particle Swarm Optimization*. Intelligence Enabled Research, 2020.

[92] M. Zeng *et al.*, "Spectral-Spatial Clustering of Hyperspectral Image Based on Laplacian Regularized Deep Subspace Clustering," in *IGARSS 2019 - 2019 IEEE International Geoscience and Remote Sensing Symposium*, 2019, pp. 2694-2697.

[93] M. M. Fard *et al.*, "Deep k-Means: Jointly clustering with k-Means and learning representations," *Pattern Recognition Letters,* vol. 138, pp. 185-192, 2020.

[94] A. Obeid *et al.*, "Unsupervised Land-Cover Segmentation Using Accelerated Balanced Deep Embedded Clustering," *IEEE Geoscience Remote Sensing Letters,* vol. 19, pp. 1-5, 2021.

[95] Y. Cai *et al.*, "Graph Convolutional Subspace Clustering: A Robust Subspace Clustering Framework for Hyperspectral Image," *IEEE Transactions on Geoscience Remote Sensing,* vol. 59, no. 5, pp. 4191-4202, 2020.

[96] J. Chang *et al.*, "Deep Self-Evolution Clustering," *IEEE Transactions on Pattern Analysis Machine Intelligence,* vol. 42, no. 4, pp. 809-823, 2018.

[97] C. M. Bachmann *et al.*, "Exploiting manifold geometry in hyperspectral imagery," *IEEE Transactions on Geoscience Remote Sensing,* vol. 43, no. 3, pp. 441-454, 2005.

[98] M. Belkin and P. Niyogi, "Laplacian Eigenmaps for Dimensionality Reduction and Data Representation," *J MIT Press,* vol. 15, no. 6, pp. 1373-1396, 2003.

[99]   S. Yan *et al.*, "Graph Embedding and Extensions: A General Framework for Dimensionality Reduction," *IEEE Transactions on Pattern Analysis Machine Intelligence,* vol. 29, no. 1, pp. 40-51, 2007.

[100]   D. Lunga *et al.*, "Manifold-Learning-Based Feature Extraction for Classification of Hyperspectral Data: A Review of Advances in Manifold Learning," *IEEE Signal Processing Magazine,* vol. 31, no. 1, pp. 55-66, 2014.

[101]   M. M. Crawford *et al.*, *Exploring Nonlinear Manifold Learning for Classification of Hyperspectral Data*, Springer Berlin Heidelberg, 2011.

[102]   R. Wang *et al.*, "Fast Spectral Clustering With Anchor Graph for Large Hyperspectral Images," *IEEE Geoscience Remote Sensing Letters,* vol. 14, no. 11, pp. 2003-2007, 2017.

[103]   L. Zhang *et al.*, "Hyperspectral image unsupervised classification by robust manifold matrix factorization," *Information Sciences,* vol. 485, pp. 154-169, 2019.

[104]   G. Camps-Valls *et al.*, "Semi-Supervised Graph-Based Hyperspectral Image Classification," *IEEE Transactions on Geoscience Remote Sensing,* vol. 45, no. 10, pp. 3044-3054, 2007.

[105]   S. Yuanjie *et al.*, "Probabilistic class structure regularized sparse representation graph for semi-supervised hyperspectral image classification," *Pattern Recognition: The Journal of the Pattern Recognition Society,* vol. 63, pp. 102-114, 2017.

[106]   H. Fang *et al.*, "Fast semi-supervised learning with anchor graph for large hyperspectral images," *Pattern Recognition Letters,* vol. 130, pp. 319-326, 2020.

[107]   W. Hao and S. Prasad, "Semi-Supervised Deep Learning Using Pseudo Labels for Hyperspectral Image Classification," *IEEE Transactions on Image Processing,* vol. 27, no. 3, pp. 1259-1270, 2017.

[108]   Y. Wang *et al.*, "A depthwise separable fully convolutional ResNet with ConvCRF for semisupervised hyperspectral image classification," *IEEE Journal of Selected Topics in Applied Earth Observations Remote Sensing,* vol. 14, pp. 4621-4632, 2021.

[109]   L. Zhang *et al.*, "Ensemble manifold regularized sparse low-rank approximation for multiview feature embedding," *Pattern Recognition,* vol. 48, no. 10, pp. 3102-3112, 2015.

[110]   C. Zhao *et al.*, "Classification of Hyperspectral Imagery based on spectral gradient, SVM and spatial random forest," *IInfrared Physics and Technology,* vol. 95, pp. 61-69, 2018.

[111]   S. Subramanian *et al.*, "Methodology for hyperspectral image classification using novel neural network," *Office of Scientific Technical Information Technical Reports,* vol. 3071, pp. 128-137, 2017.

[112]   E. Salas *et al.*, "Modified shape index for object-based random forest image classification of agricultural systems using airborne hyperspectral datasets," *PLoS ONE,* vol. 14, no. 3, pp. 1-22, 2019.

[113]   J. Chen *et al.*, "A Parallel Random Forest Algorithm for Big Data in a Spark Cloud Computing Environment," *IEEE Transactions on Parallel Distributed Systems,* vol. 28, no. 4, pp. 919-933, 2017.

[114] J. Ham *et al.*, "Investigation of the random forest framework for classification of hyperspectral data," *IEEE Transactions on Geoscience Remote Sensing,* vol. 43, no. 3, pp. 492-501, 2005.

[115] A. Mellor *et al.*, "Exploring issues of training data imbalance and mislabelling on random forest performance for large area land cover classification using the ensemble margin," *Isprs Journal of Photogrammetry Remote Sensing,* vol. 105, pp. 155-168, 2015.

[116] W. Sun *et al.*, "Fast and Robust Self-Representation Method for Hyperspectral Band Selection," *IEEE Journal of Selected Topics in Applied Earth Observations Remote Sensing,* vol. 10, no. 11, pp. 5087-5098, 2017.

[117] Y. Zhang *et al.*, "Cascaded Random Forest for Hyperspectral Image Classification," *IEEE Journal of Selected Topics in Applied Earth Observations Remote Sensing,* vol. 11, no. 4, pp. 1082-1094, 2018.

[118] A. Wang *et al.*, "Hyperspectral image classification based on convolutional neural network and random forest," *Remote Sensing Letters,* vol. 10, no. 11, pp. 1086-1094, 2019.

[119] J. Xia *et al.*, "Hyperspectral Image Classification With Rotation Random Forest Via KPCA," *IEEE Journal of Selected Topics in Applied Earth Observations Remote Sensing,* vol. 10, no. 4, pp. 1601-1609, 2017.

[120] J. Xia *et al.*, "Hyperspectral Image Classification With Canonical Correlation Forests," *IEEE Transactions on Geoence Remote Sensing,* vol. 55, no. 1, pp. 421-431, 2017.

[121] B. Liu *et al.*, "Morphological Attribute Profile Cube and Deep Random Forest for Small Sample Classification of Hyperspectral Image," *IEEE Access,* vol. PP, no. 99, pp. 1-1, 2020.

[122] F. Tong and Y. Zhang, "Exploiting Spectral–Spatial Information Using Deep Random Forest for Hyperspectral Imagery Classification," *IEEE Geoscience Remote Sensing Letters,* vol. 19, pp. 1-5, 2021.

[123] J. A. Benediktsson and P. Ghamisi, *Spectral-Spatial Classification of Hyperspectral Remote Sensing Images.* 2015.

[124] P. Ghamisi *et al.*, "Advanced Spectral Classifiers for Hyperspectral Images: A Review," *Geoscience Remote Sensing,* vol. 5, no. 1, pp. 8-32, 2017.

[125] J. Kivinen *et al.*, "Learning with Kernels," *IEEE Transactions on Signal Processing,* vol. 52, no. 8, pp. 2165-2176, 2004.

[126] J. Xia *et al.*, "Rotation-Based Support Vector Machine Ensemble in Classification of Hyperspectral Data With Limited Training Samples," *IEEE Transactions on Geoscience Remote Sensing,* vol. 54, no. 3, pp. 1519-1531, 2016.

[127] X. Zhu *et al.*, "Optimization Performance Comparison of Three Different Group Intelligence Algorithms on a SVM for Hyperspectral Imagery Classification," *Remote Sensing,* vol. 11, no. 6, p. 734, 2019.

[128] O. Onuwa and E. N. Christopher, "Deep support vector machine for hyperspectral image classification," *Pattern Recognition,* vol. 103, pp. 107298, 2020.

[129] Y. Chen *et al.*, "Deep Learning-Based Classification of Hyperspectral Data," *IEEE Journal of Selected Topics in Applied Earth Observations Remote Sensing,* vol. 7, no. 6, pp. 2094-2107, 2017.

[130] J. Zhao *et al.*, "A combination method of stacked autoencoder and 3D deep residual network for hyperspectral image classification," *International Journal of Applied Earth Observation Geoinformation,* vol. 102, no. 4, pp. 102459, 2021.

[131] C. Chen *et al.*, "Hyperspectral Classification Using Deep Belief Networks Based on Conjugate Gradient Update and Pixel-Centric Spectral Block Features," *IEEE Journal of Selected Topics in Applied Earth Observations Remote Sensing,* vol. PP, no. 99, pp. 1-1, 2020.

[132] X. Li *et al.*, "Deep Feature Fusion via Two-Stream Convolutional Neural Network for Hyperspectral Image Classification," *IEEE Transactions on Geoscience Remote Sensing,* vol. 58, no. 4, pp. 2615-2629, 2020.

[133] A. Ma *et al.*, "Fast Sequential Feature Extraction for Recurrent Neural Network-Based Hyperspectral Image Classification," *IEEE Transactions on Geoscience Remote Sensing,* vol. 59, no. 7, pp. 5920-5937, 2020.

[134] C. Xiao, "Self-Attention-Based Conditional Variational Auto-Encoder Generative Adversarial Networks for Hyperspectral Classification," *Remote Sensing,* vol. 13, no. 16, pp. 3316, 2021.

[135] Q. Xing *et al.*, "Remote Sensing of Ships and Offshore Oil Platforms and Mapping the Marine Oil Spill Risk Source in the Bohai Sea," *Aquatic Procedia,* vol. 3, pp. 127-132, 2015.

[136] S. Zhao *et al.*, "Extraction and Monitoring of Offshore Oil and Gas Platforms Based on Landsat Imagery," *Tropical Geography,* vol. 37, no. 37, pp. 112-119, 2017.

[137] Y. Fan and Q. Wang, "A Connected Component Based Offshore Platforms Extraction Method of GF2 Multi-channel Optical Images," *IEEE 4th International Conference on Signal Image Processing,* pp. 916-919, 2019.

[138] Z. Zhu *et al.*, "Offshore Platform Detection Based on Harris Detector and Intensity-Texture Image from Sentinel-2A Image," *10th IAPR Workshop on Pattern Recognition in Remote Sensing,* pp. 1-4, 2018.

[139] H. Zhu *et al.*, "Detecting Offshore Drilling Rigs with Multitemporal NDWI: A Case Study in the Caspian Sea," *Remote Sensing,* vol. 13, pp. 1576, 2021.

[140] T. A. Croft, "Nocturnal Images of the Earth from Space," *Scientific American,* vol. 239, no. 1, pp. 86-101, 1978.

[141] S. Chowdhury *et al.*, "Daytime gas flare detection using Landsat-8 multispectral data," in *Geoscience & Remote Sensing Symposium*, 2014, pp. 258-261: IEEE.

[142] O. Anejionu *et al.*, "Detecting gas flares and estimating flaring volumes at individual flow stations using MODIS data," *Remote Sensing of Environment,* vol. 158, pp. 81-94, 2015.

[143] C. D. Elvidge *et al.*, "Methods for Global Survey of Natural Gas Flaring from Visible Infrared Imaging Radiometer Suite Data," *Energies,* vol. 9, no. 1, pp. 1-15, 2015.

[144] C. D. Elvidge *et al.*, "VIIRS nightfire: Satellite pyrometry at night," *Remote Sensensing,* vol. 5, no. 9, pp. 4423-4449, 2013.

[145] W. An *et al.*, "An Improved Iterative Censoring Scheme for CFAR Ship Detection With SAR Imagery," *IEEE Transactions on Geoscience Remote Sensing,* vol. 52, no. 8, pp. 4585-4595, 2014.

[146] L. Cheng *et al.*, "Invariant triangle-based stationary oil platform detection from multitemporal synthetic aperture radar data," *Journal of Applied Remote Sensing,* vol. 7, no. 1, pp. 302-309, 2013.

[147] J. Zhang *et al.*, "Automatic Extraction of Offshore Platforms in Single SAR Images Based on a Dual-Step-Modified Model," *Sensors,* vol. 19, no. 2, p. 231, 2019.

[148] Y. Liu *et al.*, "Geometric accuracy of remote sensing images over oceans: The use of global offshore platforms," *Remote Sensing of Environment,* vol. 222, pp. 244-266, 2019.

[149] S. J. Taylor and B. Letham, "Forecasting at scale," *The American Statistician,* vol. 72, no. 1, pp. 37-45, 2018.

[150] N. Zhao *et al.*, "Day-of-week and seasonal patterns of PM 2.5 concentrations over the United States: Time-series analyses using the Prophet procedure," *Atmospheric environment,* vol. 192, pp. 116-127, 2018.

[151] A. Ibrahim *et al.*, "Predicting market movement direction for bitcoin: A comparison of time series modeling methods," *Computers Electrical Engineering,* vol. 89, pp. 106905, 2021.

[152] B. Yang *et al.*, "Learning a deep similarity network for hyperspectral image classification," *IEEE Journal of Selected Topics in Applied Earth Observations Remote Sensing,* vol. 14, pp. 1482-1496, 2020.

[153] J. M. Joyce, "Kullback-Leibler divergence," in *International Encyclopedia of Statistical Science*, M. Lovric, Ed. Berlin, Heidelberg: Springer Berlin Heidelberg, 2011, pp. 720-722.

[154] R. O. Green *et al.*, "Imaging spectroscopy and the airborne visible/infrared imaging spectrometer (AVIRIS)," *Remote sensing of environment,* vol. 65, no. 3, pp. 227-248, 1998.

[155] K. K. Huang *et al.*, "Hyperspectral image classification via discriminative convolutional neural network with an improved triplet loss," *Pattern Recognition,* vol. 112, no. 2, p. 107744, 2021.

[156] R. Achanta *et al.*, "SLIC superpixels compared to state-of-the-art superpixel methods," *IEEE transactions on pattern analysis and machine intelligence,* vol. 34, no. 11, pp. 2274-2282, 2012.

[157] Y. Zhao and J. Yang, "Hyperspectral image denoising via sparse representation and low-rank constraint," *IEEE Transactions on Geoscience and Remote Sensing,* vol. 53, no. 1, pp. 296-308, 2014.

[158] S. Taylor and B. Letham, "prophet: Automatic forecasting procedure," *R package version 0.2,* vol. 1, 2017.

[159] AVIRIS image Indian Pines [Online]. Available: https://engineering.purdue.edu/~biehl/MultiSpec

[160] B. Du and L. Zhang, "A discriminative metric learning based anomaly detection method," *IEEE Transactions on Geoscience and Remote Sensing,* vol. 52, no. 11, pp. 6844-6857, 2014.

[161] AVIRIS image Salinas Valley [Online]. Available: http://www.ehu.eus/ccwintco/index.php?title=Hyperspectral_Remote_Sensing_Scenes

[162] ROSIS image Pavia University [Online]. Available: http://www.ehu.eus/ccwintco/index.php?title=Hyperspectral_Remote_Sensing_Scenes

[163] B. Demir and S. Erturk, "Empirical Mode Decomposition of Hyperspectral Images for Support Vector Machine Classification," *IEEE Transactions on Geoscience Remote Sensing,* vol. 48, no. 11, pp. 4071-4084, 2010.

[164] J. Wang *et al.*, "Semi-supervised classification by discriminative regularization," *Applied Soft Computing Journal,* vol. 58, pp. 245-255, 2017.

[165] X. J. Shen *et al.*, "Large-scale support vector machine classification with redundant data reduction," *Neurocomputing,* vol. 172, pp. 189-197, 2016.

[166] M. Pal and G. M. Foody, "Feature selection for classification of hyperspectral data by SVM," *IEEE Transactions on Geoscience and Remote Sensing,* vol. 48, no. 5, pp. 2297-2307, 2010.

[167] H. Xu *et al.*, "Superpixel-based spatial-spectral dimension reduction for hyperspectral imagery classification," *Neurocomputing,* vol. 360, pp. 138-150, 2019.

[168] G. H. Rosenfield and K. Fitzpatricklins, "A coefficient of agreement as a measure of thematic classification accuracy," *Photogrammetric Engineering Remote Sensing,* vol. 52, no. 2, pp. 223-227, 1986.

[169] S. Jia *et al.*, "Collaborative representation-based multiscale superpixel fusion for hyperspectral image classification," *IEEE Transactions on Geoscience and Remote Sensing,* vol. 57, no. 10, pp. 7770-7784, 2019.

[170] H. Wei *et al.*, "Deep Convolutional Neural Networks for Hyperspectral Image Classification," *Journal of Sensors,* vol. 2015, pp. 1-12, 2015.

[171] L. Wei *et al.*, "Hyperspectral Image Classification Using Deep Pixel-Pair Features," *IEEE Transactions on Geoscience Remote Sensing,* vol. 55, no. 2, pp. 1-10, 2016.

[172] N. Golyandina and A. Zhigljavsky, *Singular Spectrum Analysis for time series*. Springer Science & Business Media, 2013.

[173] V. Florinsky Igor, *Digital Terrain Analysis in soil science and geology*. Amsterdam: ACADEMIC PRESS/Elsevier, 2016.

[174] B. Rasti *et al.*, "Noise reduction in hyperspectral imagery: Overview and application," *Remote Sensing,* vol. 10, no. 3, p. 482, 2018.

[175] F. Zhang *et al.*, "Hyperspectral image denoising based on low-rank coefficients and orthonormal dictionary," *Signal Processing,* vol. 177, p. 107738, 2020.

[176] J. W. van Groenigen, "The influence of variogram parameters on optimal sampling schemes for mapping by kriging," (in English), *Geoderma,* vol. 97, no. 3-4, pp. 223-236, Sep 2000.

[177] A. Ajay *et al.*, "Aerial image classification using GURLS and LIBSVM," in *2016 International Conference on Communication and Signal Processing (ICCSP)*, 2016, pp. 0396-0401: IEEE.

[178] M. Wong *et al.*, "A Massive Self-Organizing Map For Hyperspectral Image Classification," in *2019 10th Workshop on Hyperspectral Imaging and Signal Processing: Evolution in Remote Sensing (WHISPERS)*, 2019, pp. 1-5: IEEE.

[179] UKHO. (2013). *Scottish Zone (200M Limit) - Exclusive Economic Zone (EEZ) adjacent to Scotland - Exclusive Economic Zone (EEZ) Order 2013*. Available: https://marine.gov.scot/maps/416

[180] EMODnet. (1979). *The Scotland coastline*. Available: https://www.emodnet-bathymetry.eu/media/emodnet_bathymetry/org/documents/emodnet_coastline_and_baseline_collection_2020-18dec2020.pdf

134

[181] OSPAR Commission. (2021). *OSPAR Inventory of Offshore Installations - 2019*. Available: https://odims.ospar.org/en/submissions/ospar_offshore_installations_2019_01/

[182] Oil and Gas Authority. (2021). *Offshore Oil and Gas Activity*. Available: https://ogauthority.maps.arcgis.com/apps/webappviewer/index.html?id=adbe5a796f5c41c68fc762ea137a682e

[183] ESA. (2017, 4th, January). *EO Browser*.

[184] Marine Scotland. (2015). *Beatrice Offshore Wind Farm Consent Plan*. Available: https://marine.gov.scot/sites/default/files/00510248.pdf

[185] Marine Scotland. (2018). *Development Layout and Specification Plan for Moray East Offshore Wind Farm*. Available: https://marine.gov.scot/sites/default/files/moray_east_dslp_version_2_final_aug_2018.pdf

[186] Marine Scotland. (2017). *The Design Statement for Aberdeen Offshore Wind Farm* Available: https://marine.gov.scot/sites/default/files/00518408_0.pdf

[187] Marine Scotland. (2017). *Hywind Scotland Pilot Park Project Plan for Construction Activities 2017*. Available: https://marine.gov.scot/sites/default/files/00516548_0.pdf

[188] Marine Scotland. (2014). *Kincardine Offshore Windfarm Environmental Scoping Assessment*. Available: http://marine.gov.scot/sites/default/files/00448819.pdf

[189] Zenodo. (2022). *The software and metadata used in Chapter 5.* Available: https://zenodo.org/record/6339911#.Ynzz4-jMJhE

[190] G. V. Weinberg, "General transformation approach for constant false alarm rate detector development," *Digital Signal Processing,* vol. 30, pp. 15-26, 2014.

[191] P. Ma *et al.*, "Multiscale 2D Singular Spectrum Analysis and Principal Component Analysis for Spatial-Spectral Noise-Robust Feature Extraction and Classification of Hyperspectral Images," *IEEE Journal of Selected Topics in Applied Earth Observations and Remote Sensing,* vol. 14, no. 99, pp. 1233-1245, 2020.

[192] N. Ostu *et al.*, "A thresholding selection method from gray level histogram," *IEEE SMC-8,* pp. 62-66, 1979.

[193] M. Huang *et al.*, "An Improved Image Segmentation Algorithm Based on the Otsu Method," presented at the 2012 13th ACIS International Conference on Software Engineering, Artificial Intelligence, Networking and Parallel/Distributed Computing, 2012.

[194] B. K. Khan *et al.*, "A Morphological Hessian Based Approach for Retinal Blood Vessels Segmentation and Denoising Using Region Based Otsu Thresholding," *Plos One,* vol. 11, no. 7, pp. e0158996, 2016.

[195] S. Pierre, "Morphological Image Analysis: Principles and Applications," *sensor review,* vol. 28, no. 5, pp. 800-801, 1999.

[196] H. Huang *et al.*, "Individual Tree Crown Detection and Delineation From Very-High-Resolution UAV Images Based on Bias Field and Marker-Controlled Watershed Segmentation Algorithms," *IEEE Journal of Selected Topics in Applied Earth Observations and Remote Sensing,* vol. 11, no. 7, pp. 2253-2262, 2018.

[197] B. Han, "Watershed Segmentation Algorithm Based on Morphological Gradient Reconstruction," presented at the In 2015 2nd International Conference on Information Science and Control Engineering In 2015 2nd International Conference on Information Science and Control Engineering, 2015.

[198] T. Lei *et al.*, "A conditionally invariant mathematical morphological framework for color images," *Information Sciences,* vol. 387, pp. 34-52, 2017.

[199] M. Baisantry *et al.*, "Two-Level Band Selection Framework for Hyperspectral Image Classification," *Journal of the Indian Society of Remote Sensing,* vol. 49, no. 4, pp. 843-856, 2021.

[200] L. Mou *et al.*, "Deep Reinforcement Learning for Band Selection in Hyperspectral Image Classification," *IEEE Transactions on Geoscience Remote Sensing,* vol. 60, pp. 1-14, 2021.

[201] L. Deng *et al.*, "M2H-Net: A Reconstruction Method For Hyperspectral Remotely Sensed Imagery," *ISPRS Journal of Photogrammetry Remote Sensing,* vol. 173, no. 2, pp. 323-348, 2021.

[202] A. Chakrabarty *et al.*, "Hyperspectral image classification incorporating bacterial foraging-optimized spectral weighting," *Artificial Intelligence Research,* vol. 1, no. 1, pp. 63-83, 2012.

[203] F. Xie *et al.*, "A novel spectral–spatial classification method for hyperspectral image at superpixel Level," vol. 10, no. 2, p. 463, 2020.

[204] S. Holzwarth *et al.*, "HySens-DAIS 7915/ROSIS imaging spectrometers at DLR," in *Proceedings of the 3rd EARSeL Workshop on Imaging Spectroscopy*, 2003, pp. 3-14.

Appendix 1: Introducing to the HSI datasets used

A.1.1 Indian Pines

The Indian Pines dataset [159], also namely 92AV3C, is acquired by the Airborne Visible/Infrared Imaging Spectrometer (AVIRIS) sensor over the Indian Pines study site in Northwest Indiana, USA, in 1992 [154]. This dataset has 145×145 pixels with a spatial resolution of 18 m/pixel [202]. Each pixel contains 224 spectral bands covering the wavelengths from 0.4-2.5um. The whole scene contains two-thirds agriculture, and one-third forest or other natural perennial vegetation. The spectral bands used in most image analysis methods are usually discarding 20 water absorption bands (104-108, 150-163 and 220) [203]. The ground truth is designated into 16 types of land-cover classes. One random band image (band 168) and the corresponding ground truth map are presented in Fig. A.1.1.

■ 1. Alfalfa (54) ■ 2. Corn-notill (1434)
■ 3. Corn-min (834) ■ 4. Corn (234)
■ 5. Grass/Pasture (497) ■ 6. Grass/Trees (747)
■ 7. Grass/Pasture-mowed (26) ■ 8. Hay-windrowed (489)
■ 9. Oats (20) ■ 10. Soybeans-notill (968)
■ 11. Soybean-min (2468) ■ 12. Soybean-clean (614)
■ 13. Wheat (212) ■ 14. Woods (1294)
■ 15. Building-Grass-Trees-Drives (380) ■ 16. Stone-steel Towers (95)
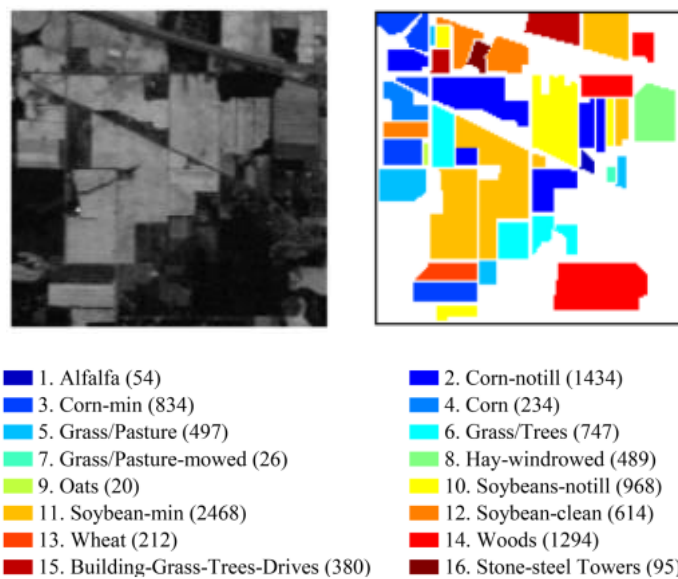
Fig. A.1.1. Band 168 of Indian Pines dataset (left) and the corresponding ground truth map (right) with the number of samples in parentheses.

A.1.2 Salinas Valley

The second dataset is Salinas Valley [161], which was acquired via AVIRIS at the Salinas Valley in California, USA, in 1988. It has 512×217 pixels and 224 spectral bands with a high spatial resolution of 3.7m/pixel [202]. Similar to the Indian Pines dataset, twenty water absorption bands, [108-112], [154-167], 224, are discarded for the corrected data. The whole scene contains vegetables, bare soils, and vineyard fields. Ground truth map is designed including 16 classes. A random band (band 50) and the corresponding ground truth map are shown in Fig. A.1.2.

1. Broccoli green weeds 1 (2009)	2. Broccoli green weeds 2 (3726)
3. Fallow (1976)	4. Fallow rough plow (1394)
5. Fallow smooth (2678)	6. Stubble (3959)
7. Celery (3579)	8. Grapes untrained (11271)
9. Soil vineyard develop (6203)	10. Corn senesced green weeds (3278)
11. Lettuce romaine 4wk (1068)	12. Lettuce romaine 5wk (1927)
13. Lettuce romaine 6wk (916)	14. Lettuce romaine 7wk (1070)
15. Vineyard untrained (7268)	16. Vineyard vertical trellis (1807)

Fig. A.1.2. Band 50 of Salinas Valley dataset (left) and the corresponding ground truth map (right) with the number of samples in parentheses.

138

A.1.3 Pavia University

The Pavia University dataset [162] was gathered by the Reflective Optics System Imaging Spectrometer (ROSIS) sensor over Pavia, Northern Italy in 2001 [204]. This scene consists of 610×340 pixels with a spatial resolution of 1.3m/pixel. Each pixel includes 115 spectral bands in a spectral range of 0.43-0.86um. For avoiding the effect of water absorption, this scene can be corrected by reducing the available number of bands to 103. A random band (band 70) and the corresponding ground truth map with nine dominant classes including urban, soil and vegetation are shown in Fig. A.1.3.

1. Asphalt (6631)	2. Meadows (18649)	3. Gravel (2099)
4. Trees (3064)	5. Painted metal sheets (1345)	6. Bare soil (5029)
7. Bitumen (1330)	8. Self-blocking bricks (3682)	9. Shadows (947)
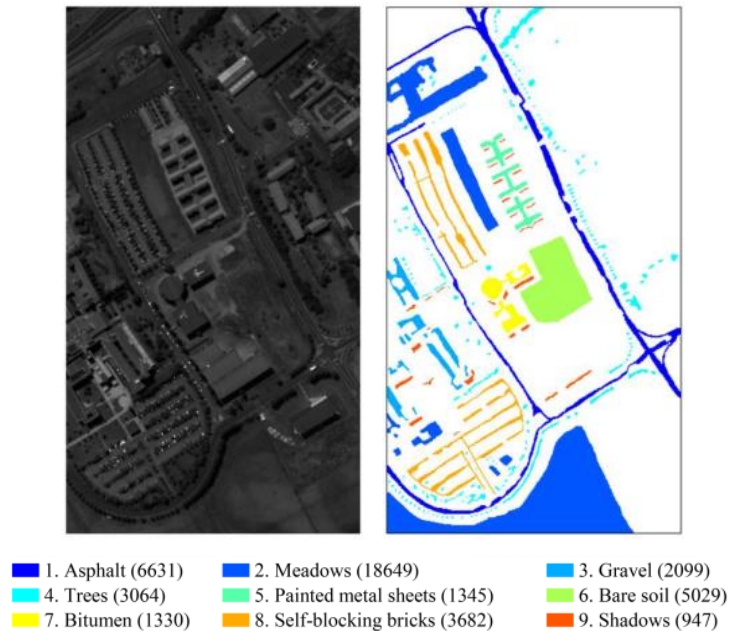
Fig. A.1.3. Band 70 of Pavia University dataset (left) and the corresponding ground truth map (right) with the number of samples in parentheses.

Appendix 2: Additional information of the ground truth ocean infrastructure and the detected results

This appendix contains further information in terms of the ground truth for the ocean infrastructure and the detected results in connection to the work in Chapter 5.

A.2.1 The constructed ground truth

Table A.2.1. The constructed ground truth dataset of oil/gas platforms and semi-permanent objects.

ID	Name	Latitude (°)	Longitude (°)	Topside area (Square meters)
1	Dunbar	60.6286	1.6510	5394
2	Magnus	61.6198	1.3050	7565
3	Western Isles FPSO	61.2140	0.7540	5544
4	Tern	61.2751	0.9180	5208
5	Heather Alpha	60.9530	0.9380	4290
6	Cormorant Alpha	61.1020	1.0710	5656
7	North Cormorant	61.2400	1.1480	5915
8	Eider	61.3565	1.1600	3818
9	Ninian north *	60.9054	1.4195	—
10	Ninian South	60.8050	1.4490	7209
11	Northern Producer *	61.4870	1.4630	—
12	Ninian Central	60.8560	1.4680	5888
13	Thistle Alpha	61.3620	1.5780	6460
14	Dunlin Alpha	61.2742	1.5958	6840
15	Brent Bravo *	61.0550	1.7110	—
16	Brent Charlie	61.0959	1.7200	6172
17	Alwyn North Bravo	60.8096	1.7340	3551
18	Alwyn North Alpha	60.8086	1.7360	3927
19	Brent Delta *	61.1320	1.7341	—
20	Noble Lloyd Noble	59.5891	1.0550	4494
21	Mariner production, drilling and living quarters (PDQ)	59.5880	1.0550	9912

22	Mariner FSU	59.6085	1.0760	10130
23	Kraken FPSO	59.9258	1.2930	12502
24	Beryl Bravo	59.6099	1.5110	4689
25	Harding	59.2790	1.5140	5304
26	Beryl Alpha	59.5446	1.5340	1020
27	Beryl Flare	59.5460	1.5330	378
28	Beryl Alpha Riser	59.5450	1.5360	4352
29	Beryl SPM-3	59.5338	1.5575	864
30	Beryl SPM-2	59.5535	1.5610	2179
31	Gryphon Alpha FPSO	59.3600	1.5690	12288
32	Bruce PUQ	59.7421	1.6710	4698
33	Bruce Compression Reception (CR)	59.7438	1.6710	706
34	Bruce Drilling	59.7430	1.6700	4212
35	Tartan Alpha	58.3692	0.0720	4823
36	Scott Drilling and Process (DP)	58.2887	0.2006	2964
37	Scott Utilities and Quarters	58.2883	0.1990	3680
38	Piper Bravo	58.4607	0.2494	6090
39	Saltire	58.4163	0.3331	4785
40	Global Producer III FPSO	58.3529	0.8630	8660
41	Alba FPSO	58.0478	1.0329	9315
42	Alba North	58.0580	1.0800	5520
43	Balmoral FPSO	58.2287	1.1071	5010
44	Britannia	58.0480	1.1372	6032
45	Britannia Bridge-Linked Platform (BLP)	58.0481	1.1400	2279
46	Hummingbird FPSO	57.9760	1.2380	4154
47	Tiffany	58.4777	1.2649	5358
48	Brae Alpha	58.6920	1.2803	5544
49	Brae Bravo	58.7916	1.3458	4140
50	Andrew	58.0469	1.4027	5246
51	Brae East	58.8755	1.5254	4560
52	Glen Lyon FPSO	60.3560	-4.0680	13152
53	Solan	60.0618	-3.9710	4296

54	Aoka Mizu FPSO	60.1800	-3.8700	11662
55	Clair	60.6920	-2.5440	6627
56	Clair Ridge DP	60.7361	-2.4940	5972
57	Clair Ridge quarters and utilities (QU)	60.7360	-2.4970	5151
58	Foinaven FPSO	60.3150	-4.2760	11397
59	Claymore Production	58.4490	-0.2565	4740
60	Claymore Accommodation	58.4489	-0.2556	4484
61	Captain BLP	58.3060	-1.7714	2236
62	Captain wellhead protection platform	58.3070	-1.7700	4350
63	Captain FPSO	58.3052	-1.7436	10731
64	Ross FPSO	58.1015	-1.4400	9844
65	Well Head	57.8140	-0.9740	2583
66	Production Jacket	57.8138	-0.9760	4128
67	Quarters Utilities (QU) Jacket	57.8130	-0.9780	4181
68	Oil Stripper platform	57.8144	-0.9762	2107
69	Golden Eagle Wellhead	57.9610	-0.9180	3549
70	Golden Eagle PUQ	57.9600	-0.9180	4788
71	Kittiwake	57.4678	0.5102	4032
72	Catcher FPSO	56.7700	0.7130	11050
73	Forties Unity	57.7210	0.7548	1539
74	Anasuria FPSO	57.2565	0.8081	9072
75	Forties Charlie	57.7260	0.8460	5760
76	Triton FPSO	57.0831	0.8910	9460
77	Forties Delta	57.7219	0.9010	4686
78	Forties Bravo	57.7485	0.9134	4180
79	Forties Alpha	57.7310	0.9710	5616
80	Fasp	57.7310	0.9689	3036
81	Gannet Alpha	57.1843	0.9984	6544
82	Forties Echo	57.7157	1.0310	1987
83	Nelson	57.6627	1.1446	6467
84	Arbroath	57.3743	1.3816	2201
85	Montrose BLP	57.4510	1.3870	2916

86	Montrose Alpha	57.4501	1.3870	4104
87	Etap processing, drilling and riser (PDR)	57.2941	1.6620	3776
88	Etap QU	57.2937	1.6610	4108
89	North Everest	57.7580	1.8000	4418
90	Cats Riser	57.7575	1.8020	2100
91	West Franklin wellhead platform (WHP)	56.9592	1.8060	2050
92	Elgin A WHP	57.0116	1.8383	1450
93	Elgin B WHP	57.0112	1.8402	5976
94	Elgin PUQ	57.0110	1.8362	5751
95	Franklin WHP	56.9660	1.8680	6520
96	Culzean Utilities and Living Quarters	57.1902	1.9079	3610
97	Culzean Central Processing Facility	57.1910	1.9100	4277
98	Culzean WHP	57.1921	1.9110	7701
99	Shearwater A	57.0315	1.9538	5016
100	Shearwater C	57.0303	1.9534	4576
101	Erskine	57.0390	2.0700	2028
102	FPF1 FPSO	56.7810	2.1090	6525
103	Mungo	57.3747	1.9965	1672
104	Lomond	57.2869	2.1767	4165
105	Jasmine Wellhead	56.7242	2.2060	7112
106	Jasmine Living Quarters	56.7235	2.2040	2180
107	Jade	56.8490	2.2540	2108
108	Haewene Brim FPSO	57.1609	2.2930	9476
109	Judy Riser and Separation Platform	56.6980	2.3350	4176
110	Judy	56.6968	2.3369	5775
111	Culzean FSO - Ailsa	57.1955	1.9610	9360
112	Armada	57.9567	1.8444	4989
113	Jacky platform	58.1838	-2.9801	4964
114	Beatrice Charlie *	58.0940	-3.1532	—
115	Betrice Alpha Drilling *	58.1148	-3.0880	—
116	Beatrice Alpha Production *	58.1140	-3.0890	—
117	Beatrice Bravo *	58.1473	-3.0216	—

118	Manifold and Compression Platform 01 (MCP01) *	58.8265	-0.2880	—
119	Frigg Treatment platform 1 (TP1) *	59.8790	2.0630	—
120	Frigg Concrete drilling platform 1 (CDP1) *	59.8748	2.0607	—
121	Frigg Treatment Compression Platform 2 (TCP 2) *	59.8791	2.0650	—

* The infrastructure has undergone decommissioning.

Table A.2.2. The constructed ground truth dataset of wind turbines in Beatrice Wind Farm.

ID	Name	Latitude (°)	Longitude (°)	Diameter Length (Meters)
1	BE-A5	58.2079	-2.9999	154
2	BE-B5	58.2115	-2.9812	154
3	BE-B6	58.2218	-2.9777	154
4	BE-B7	58.2322	-2.9743	154
5	BE-C4	58.2051	-2.9656	154
6	BE-C5	58.2150	-2.9625	154
7	BE-C6	58.2254	-2.9590	154
8	BE-C7	58.2357	-2.9555	154
9	BE-C8	58.2461	-2.9521	154
10	BE-C9	58.2564	-2.9486	154
11	BE-D3	58.1999	-2.9500	154
12	BE-D4	58.2083	-2.9472	154
13	BE-D5	58.2186	-2.9438	154
14	BE-D6	58.2289	-2.9403	154
15	BE-D7	58.2393	-2.9368	154
16	BE-D8	58.2497	-2.9333	154
17	BE-D9	58.2600	-2.9298	154
18	BE-D10	58.2704	-2.9264	154
19	BE-D11	58.2807	-2.9229	154
20	BE-E1	58.1817	-2.9375	154

21	BE-E2	58.1912	-2.9355	154
22	BE-E3	58.2015	-2.9320	154
23	BE-E4	58.2119	-2.9285	154
24	BE-E5	58.2222	-2.9250	154
25	BE-E6	58.2326	-2.9216	154
26	BE-E7	58.2429	-2.9181	154
27	BE-E8	58.2533	-2.9146	154
28	BE-E9	58.2636	-2.9111	154
29	BE-E10	58.2739	-2.9076	154
30	BE-E11	58.2843	-2.9041	154
31	BE-E12	58.2947	-2.9006	154
32	BE-F2	58.1948	-2.9168	154
33	BE-F3	58.2051	-2.9133	154
34	BE-F4	58.2155	-2.9098	154
35	BE-F5	58.2258	-2.9063	154
36	BE-F6	58.2361	-2.9028	154
37	BE-F9	58.2672	-2.8923	154
38	BE-F10	58.2776	-2.8888	154
39	BE-F11	58.2879	-2.8853	154
40	BE-F12	58.2982	-2.8819	154
41	BE-F13	58.3086	-2.8784	154
42	BE-G3	58.2091	-2.8954	154
43	BE-G4	58.2190	-2.8911	154
44	BE-G5	58.2293	-2.8876	154
45	BE-G6	58.2397	-2.8841	154
46	BE-G8	58.2604	-2.8771	154
47	BE-G9	58.2708	-2.8736	154
48	BE-G10	58.2811	-2.8701	154
49	BE-G11	58.2915	-2.8666	154
50	BE-G12	58.3018	-2.8631	154
51	BE-G13	58.3122	-2.8596	154
52	BE-G14	58.3225	-2.8560	154

53	BE-H4	58.2226	-2.8723	154
54	BE-H5	58.2329	-2.8688	154
55	BE-H6	58.2433	-2.8653	154
56	BE-H7	58.2537	-2.8618	154
57	BE-H8	58.2640	-2.8583	154
58	BE-H9	58.2744	-2.8548	154
59	BE-H10	58.2847	-2.8513	154
60	BE-H11	58.2951	-2.8478	154
61	BE-H12	58.3054	-2.8443	154
62	BE-H13	58.3157	-2.8408	154
63	BE-J5	58.2365	-2.8501	154
64	BE-J6	58.2469	-2.8466	154
65	BE-J7	58.2572	-2.8431	154
66	BE-J8	58.2676	-2.8396	154
67	BE-J9	58.2779	-2.8361	154
68	BE-J10	58.2883	-2.8325	154
69	BE-J11	58.2986	-2.8290	154
70	BE-J12	58.3089	-2.8255	154
71	BE-J13	58.3193	-2.8219	154
72	BE-K6	58.2505	-2.8278	154
73	BE-K7	58.2608	-2.8243	154
74	BE-K8	58.2712	-2.8208	154
75	BE-K9	58.2815	-2.8173	154
76	BE-K10	58.2918	-2.8138	154
77	BE-K11	58.3022	-2.8102	154
78	BE-K12	58.3125	-2.8067	154
79	BE-L7	58.2644	-2.8056	154
80	BE-L8	58.2747	-2.8020	154
81	BE-L9	58.2851	-2.7985	154
82	BE-L10	58.2954	-2.7949	154
83	BE-M9	58.2886	-2.7797	154
84	BE-M10	58.2989	-2.7762	154

85	Wind turbine A	58.0999	-3.0827	154
86	Wind turbine B	58.0955	-3.0739	154
87	BE-F8*	58.2567	-2.8956	—
88	BE-G7*	58.2497	-2.8803	—

* Offshore transformer modules (OTMs)

Table A.2.3. The constructed ground truth dataset of wind turbines in Moray East Wind Farm.

ID	Name	Latitude (°)	Longitude (°)	Diameter Length (Meters)
1	ME-A01	58.0758	-2.8691	164
2	ME-A02	58.0859	-2.8691	164
3	ME-B02	58.0858	-2.8428	164
4	ME-B03	58.0959	-2.8428	164
5	ME-B04	58.1061	-2.8427	164
6	ME-B05	58.1161	-2.8424	164
7	ME-B13	58.1973	-2.8423	164
8	ME-B14	58.2074	-2.8423	164
9	ME-C02	58.0855	-2.8166	164
10	ME-C04	58.1059	-2.8165	164
11	ME-C05	58.1160	-2.8164	164
12	ME-C07	58.1363	-2.8163	164
13	ME-C08	58.1464	-2.8163	164
14	ME-C09	58.1566	-2.8162	164
15	ME-C10	58.1667	-2.8162	164
16	ME-C11	58.1768	-2.8162	164
17	ME-C12	58.1869	-2.8161	164
18	ME-C13	58.1971	-2.8161	164
19	ME-C14	58.2073	-2.8159	164
20	ME-C15	58.2174	-2.8159	164
21	ME-C16	58.2275	-2.8159	164
22	ME-D04	58.1057	-2.7902	164
23	ME-D05	58.1158	-2.7902	164
24	ME-D06	58.1258	-2.7901	164

25	ME-D07	58.1361	-2.7901	164
26	ME-D08	58.1462	-2.7899	164
27	ME-D09	58.1564	-2.7899	164
28	ME-D10	58.1665	-2.7899	164
29	ME-D11	58.1766	-2.7898	164
30	ME-D12	58.1868	-2.7897	164
31	ME-D13	58.1969	-2.7898	164
32	ME-D14	58.2071	-2.7896	164
33	ME-D15	58.2171	-2.7896	164
34	ME-D16	58.2273	-2.7895	164
35	ME-D17	58.2375	-2.7895	164
36	ME-E04	58.1055	-2.7639	164
37	ME-E05	58.1156	-2.7639	164
38	ME-E14	58.2069	-2.7633	164
39	ME-E18	58.2474	-2.7630	164
40	ME-E19	58.2575	-2.7629	164
41	ME-F04	58.1053	-2.7377	164
42	ME-F08	58.1458	-2.7374	164
43	ME-F21	58.2776	-2.7365	164
44	ME-G05	58.1152	-2.7114	164
45	ME-G06	58.1254	-2.7113	164
46	ME-G07	58.1355	-2.7112	164
47	ME-G08	58.1456	-2.7111	164
48	ME-G09	58.1558	-2.7111	164
49	ME-G10	58.1659	-2.7109	164
50	ME-G11	58.1760	-2.7109	164
51	ME-G13	58.1963	-2.7107	164
52	ME-G15	58.2166	-2.7106	164
53	ME-G16	58.2267	-2.7105	164
54	ME-G17	58.2369	-2.7104	164
55	ME-G18	58.2469	-2.7103	164
56	ME-G19	58.2571	-2.7102	164

57	ME-G20	58.2673	-2.7102	164
58	ME-G21	58.2774	-2.7101	164
59	ME-G22	58.2875	-2.7099	164
60	ME-H05	58.1150	-2.6851	164
61	ME-H06	58.1251	-2.6850	164
62	ME-H07	58.1352	-2.6849	164
63	ME-H08	58.1454	-2.6849	164
64	ME-H09	58.1556	-2.6848	164
65	ME-H10	58.1657	-2.6847	164
66	ME-H11	58.1758	-2.6846	164
67	ME-H13	58.1961	-2.6844	164
68	ME-H14	58.2062	-2.6843	164
69	ME-H16	58.2265	-2.6841	164
70	ME-H17	58.2366	-2.6840	164
71	ME-H18	58.2468	-2.6839	164
72	ME-H19	58.2569	-2.6839	164
73	ME-H20	58.2671	-2.6838	164
74	ME-H21	58.2772	-2.6837	164
75	ME-H22	58.2873	-2.6836	164
76	ME-I06	58.1249	-2.6588	164
77	ME-I07	58.1351	-2.6587	164
78	ME-I18	58.2466	-2.6576	164
79	ME-I19	58.2567	-2.6575	164
80	ME-I20	58.2668	-2.6574	164
81	ME-J07	58.1348	-2.6324	164
82	ME-J08	58.1449	-2.6323	164
83	ME-J09	58.1551	-2.6322	164
84	ME-J10	58.1652	-2.6321	164
85	ME-J12	58.1855	-2.6319	164
86	ME-J13	58.1957	-2.6318	164
87	ME-J14	58.20583	-2.6317	164
88	ME-J16	58.2261	-2.6314	164

149

89	ME-J17	58.2362	-2.6313	164
90	ME-J18	58.2463	-2.6312	164
91	ME-J19	58.2564	-2.6315	164
92	ME-K09	58.1549	-2.6059	164
93	ME-K10	58.1650	-2.6058	164
94	ME-K11	58.1752	-2.6057	164
95	ME-K16	58.2258	-2.6051	164
96	ME-K17	58.2365	-2.6022	164
97	ME-L09	58.1546	-2.5796	164
98	ME-L11	58.1749	-2.5794	164
99	ME-L12	58.1851	-2.5792	164
100	ME-L13	58.1952	-2.5791	164
101	OSP1*	58.1257	-2.7641	—
102	OSP2*	58.2167	-2.7371	—
103	OSP3*	58.1654	-2.6585	—

* Offshore Substation Platform (OSP)

Table A.2.4. The constructed ground truth dataset of wind turbines in HyWind Wind Farm (Aberdeenshire).

ID	Name	Latitude (°)	Longitude (°)	Diameter Length (Meters)
1	HS1	57.4843	-1.3323	154
2	HS2	57.4908	-1.3520	154
3	HS3	57.4972	-1.3718	154
4	HS4	57.4783	-1.3526	154
5	HS5	57.4848	-1.3723	154

Table A.2.5. The constructed ground truth dataset of wind turbines in Kincardine Wind Farm (Aberdeenshire).

ID	Name	Latitude (°)	Longitude (°)	Diameter Length (Meters)
1	KIN-01	57.0053	-1.8812	164
2	KIN-02	56.9973	-1.8738	164
3	KIN-03	56.9892	-1.8665	164
4	KIN-04	57.0186	-1.8550	164
5	KIN-05	57.0105	-1.8477	164

Table A.2.6. The constructed ground truth dataset of wind turbines in Aberdeen Offshore Wind Farm.

ID	Name	Latitude (˚)	Longitude (˚)	Diameter Length (Meters)
1	AWF01	57.2237	-2.0126	150
2	AWF02	57.2284	-2.0022	150
3	AWF03	57.2335	-1.9895	150
4	AWF04	57.2401	-1.9758	150
5	AWF05	57.2158	-2.0112	150
6	AWF06	57.2201	-2.0002	150
7	AWF07	57.2244	-1.9879	150
8	AWF08	57.2301	-1.9742	150
9	AWF09	57.2079	-2.0104	150
10	AWF10	57.2117	-1.9987	150
11	AWF11	57.2160	-1.9858	150

A.2.2 The geolocating results

Table A.2.7. The detected contour range results of oil/gas platforms and semi-permanent objects in Scottish waters.

ID	Name	Contour range	
		Latitude (˚)	Longitude (˚)
1	Dunbar	60.628517 ~ 60.629055	1.649901 ~ 1.651715
2	Magnus	61.619080 ~ 61.619962	1.304405 ~ 1.306393
3	Western Isles FPSO	61.213852 ~ 61.214820	0.753038 ~ 0.754490
4	Tern	61.274986 ~ 61.275689	0.917036 ~ 0.918669
5	Heather Alpha	60.952831 ~ 60.953364	0.937178 ~ 0.938630
6	Cormorant Alpha	61.101560 ~ 61.102532	1.070591 ~ 1.072043
7	North Cormorant	61.239452 ~ 61.240244	1.147276 ~ 1.148546
8	Eider	61.356320 ~ 61.356846	1.159268 ~ 1.160539
9	Ninian north	60.905220 ~ 60.905576	1.419303 ~ 1.419848
10	Ninian South	60.804512 ~ 60.805404	1.447774 ~ 1.449770
11	Northern Producer	61.486624 ~ 61.487322	1.461770 ~ 1.463403

12	Ninian Central	60.855808 ~ 60.856432	1.466477 ~ 1.468473
13	Thistle Alpha	61.361894 ~ 61.362771	1.577503 ~ 1.578954
14	Dunlin Alpha	61.273705 ~ 61.274584	1.595310 ~ 1.596762
15	Brent Bravo	61.054543 ~ 61.056136	1.710742 ~ 1.712193
16	Brent Charlie	61.095037 ~ 61.095921	1.719479 ~ 1.721112
17	Alwyn North Bravo	60.809090 ~ 60.809723	1.733229 ~ 1.734314
18	Alwyn North Alpha	60.808365 ~ 60.808818	1.735217 ~ 1.736482
19	Brent Delta	61.131771 ~ 61.132125	1.734055 ~ 1.734418
20	Noble Lloyd Noble	59.589025 ~ 59.589847	1.053823 ~ 1.055274
21	Mariner PDQ	59.587837 ~ 59.588751	1.053097 ~ 1.056000
22	Mariner FSU	59.607397 ~ 59.608524	1.073946 ~ 1.077199
23	Kraken FPSO	59.924172 ~ 59.925939	1.291559 ~ 1.293367
24	Beryl Bravo	59.609422 ~ 59.609977	1.510435 ~ 1.511705
25	Harding	59.278428 ~ 59.279268	1.513581 ~ 1.515214
26	Beryl Alpha	59.544489 ~ 59.544677	1.533876 ~ 1.534418
27	Beryl Flare*	—	—
28	Beryl Alpha Riser	59.544677 ~ 59.545336	1.535502 ~ 1.536948
29	Beryl SPM-3	59.533681 ~ 59.533867	1.557417 ~ 1.557780
30	Beryl SPM-2	59.553452 ~ 59.553822	1.560377 ~ 1.561465
31	Gryphon Alpha FPSO	59.359063 ~ 59.361206	1.568349 ~ 1.570707
32	Bruce PUQ	59.742005 ~ 59.742557	1.670322 ~ 1.671955
33	Bruce CR *	—	—
34	Bruce Drilling	59.742834 ~ 59.743202	1.669960 ~ 1.670686
35	Tartan Alpha	58.368864 ~ 58.369439	0.071343 ~ 0.072976
36	Scott DP	58.288221 ~ 58.288904	0.199949 ~ 0.200853
37	Scott Utilities and Quarters	58.287928 ~ 58.288513	0.198323 ~ 0.199408
38	Piper Bravo	58.460123 ~ 58.461079	0.248381 ~ 0.250377
39	Saltire	58.415647 ~ 58.416509	0.331739 ~ 0.333191
40	Global Producer III FPSO	58.352599 ~ 58.352989	0.860096 ~ 0.863891
41	Alba FPSO	58.047390 ~ 58.047874	1.031359 ~ 1.032992
42	Alba North	58.057568 ~ 58.058342	1.078810 ~ 1.080625
43	Balmoral FPSO	58.228229 ~ 58.228893	1.106116 ~ 1.107925

44	Britannia	58.047547 ~ 58.048235	1.135946 ~ 1.138115
45	Britannia BLP	58.047842 ~ 58.048235	1.139018 ~ 1.140103
46	Hummingbird FPSO	57.975876 ~ 57.976555	1.237036 ~ 1.238125
47	Tiffany	58.477197 ~ 58.478057	1.263989 ~ 1.265804
48	Brae Alpha	58.691522 ~ 58.692282	1.279512 ~ 1.281145
49	Brae Bravo	58.791158 ~ 58.791916	1.345040 ~ 1.346492
50	Andrew	58.046424 ~ 58.047198	1.401684 ~ 1.403498
51	Brae East	58.874968 ~ 58.875724	1.524741 ~ 1.526011
52	Glen Lyon FPSO	60.354990 ~ 60.356618	-4.068720 ~ -4.064214
53	Solan	60.061161 ~ 60.061891	-3.971589 ~ -3.970327
54	Aoka Mizu FPSO	60.179083 ~ 60.180174	-3.870801 ~ -3.866655
55	Clair	60.691568 ~ 60.692121	-2.545760 ~ -2.543563
56	Clair Ridge DP	60.736072 ~ 60.736809	-2.495225 ~ -2.493211
57	Clair Ridge QU	60.735611 ~ 60.736072	-2.498155 ~ -2.496141
58	Foinaven FPSO	60.314613 ~ 60.316062	-4.276289 ~ -4.272143
59	Claymore Production	58.448721 ~ 58.449486	-0.258089 ~ -0.256457
60	Claymore Accommodation	58.448147 ~ 58.448912	-0.255731 ~ -0.254099
61	Captain BLP	58.305752 ~ 58.306226	-1.771938 ~ -1.771031
62	Captain wellhead protection platform	58.306416 ~ 58.307175	-1.770669 ~ -1.769580
63	Captain FPSO	58.304506 ~ 58.305299	-1.747163 ~ -1.743501
64	Ross FPSO	58.100758 ~ 58.102698	-1.441461 ~ -1.439834
65	Well Head	57.813932 ~ 57.814427	-0.975030 ~ -0.973946
66	Production Jacket	57.813141 ~ 57.813834	-0.976657 ~ -0.975030
67	Quarters Utilities (QU) Jacket	57.812350 ~ 57.813043	-0.978644 ~ -0.976837
68	Oil Stripper platform	57.814229 ~ 57.814723	-0.976657 ~ -0.975753
69	Golden Eagle Wellhead	57.960820 ~ 57.961411	-0.918163 ~ -0.916899
70	Golden Eagle PUQ	57.959540 ~ 57.960328	-0.918705 ~ -0.917260
71	Kittiwake	57.467124 ~ 57.467834	0.510031 ~ 0.511130
72	Catcher FPSO	56.769782 ~ 56.770384	0.709836 ~ 0.713645
73	Forties Unity	57.720689 ~ 57.721177	0.754255 ~ 0.754981
74	Anasuria FPSO	57.256170 ~ 57.256665	0.804706 ~ 0.808153
75	Forties Charlie	57.725894 ~ 57.726577	0.845140 ~ 0.846591

76	Triton FPSO	57.082713 ~ 57.083310	0.887659 ~ 0.891287
77	Forties Delta	57.721330 ~ 57.722014	0.900881 ~ 0.902152
78	Forties Bravo	57.748255 ~ 57.748938	0.912827 ~ 0.914097
79	Forties Alpha	57.730904 ~ 57.731608	0.970453 ~ 0.971918
80	Fasp	57.730803 ~ 57.731407	0.968622 ~ 0.969538
81	Gannet Alpha	57.183816 ~ 57.185005	0.996785 ~ 0.999325
82	Forties Echo	57.715369 ~ 57.715759	1.030276 ~ 1.031002
83	Nelson	57.661688 ~ 57.662861	1.143109 ~ 1.145468
84	Arbroath	57.373967 ~ 57.374558	1.380932 ~ 1.382021
85	Montrose BLP	57.450681 ~ 57.451480	1.386506 ~ 1.387049
86	Montrose Alpha	57.449583 ~ 57.450381	1.386145 ~ 1.387410
87	Etap PDR	57.294031 ~ 57.294525	1.660861 ~ 1.662312
88	Etap QU	57.293142 ~ 57.293834	1.660135 ~ 1.661587
89	North Everest	57.757697 ~ 57.758184	1.799136 ~ 1.800951
90	Cats Riser	57.757209 ~ 57.757599	1.801132 ~ 1.802402
91	West Franklin WHP	56.959151 ~ 56.959563	1.805378 ~ 1.806296
92	Elgin A WHP*	—	—
93	Elgin B WHP*	—	—
94	Elgin PUQ	57.010471 ~ 57.011367	1.835573 ~ 1.837387
95	Franklin WHP	56.965817 ~ 56.966537	1.866625 ~ 1.869189
96	Culzean Utilities and Living Quarters	57.189832 ~ 57.190525	1.907131 ~ 1.908583
97	Culzean Central Processing Facility	57.190723 ~ 57.191516	1.908764 ~ 1.910215
98	Culzean WHP	57.192011 ~ 57.193200	1.909852 ~ 1.911848
99	Shearwater A	57.031179 ~ 57.032362	1.952427 ~ 1.954420
100	Shearwater C	57.029799 ~ 57.030785	1.952608 ~ 1.954057
101	Erskine	57.038847 ~ 57.039344	2.069724 ~ 2.070450
102	FPF1 FPSO	56.780219 ~ 56.781021	2.108290 ~ 2.109741
103	Mungo	57.374524 ~ 57.374931	1.996159 ~ 1.996892
104	Lomond	57.286520 ~ 57.287112	2.175829 ~ 2.177462
105	Jasmine Wellhead	56.724125 ~ 56.725228	2.204670 ~ 2.206666
106	Jasmine Living Quarters	56.723322 ~ 56.723723	2.203944 ~ 2.204852
107	Jade	56.848831 ~ 56.849330	2.253838 ~ 2.254746

108	Haewene Brim FPSO	57.160319 ~ 57.160914	2.292038 ~ 2.293671
109	Judy Riser and Separation Platform	56.697618 ~ 56.698120	2.334940 ~ 2.336210
110	Judy	56.696112 ~ 56.697116	2.336391 ~ 2.337843
111	Culzean FSO - Ailsa	57.195223 ~ 57.195619	1.959675 ~ 1.961490
112	Armada	57.956237 ~ 57.957207	1.843930 ~ 1.844837
113	Jacky platform	58.182816 ~ 58.183866	-2.980600 ~ -2.979338
114	Beatrice Charlie	58.093794 ~ 58.094180	-3.153639 ~ -3.152913
115	Betrice Alpha Drilling	58.114305 ~ 58.114884	-3.088377 ~ -3.086926
116	Beatrice Alpha Production	58.113725 ~ 58.114305	-3.089647 ~ -3.088559
117	Beatrice Bravo	58.147027 ~ 58.147419	-3.022115 ~ -3.021211
118	Manifold and Compression Platform 01 (MCP01)	58.826305 ~ 58.827157	-0.288824 ~ -0.287554
119	Frigg Treatment platform 1 (TP1)	59.878877 ~ 59.879333	2.062646 ~ 2.063191
120	Frigg Concrete drilling platform 1 (CDP1)	59.874407 ~ 59.874863	2.060096 ~ 2.060823
121	Frigg Treatment Compression Platform 2 (TCP 2)	59.879060 ~ 59.879607	2.064642 ~ 2.065550

* The infrastructure is omitted in Sentinel-2 data.

Table A.2.8. The detected contour range results in Beatrice Wind Farm.

ID	Name	Contour range	
		Latitude (˚)	Longitude (˚)
1	BE-A5	58.207460 ~ 58.208031	-3.000569 ~ -2.999290
2	BE-B5	58.211030 ~ 58.211885	-2.981578 ~ -2.980660
3	BE-B6	58.221224 ~ 58.222174	-2.978122 ~ -2.977020
4	BE-B7	58.231744 ~ 58.232314	-2.974534 ~ -2.973620
5	BE-C4	58.204843 ~ 58.205699	-2.965634 ~ -2.964900
6	BE-C5	58.214703 ~ 58.215273	-2.962874 ~ -2.961770
7	BE-C6	58.224819 ~ 58.225864	-2.959245 ~ -2.958510
8	BE-C7	58.235387 ~ 58.236169	-2.956113 ~ -2.955030
9	BE-C8	58.245478 ~ 58.246537	-2.952631 ~ -2.951360
10	BE-C9	58.256084 ~ 58.256758	-2.949109 ~ -2.947837

11	BE-D3	58.199796 ~ 58.200367	-2.950213 ~ -2.949110
12	BE-D4	58.207666 ~ 58.208522	-2.947727 ~ -2.946630
13	BE-D5	58.218326 ~ 58.218802	-2.944259 ~ -2.943160
14	BE-D6	58.228702 ~ 58.229178	-2.940825 ~ -2.939730
15	BE-D7	58.239113 ~ 58.239684	-2.937332 ~ -2.936230
16	BE-D8	58.249020 ~ 58.249876	-2.933631 ~ -2.932720
17	BE-D9	58.259423 ~ 58.260278	-2.930127 ~ -2.929210
18	BE-D10	58.269745 ~ 58.270694	-2.926910 ~ -2.925810
19	BE-D11	58.280369 ~ 58.281223	-2.923460 ~ -2.922180
20	BE-E1	58.181317 ~ 58.181983	-2.937536 ~ -2.936620
21	BE-E2	58.190672 ~ 58.191433	-2.935980 ~ -2.934880
22	BE-E3	58.201174 ~ 58.201840	-2.932543 ~ -2.931440
23	BE-E4	58.211440 ~ 58.212296	-2.929087 ~ -2.927990
24	BE-E5	58.221853 ~ 58.222803	-2.925628 ~ -2.924530
25	BE-E6	58.232533 ~ 58.233009	-2.922028 ~ -2.921110
26	BE-E7	58.242821 ~ 58.243297	-2.918525 ~ -2.917430
27	BE-E8	58.252588 ~ 58.253443	-2.914995 ~ -2.913900
28	BE-E9	58.263371 ~ 58.264225	-2.911519 ~ -2.910790
29	BE-E10	58.273538 ~ 58.274395	-2.908059 ~ -2.906960
30	BE-E11	58.283805 ~ 58.284659	-2.904636 ~ -2.903540
31	BE-E12	58.294209 ~ 58.295063	-2.900994 ~ -2.900080
32	BE-F2	58.194289 ~ 58.195050	-2.917130 ~ -2.916030
33	BE-F3	58.204637 ~ 58.205304	-2.913729 ~ -2.912630
34	BE-F4	58.214986 ~ 58.215842	-2.910328 ~ -2.909230
35	BE-F5	58.225357 ~ 58.226118	-2.906831 ~ -2.905730
36	BE-F6	58.235478 ~ 58.236239	-2.903344 ~ -2.902250
37	BE-F9	58.266761 ~ 58.267426	-2.892921 ~ -2.891640
38	BE-F10	58.277177 ~ 58.277936	-2.889390 ~ -2.888290
39	BE-F11	58.287406 ~ 58.288260	-2.885635 ~ -2.884720
40	BE-F12	58.297776 ~ 58.298641	-2.882294 ~ -2.881204
41	BE-F13	58.307998 ~ 58.308757	-2.878623 ~ -2.877723
42	BE-G3	58.208901 ~ 58.209472	-2.896514 ~ -2.895420

43	BE-G4	58.218492 ~ 58.219253	-2.891590 ~ -2.890490
44	BE-G5	58.228839 ~ 58.229505	-2.887927 ~ -2.886830
45	BE-G6	58.239224 ~ 58.240080	-2.884585 ~ -2.883300
46	BE-G8	58.260057 ~ 58.260722	-2.877611 ~ -2.876700
47	BE-G9	58.270526 ~ 58.271001	-2.874122 ~ -2.873020
48	BE-G10	58.280442 ~ 58.281297	-2.870293 ~ -2.869560
49	BE-G11	58.290830 ~ 58.291684	-2.867043 ~ -2.865940
50	BE-G12	58.301341 ~ 58.301911	-2.863427 ~ -2.862526
51	BE-G13	58.311696 ~ 58.312266	-2.860128 ~ -2.858867
52	BE-G14	58.322007 ~ 58.322766	-2.856352 ~ -2.855440
53	BE-H4	58.222080 ~ 58.222841	-2.872799 ~ -2.871700
54	BE-H5	58.232499 ~ 58.233260	-2.869480 ~ -2.868200
55	BE-H6	58.242762 ~ 58.243617	-2.865922 ~ -2.864640
56	BE-H7	58.253241 ~ 58.254096	-2.862160 ~ -2.861240
57	BE-H8	58.263528 ~ 58.264098	-2.858706 ~ -2.857610
58	BE-H9	58.273963 ~ 58.274533	-2.855284 ~ -2.854190
59	BE-H10	58.284289 ~ 58.285143	-2.851824 ~ -2.850730
60	BE-H11	58.294711 ~ 58.295660	-2.847944 ~ -2.847210
61	BE-H12	58.304765 ~ 58.305524	-2.844549 ~ -2.843820
62	BE-H13	58.315179 ~ 58.316033	-2.841262 ~ -2.840160
63	BE-J5	58.236053 ~ 58.236909	-2.850483 ~ -2.849570
64	BE-J6	58.246465 ~ 58.247225	-2.847071 ~ -2.845970
65	BE-J7	58.256603 ~ 58.257470	--2.843554 ~ -2.842827
66	BE-J8	58.267188 ~ 58.268137	-2.839682 ~ -2.838950
67	BE-J9	58.277369 ~ 58.278223	-2.836433 ~ -2.835880
68	BE-J10	58.287959 ~ 58.288528	-2.832998 ~ -2.831900
69	BE-J11	58.298131 ~ 58.298890	-2.829351 ~ -2.828620
70	BE-J12	58.308436 ~ 58.309099	-2.825930 ~ -2.824830
71	BE-J13	58.318897 ~ 58.319466	-2.822632 ~ -2.821350
72	BE-K6	58.249875 ~ 58.250635	-2.828074 ~ -2.827340
73	BE-K7	58.260172 ~ 58.260932	-2.824808 ~ -2.823710
74	BE-K8	58.270840 ~ 58.271410	-2.821235 ~ -2.820140

75	BE-K9	58.281094 ~ 58.281853	-2.817787 ~ -2.816690
76	BE-K10	58.291127 ~ 58.291887	-2.814041 ~ -2.813120
77	BE-K11	58.301673 ~ 58.302338	-2.810765 ~ -2.809670
78	BE-K12	58.312337 ~ 58.312811	-2.807310 ~ -2.805850
79	BE-L7	58.263993 ~ 58.264659	-2.806043 ~ -2.804940
80	BE-L8	58.274313 ~ 58.274788	-2.802514 ~ -2.801420
81	BE-L9	58.284883 ~ 58.285547	-2.799103 ~ -2.797820
82	BE-L10	58.294803 ~ 58.295562	-2.795514 ~ -2.794420
83	BE-M9	58.288175 ~ 58.288839	-2.780312 ~ -2.779210
84	BE-M10	58.298365 ~ 58.299029	-2.776723 ~ -2.775440
85	Wind turbine A	58.099998 ~ 58.100784	-3.082761 ~ -3.081860
86	Wind turbine B	58.095349 ~ 58.096018	-3.074256 ~ -3.072790
87	BE-F8*	58.256559 ~ 58.256940	-2.896245 ~ -2.895150
88	BE-G7*	58.249683 ~ 58.250159	-2.880904 ~ -2.880170

*   Offshore transformer modules (OTMs)

Table A.2.9. The detected contour range results in Moray East Wind Farm.

ID	Name	Contour range	
		Latitude (˚)	Longitude (˚)
1	ME-A01	58.075480 ~ 58.076050	-2.870150 ~ -2.867980
2	ME-A02	58.085440 ~ 58.086600	-2.869630 ~ -2.868530
3	ME-B02	58.085470 ~ 58.086050	-2.843740 ~ -2.841760
4	ME-B03	58.095570 ~ 58.096640	-2.843090 ~ -2.842370
5	ME-B04	58.105670 ~ 58.106350	-2.843540 ~ -2.841560
6	ME-B05	58.115430 ~ 58.116400	-2.842930 ~ -2.842030
7	ME-B13	58.196800~ 58.197860	-2.843400 ~ -2.841760
8	ME-B14	58.207050 ~ 58.207530	-2.842750 ~ -2.841100
9	ME-C02	58.085320 ~ 58.085800	-2.817630 ~ -2.815820
10	ME-C04	58.105540 ~ 58.106410	-2.817080 ~ -2.816000
11	ME-C05	58.115460 ~ 58.116620	-2.817100 ~ -2.816010
12	ME-C07	58.135760 ~ 58.136920	-2.816490 ~ -2.815410

13	ME-C08	58.145800 ~ 58.146960	-2.816440 ~ -2.815340
14	ME-C09	58.155860 ~ 58.156920	-2.816520 ~ -2.815240
15	ME-C10	58.166340 ~ 58.167020	-2.817370 ~ -2.815540
16	ME-C11	58.176500 ~ 58.177080	-2.817070 ~ -2.815080
17	ME-C12	58.186740 ~ 58.187220	-2.817050 ~ -2.815420
18	ME-C13	58.196870 ~ 58.197260	-2.817410 ~ -2.815210
19	ME-C14	58.207050 ~ 58.207430	-2.817200 ~ -2.815190
20	ME-C15	58.217170 ~ 58.217550	-2.816900 ~ -2.815070
21	ME-C16	58.227250 ~ 58.227730	-2.816640 ~ -2.814990
22	ME-D04	58.105390 ~ 58.106250	-2.790640 ~ -2.789740
23	ME-D05	58.115510 ~ 58.116090	-2.791060 ~ -2.789620
24	ME-D06	58.125650 ~ 58.126610	-2.790590 ~ -2.789510
25	ME-D07	58.135640 ~ 58.136500	-2.791110 ~ -2.788940
26	ME-D08	58.145940 ~ 58.146420	-2.790880 ~ -2.789260
27	ME-D09	58.155990 ~ 58.156660	-2.790910 ~ -2.788920
28	ME-D10	58.166150 ~ 58.166730	-2.790760 ~ -2.788780
29	ME-D11	58.176150 ~ 58.176910	-2.790570 ~ -2.788940
30	ME-D12	58.186130 ~ 58.187280	-2.790700 ~ -2.789430
31	ME-D13	58.196190 ~ 58.197330	-2.789900 ~ -2.788640
32	ME-D14	58.206620 ~ 58.207480	-2.790070 ~ -2.788810
33	ME-D15	58.216690 ~ 58.217360	-2.789940 ~ -2.788660
34	ME-D16	58.226900 ~ 58.227670	-2.790000 ~ -2.788720
35	ME-D17	58.236950 ~ 58.237610	-2.789650 ~ -2.788930
36	ME-E04	58.104890 ~ 58.105950	-2.764230 ~ -2.763140
37	ME-E05	58.114890 ~ 58.115760	-2.763970 ~ -2.763240
38	ME-E14	58.206550 ~ 58.207040	-2.764210 ~ -2.762410
39	ME-E18	58.247160 ~ 58.247550	-2.763740 ~ -2.762120
40	ME-E19	58.257280 ~ 58.257760	-2.764230 ~ -2.761880
41	ME-F04	58.104970 ~ 58.105740	-2.738190 ~ -2.737100
42	ME-F08	58.145410 ~ 58.146090	-2.738260 ~ -2.736450
43	ME-F21	58.277280 ~ 58.277670	-2.737420 ~ -2.735980
44	ME-G05	58.114570 ~ 58.115530	-2.711550 ~ -2.710460

45	ME-G06	58.124970 ~ 58.125830	-2.711860 ~ -2.710780
46	ME-G07	58.134910 ~ 58.135970	-2.711500 ~ -2.710240
47	ME-G08	58.145150 ~ 58.145820	-2.712240 ~ -2.710080
48	ME-G09	58.155210 ~ 58.156080	-2.711380 ~ -2.710280
49	ME-G10	58.165380 ~ 58.166430	-2.711430 ~ -2.710170
50	ME-G11	58.175360 ~ 58.176500	-2.711170 ~ -2.710080
51	ME-G13	58.195710 ~ 58.196670	-2.711200 ~ -2.709930
52	ME-G15	58.216130 ~ 58.216710	-2.711400 ~ -2.709600
53	ME-G16	58.226490 ~ 58.226880	-2.711400 ~ -2.709230
54	ME-G17	58.236350 ~ 58.237030	-2.711540 ~ -2.709740
55	ME-G18	58.246420 ~ 58.247380	-2.710560 ~ -2.709480
56	ME-G19	58.256600 ~ 58.257360	-2.710660 ~ -2.709210
57	ME-G20	58.266680 ~ 58.267720	-2.710720 ~ -2.709090
58	ME-G21	58.277010 ~ 58.277780	-2.710630 ~ -2.709370
59	ME-G22	58.286960 ~ 58.287830	-2.710450 ~ -2.709010
60	ME-H05	58.114800 ~ 58.115190	-2.685670 ~ -2.683680
61	ME-H06	58.124520 ~ 58.125580	-2.685670 ~ -2.684230
62	ME-H07	58.134790 ~ 58.135750	-2.685630 ~ -2.684370
63	ME-H08	58.144780 ~ 58.145740	-2.685060 ~ -2.683980
64	ME-H09	58.155020 ~ 58.155790	-2.684980 ~ -2.683880
65	ME-H10	58.165030 ~ 58.165890	-2.685170 ~ -2.683730
66	ME-H11	58.175210 ~ 58.176170	-2.685050 ~ -2.683790
67	ME-H13	58.195680 ~ 58.196550	-2.684730 ~ -2.683650
68	ME-H14	58.205970 ~ 58.206830	-2.684470 ~ -2.683750
69	ME-H16	58.226130 ~ 58.226610	-2.685300 ~ -2.683310
70	ME-H17	58.235940 ~ 58.237000	-2.684250 ~ -2.683350
71	ME-H18	58.246130 ~ 58.246990	-2.684530 ~ -2.683080
72	ME-H19	58.256430 ~ 58.257290	-2.684150 ~ -2.682890
73	ME-H20	58.266850 ~ 58.267230	-2.684840 ~ -2.682640
74	ME-H21	58.276700 ~ 58.277460	-2.684520 ~ -2.682710
75	ME-H22	58.286880 ~ 58.287450	-2.684170 ~ -2.682540
76	ME-I06	58.124640 ~ 58.125510	-2.659180 ~ -2.658280

77	ME-I07	58.134450 ~ 58.135510	-2.659020 ~ -2.657750
78	ME-I18	58.245870 ~ 58.247020	-2.657780 ~ -2.656870
79	ME-I19	58.256280 ~ 58.256960	-2.657830 ~ -2.656550
80	ME-I20	58.266430 ~ 58.267110	-2.657900 ~ -2.656820
81	ME-J07	58.134320 ~ 58.135280	-2.632820 ~ -2.631550
82	ME-J08	58.144710 ~ 58.145470	-2.632900 ~ -2.631820
83	ME-J09	58.154540 ~ 58.155590	-2.632660 ~ -2.631580
84	ME-J10	58.164910 ~ 58.165490	-2.632540 ~ -2.630550
85	ME-J12	58.184860 ~ 58.185720	-2.632100 ~ -2.631020
86	ME-J13	58.194980 ~ 58.196030	-2.631910 ~ -2.631010
87	ME-J14	58.205360 ~ 58.206320	-2.632260 ~ -2.631170
88	ME-J16	58.225450 ~ 58.226410	-2.631830 ~ -2.630930
89	ME-J17	58.235790 ~ 58.236940	-2.631920 ~ -2.630840
90	ME-J18	58.245860 ~ 58.246820	-2.632270 ~ -2.630640
91	ME-J19	58.255970 ~ 58.256840	-2.631800 ~ -2.630710
92	ME-K09	58.154250 ~ 58.155300	-2.606410 ~ -2.605330
93	ME-K10	58.164300 ~ 58.165260	-2.605940 ~ -2.604860
94	ME-K11	58.174760 ~ 58.175430	-2.606570 ~ -2.604940
95	ME-K16	58.225500 ~ 58.226170	-2.606110 ~ -2.604380
96	ME-K17	58.235830 ~ 58.236600	-2.602440 ~ -2.601360
97	ME-L09	58.154090 ~ 58.154960	-2.580060 ~ -2.578980
98	ME-L11	58.174680 ~ 58.175250	-2.580260 ~ -2.578280
99	ME-L12	58.184670 ~ 58.185150	-2.579980 ~ -2.578180
100	ME-L13	58.194600 ~ 58.195650	-2.579790 ~ -2.578530
101	OSP1*	58.125490 ~ 58.125870	-2.764110 ~ -2.763390
102	OSP2*	58.216400 ~ 58.216970	-2.737380 ~ -2.736480
103	OSP3*	58.165220 ~ 58.165600	-2.658650 ~ -2.657930

*   Offshore Substation Platform (OSP)

Table A.2.10. The detected contour range results in HyWind Wind Farm (Aberdeenshire).

ID	Name	Contour range

		Latitude (˚)	Longitude (˚)
1	HS1	57.483710 ~ 57.484580	-1.333010 ~ -1.331930
2	HS2	57.490105 ~ 57.490989	-1.352627 ~ -1.351338
3	HS3	57.496672 ~ 57.497458	-1.372470 ~ -1.371181
4	HS4	57.477897 ~ 57.478684	-1.353303 ~ -1.352034
5	HS5	57.484250 ~ 57.485321	-1.373062 ~ -1.371802

Table A.2.11. The detected contour range results in Kincardine Wind Farm (Aberdeenshire).

ID	Name	Contour range	
		Latitude (˚)	Longitude (˚)
1	KIN-01	57.004740 ~ 57.005730	-1.882010 ~ -1.880730
2	KIN-02	56.996640 ~ 56.997340	-1.874750 ~ -1.873110
3	KIN-03	56.988690 ~ 56.989590	-1.867260 ~ -1.865980
4	KIN-04	57.018040 ~ 57.018940	-1.856110 ~ -1.854830
5	KIN-05	57.009990 ~ 57.010790	-1.848490 ~ -1.846840

Table A.2.12. The detected contour range results in Aberdeen Offshore Wind Farm.

ID	Name	Contour range	
		Latitude (˚)	Longitude (˚)
1	AWF01	57.223170 ~ 57.223970	-2.013430 ~ -2.012170
2	AWF02	57.228119 ~ 57.228918	-2.002626 ~ -2.001718
3	AWF03	57.233165 ~ 57.234056	-1.989992 ~ -1.988723
4	AWF04	57.239830 ~ 57.240520	-1.976230 ~ -1.974950
5	AWF05	57.215390 ~ 57.216280	-2.011910 ~ -2.010820
6	AWF06	57.219750 ~ 57.220440	-2.001110 ~ -1.999460
7	AWF07	57.223890 ~ 57.224784	-1.988600 ~ -1.987330
8	AWF08	57.229623 ~ 57.230613	-1.974905 ~ -1.973817
9	AWF09	57.207500 ~ 57.208195	-2.011340 ~ -2.009520
10	AWF10	57.211302 ~ 57.212194	-1.999313 ~ -1.998024
11	AWF11	57.215623 ~ 57.216514	-1.986536 ~ -1.985083

A.2.3 The size measuring results

Table A.2.13. The topside area estimate accuracies of oil/gas platforms and semi-permanent objects in Scottish waters.

ID	Name	The detected size (Square meters)	The actual size (Square meters)	Size error (Square meters)
1	Dunbar	5300	5394	94
2	Magnus	7100	7565	465
3	Western Isles FPSO	5400	5544	144
4	Tern	5100	5208	108
5	Heather Alpha	4100	4290	190
6	Cormorant Alpha	5500	5656	156
7	North Cormorant	5800	5915	115
8	Eider	3900	3818	82
9	Ninian north *	—	—	—
10	Ninian South	7500	7209	291
11	Northern Producer *	—	—	—
12	Ninian Central	5500	5888	388
13	Thistle Alpha	6400	6460	60
14	Dunlin Alpha	7000	6840	160
15	Brent Bravo *	—	—	—
16	Brent Charlie	5800	6172	372
17	Alwyn North Bravo	3800	3551	249
18	Alwyn North Alpha	3800	3927	127
19	Brent Delta *	—	—	—
20	Noble Lloyd Noble	4900	4494	406
21	Mariner PDQ	9700	9912	212
22	Mariner FSU	9700	10130	430
23	Kraken FPSO	11300	12502	1202
24	Beryl Bravo	4800	4689	111
25	Harding	5500	5304	196
26	Beryl Alpha	800	1020	220

27	Beryl Flare [†]	—	378	—
28	Beryl Alpha Riser	4100	4352	252
29	Beryl SPM-3	600	864	264
30	Beryl SPM-2	2300	2179	121
31	Gryphon Alpha FPSO	12200	12288	88
32	Bruce PUQ	5300	4698	602
33	Bruce CR [†]	—	706	—
34	Bruce Drilling	4000	4212	212
35	Tartan Alpha	4800	4823	23
36	Scott DP	2700	2964	264
37	Scott Utilities and Quarters	3400	3680	280
38	Piper Bravo	6300	6090	210
39	Saltire	4900	4785	115
40	Global Producer III FPSO	8400	8660	260
41	Alba FPSO	4300	9315	5015
42	Alba North	5700	5520	180
43	Balmoral FPSO	4900	5010	110
44	Britannia	6100	6032	68
45	Britannia BLP	2400	2279	121
46	Hummingbird FPSO	3800	4154	354
47	Tiffany	5300	5358	58
48	Brae Alpha	5400	5544	144
49	Brae Bravo	4200	4140	60
50	Andrew	5500	5246	254
51	Brae East	4200	4560	360
52	Glen Lyon FPSO	13500	13152	348
53	Solan	4000	4296	296
54	Aoka Mizu FPSO	11800	11662	138
55	Clair	6500	6627	127
56	Clair Ridge DP	5800	5972	172
57	Clair Ridge QU	5000	5151	151
58	Foinaven FPSO	11200	11397	197

59	Claymore Production	4700	4740	40
60	Claymore Accommodation	4600	4484	116
61	Captain BLP	2200	2236	36
62	Captain wellhead protection platform	4600	4350	250
63	Captain FPSO	11300	10731	569
64	Ross FPSO	9100	9844	744
65	Well Head	2700	2583	117
66	Production Jacket	4300	4128	172
67	Quarters Utilities (QU) Jacket	4500	4181	319
68	Oil Stripper platform	2400	2107	293
69	Golden Eagle Wellhead	3400	3549	149
70	Golden Eagle PUQ	4500	4788	288
71	Kittiwake	4400	4032	368
72	Catcher FPSO	10200	11050	850
73	Forties Unity	1900	1539	361
74	Anasuria FPSO	8400	9072	672
75	Forties Charlie	5300	5760	460
76	Triton FPSO	9300	9460	160
77	Forties Delta	4700	4686	14
78	Forties Bravo	3900	4180	280
79	Forties Alpha	5700	5616	84
80	Fasp	3000	3036	36
81	Gannet Alpha	6700	6544	156
82	Forties Echo	1700	1987	287
83	Nelson	6800	6467	333
84	Arbroath	2400	2201	199
85	Montrose BLP	2600	2916	316
86	Montrose Alpha	4400	4104	296
87	Etap PDR	3900	3776	124
88	Etap QU	4600	4108	492
89	North Everest	4500	4418	82

90	Cats Riser	2300	2100	200
91	West Franklin WHP	1700	2050	350
92	Elgin A WHP †	—	1450	—
93	Elgin B WHP †	—	5976	—
94	Elgin PUQ	5800	5751	49
95	Franklin WHP	6300	6520	220
96	Culzean Utilities and Living Quarters	3500	3610	110
97	Culzean Central Processing Facility	4400	4277	123
98	Culzean WHP	7400	7701	301
99	Shearwater A	5300	5016	284
100	Shearwater C	4800	4576	224
101	Erskine	2100	2028	72
102	FPF1 FPSO	4400	6525	2125
103	Mungo	1700	1672	28
104	Lomond	4100	4165	65
105	Jasmine Wellhead	7300	7112	188
106	Jasmine Living Quarters	1900	2180	280
107	Jade	1900	2108	208
108	Haewene Brim FPSO	3400	9476	6076
109	Judy Riser and Separation Platform	3800	4176	376
110	Judy	5900	5775	125
111	Culzean FSO - Ailsa	4700	9360	4660
112	Armada	5300	4989	311
113	Jacky platform	5000	4964	36
114	Beatrice Charlie *	—	—	—
115	Betrice Alpha Drilling *	—	—	—
116	Beatrice Alpha Production *	—	—	—
117	Beatrice Bravo *	—	—	—

	Manifold and Compression	—	—	—
118	Platform 01 (MCP01) *			
	Frigg Treatment platform 1	—	—	—
119	(TP1) *			
	Frigg Concrete drilling platform	—	—	—
120	1 (CDP1) *			
	Frigg Treatment Compression	—	—	—
121	Platform 2 (TCP 2) *			

* The infrastructure has undergone decommissioning.

† The infrastructure is omitted in Sentinel-2 data.

Table A.2.14. The diameter length estimate accuracies of wind turbines in Beatrice Wind Farm.

ID	Name	The detected size (meter)	The actual size (meter)	The size error (meter)
1	BE-A5	160±5	154	6±5
2	BE-B5	145±5	154	9±5
3	BE-B6	145±5	154	9±5
4	BE-B7	135±5	154	19±5
5	BE-C4	160±5	154	6±5
6	BE-C5	145±5	154	9±5
7	BE-C6	150±5	154	4±5
8	BE-C7	135±5	154	19±5
9	BE-C8	160±5	154	6±5
10	BE-C9	140±5	154	14±5
11	BE-D3	135±5	154	19±5
12	BE-D4	160±5	154	6±5
13	BE-D5	150±5	154	4±5
14	BE-D6	170±5	154	16±5
15	BE-D7	145±5	154	9±5
16	BE-D8	160±5	154	6±5
17	BE-D9	165±5	154	11±5
18	BE-D10	170±5	154	16±5

19	BE-D11	160±5	154	6±5
20	BE-E1	155±5	154	1±5
21	BE-E2	145±5	154	9±5
22	BE-E3	150±5	154	4±5
23	BE-E4	145±5	154	9±5
24	BE-E5	170±5	154	16±5
25	BE-E6	145±5	154	9±5
26	BE-E7	135±5	154	19±5
27	BE-E8	160±5	154	6±5
28	BE-E9	170±5	154	16±5
29	BE-E10	155±5	154	1±5
30	BE-E11	155±5	154	1±5
31	BE-E12	145±5	154	9±5
32	BE-F2	135±5	154	19±5
33	BE-F3	145±5	154	9±5
34	BE-F4	145±5	154	9±5
35	BE-F5	135±5	154	19±5
36	BE-F6	145±5	154	9±5
37	BE-F9	145±5	154	9±5
38	BE-F10	140±5	154	14±5
39	BE-F11	140±5	154	14±5
40	BE-F12	155±5	154	1±5
41	BE-F13	150±5	154	4±5
42	BE-G3	145±5	154	9±5
43	BE-G4	145±5	154	9±5
44	BE-G5	135±5	154	19±5
45	BE-G6	145±5	154	9±5
46	BE-G8	155±5	154	1±5
47	BE-G9	145±5	154	9±5
48	BE-G10	170±5	154	16±5
49	BE-G11	170±5	154	16±5

50	BE-G12	135±5	154	19±5
51	BE-G13	155±5	154	1±5
52	BE-G14	145±5	154	9±5
53	BE-H4	170±5	154	16±5
54	BE-H5	155±5	154	1±5
55	BE-H6	160±5	154	6±5
56	BE-H7	150±5	154	4±5
57	BE-H8	155±5	154	1±5
58	BE-H9	135±5	154	19±5
59	BE-H10	145±5	154	9±5
60	BE-H11	150±5	154	4±5
61	BE-H12	150±5	154	4±5
62	BE-H13	140±5	154	14±5
63	BE-J5	140±5	154	14±5
64	BE-J6	135±5	154	19±5
65	BE-J7	150±5	154	4±5
66	BE-J8	150±5	154	4±5
67	BE-J9	140±5	154	14±5
68	BE-J10	160±5	154	6±5
69	BE-J11	150±5	154	4±5
70	BE-J12	135±5	154	19±5
71	BE-J13	150±5	154	4±5
72	BE-K6	170±5	154	16±5
73	BE-K7	145±5	154	9±5
74	BE-K8	140±5	154	14±5
75	BE-K9	140±5	154	14±5
76	BE-K10	150±5	154	4±5
77	BE-K11	145±5	154	9±5
78	BE-K12	145±5	154	9±5
79	BE-L7	135±5	154	19±5
80	BE-L8	135±5	154	19±5

81	BE-L9	170±5	154	16±5
82	BE-L10	155±5	154	1±5
83	BE-M9	145±5	154	9±5
84	BE-M10	145±5	154	9±5
85	Wind turbine A	145±5	154	9±5
86	Wind turbine B	155±5	154	1±5
87	BE-F8*	—	—	—
88	BE-G7*	—	—	—

* Offshore transformer modules (OTMs)

Table A.2.15. The diameter length estimate accuracies in Moray East Wind Farm.

ID	Name	The detected size (meter)	The actual size (meter)	The size error (meter)
1	ME-A01	160±5	164	4±5
2	ME-A02	170±5	164	6±5
3	ME-B02	160±5	164	4±5
4	ME-B03	145±5	164	19±5
5	ME-B04	180±5	164	16±5
6	ME-B05	180±5	164	16±5
7	ME-B13	185±5	164	21±5
8	ME-B14	160±5	164	4±5
9	ME-C02	165±5	164	1±5
10	ME-C04	150±5	164	14±5
11	ME-C05	170±5	164	6±5
12	ME-C07	170±5	164	6±5
13	ME-C08	170±5	164	6±5
14	ME-C09	180±5	164	16±5
15	ME-C10	155±5	164	9±5
16	ME-C11	155±5	164	9±5
17	ME-C12	145±5	164	19±5

18	ME-C13	160±5	164	4±5
19	ME-C14	160±5	164	4±5
20	ME-C15	150±5	164	14±5
21	ME-C16	150±5	164	14±5
22	ME-D04	150±5	164	14±5
23	ME-D05	145±5	164	19±5
24	ME-D06	170±5	164	6±5
25	ME-D07	185±5	164	21±5
26	ME-D08	150±5	164	14±5
27	ME-D09	160±5	164	4±5
28	ME-D10	160±5	164	4±5
29	ME-D11	155±5	164	9±5
30	ME-D12	185±5	164	21±5
31	ME-D13	170±5	164	6±5
32	ME-D14	145±5	164	19±5
33	ME-D15	150±5	164	14±5
34	ME-D16	145±5	164	19±5
35	ME-D17	140±5	164	24±5
36	ME-E04	170±5	164	6±5
37	ME-E05	170±5	164	6±5
38	ME-E14	145±5	164	19±5
39	ME-E18	145±5	164	19±5
40	ME-E19	180±5	164	16±5
41	ME-F04	145±5	164	19±5
42	ME-F08	155±5	164	9±5
43	ME-F21	145±5	164	19±5
44	ME-G05	170±5	164	6±5
45	ME-G06	150±5	164	14±5
46	ME-G07	170±5	164	6±5
47	ME-G08	170±5	164	6±5
48	ME-G09	150±5	164	14±5

49	ME-G10	180±5	164	16±5
50	ME-G11	170±5	164	6±5
51	ME-G13	155±5	164	9±5
52	ME-G15	155±5	164	9±5
53	ME-G16	170±5	164	6±5
54	ME-G17	170±5	164	6±5
55	ME-G18	160±5	164	4±5
56	ME-G19	150±5	164	14±5
57	ME-G20	185±5	164	21±5
58	ME-G21	145±5	164	19±5
59	ME-G22	170±5	164	6±5
60	ME-H05	170±5	164	6±5
61	ME-H06	170±5	164	6±5
62	ME-H07	155±5	164	9±5
63	ME-H08	150±5	164	14±5
64	ME-H09	150±5	164	14±5
65	ME-H10	185±5	164	21±5
66	ME-H11	155±5	164	9±5
67	ME-H13	145±5	164	19±5
68	ME-H14	180±5	164	16±5
69	ME-H16	180±5	164	16±5
70	ME-H17	180±5	164	16±5
71	ME-H18	170±5	164	6±5
72	ME-H19	155±5	164	9±5
73	ME-H20	170±5	164	6±5
74	ME-H21	155±5	164	9±5
75	ME-H22	150±5	164	14±5
76	ME-I06	150±5	164	14±5
77	ME-I07	160±5	164	4±5
78	ME-I18	170±5	164	6±5
79	ME-I19	145±5	164	19±5

80	ME-I20	145±5	164	19±5
81	ME-J07	155±5	164	9±5
82	ME-J08	150±5	164	14±5
83	ME-J09	170±5	164	6±5
84	ME-J10	180±5	164	16±5
85	ME-J12	170±5	164	6±5
86	ME-J13	170±5	164	6±5
87	ME-J14	155±5	164	9±5
88	ME-J16	155±5	164	9±5
89	ME-J17	180±5	164	16±5
90	ME-J18	170±5	164	6±5
91	ME-J19	150±5	164	14±5
92	ME-K09	170±5	164	6±5
93	ME-K10	170±5	164	6±5
94	ME-K11	145±5	164	19±5
95	ME-K16	155±5	164	9±5
96	ME-K17	170±5	164	6±5
97	ME-L09	155±5	164	9±5
98	ME-L11	155±5	164	9±5
99	ME-L12	145±5	164	19±5
100	ME-L13	170±5	164	6±5
101	OSP1*	—	—	—
102	OSP2*	—	—	—
103	OSP3*	—	—	—

* Offshore Substation Platform (OSP)

Table A.2.16. The diameter length estimate accuracies in HyWind Wind Farm (Aberdeenshire).

ID	Name	The detected size (meter)	The actual size (meter)	The size error (meter)
1	HS1	145±5	154	9±5
2	HS2	145±5	154	9±5
3	HS3	145±5	154	9±5
4	HS4	145±5	154	9±5

5	HS5	160±5	154	6 ± 5

Table A.2.17. The diameter length estimate accuracies in Kincardine Wind Farm (Aberdeenshire).

ID	Name	The detected size (meter)	The actual size (meter)	The size error (meter)
1	KIN-01	170±5	164	6±5
2	KIN-02	155±5	164	9±5
3	KIN-03	170±5	164	6±5
4	KIN-04	150±5	164	14±5
5	KIN-05	155±5	164	9±5

Table A.2.18. The diameter length estimate accuracies in Aberdeen Offshore Wind Farm.

ID	Name	The detected size (meter)	The actual size (meter)	The size error (meter)
1	AWF01	145±5	150	5±5
2	AWF02	155±5	150	5±5
3	AWF03	155±5	150	5±5
4	AWF04	155±5	150	5±5
5	AWF05	150±5	150	0±5
6	AWF06	155±5	150	5±5
7	AWF07	145±5	150	5±5
8	AWF08	155±5	150	5±5
9	AWF09	155±5	150	5±5
10	AWF10	170±5	150	20±5
11	AWF11	155±5	150	5

Appendix 3: Parameter analysis

A.3.1 Parameters in 2D-SSA filtering

When applying 2D-SSA, the image can be decomposed and reconstructed based on the eigenvalues obtained in singular value decomposition (SVD). In general, the first component contains the main information of input data, while noises are usually existed in those small eigenvalues. Fig. A.3.1. shows the different components of input Sentinel-1 image after 2D-SSA decomposition. It is clear that the first component in Fig. A.3.1. (b) contains the clearer and more discriminative features of the platforms, while the 2nd, 3rd, 4th components in Fig. A.3.1. (c-e) keep the noisy contents. Therefore, in this paper, we only utilize the first component to reconstruct the image.

Another key parameter in 2D-SSA is the window size, which also affects the noise level of image. A large window size leads to more smoothed results with most of noisy content removed. Here, the effects of different window sizes are test. The filtered images by 2D-SSA with the wind sizes of 3×3, 5×5, and 10×10, and their corresponding results by threshold segmentation are depicted in Fig. A.3.2. It is clear that increasing the window size can reduce the noises in threshold segmentation result. When using the window size of 3×3, there are still some noises on the edges of the detected object as shown in Fig. A.3.2 (f). However, when the window size equals to 10×10, the filtered image in Fig. A.3.2 (d) would lose many feature details of object with the distorted segmentation result. Besides, a large window size in 2D-SSA would increase the computational cost. Therefore, to achieve an efficient and effective filter, the window sizes of 5×5 and the first component is employed in 2D-SSA.

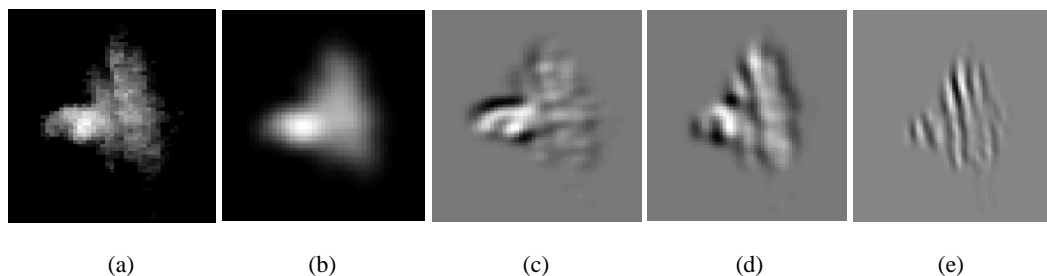| (a) | (b) | (c) | (d) | (e) |

Fig. A.3.1 The different components of the input Sentinel-1 image after 2D-SSA decomposition. (a) The input median composite image; (b) The 1st component; (c) The 2nd component; (d) The 3rd component; (e) The 4th component.
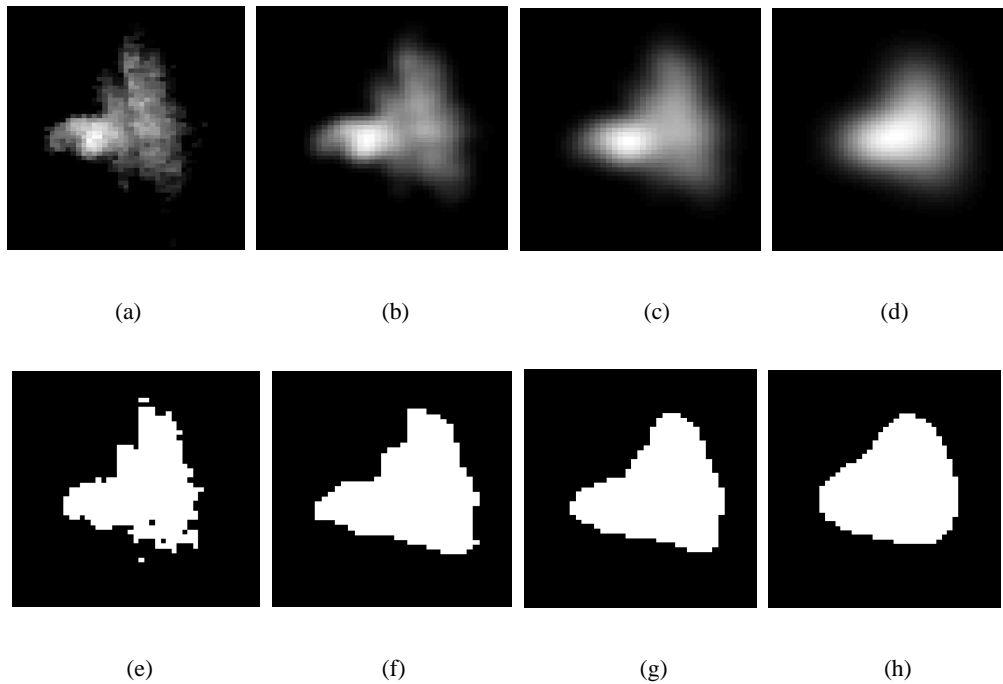
175

Fig. A.3.2. The effects of different window sizes of 2D-SSA on the proposed method. (a) The input median composite image; (b) The filtered image by 2D-SSA with window size of 3×3; (c) The filtered image by 2D-SSA with window size of 5×5; (d) The filtered image by 2D-SSA with window size of 10×10; (e) The threshold segmentation results of (a); (f) The threshold segmentation results of (b); (g) The threshold segmentation results of (c); (h) The threshold segmentation results of (d).

A.3.2 Parameters in morphological reconstruction operation

The morphological reconstruction operation can modify the intensity of images and distinguish the offshore infrastructure from the background. In this operation, the structural element plays an important role in the intensity changing. Here the radius value of disc structural element is analysed. Fig. A.3.3 shows the detected results of the offshore infrastructure with different topside area in Sentinel-2 data after the morphological reconstruction with the radius value of 1, 2 and 3, respectively. We take the Forties Unity platform (Fig. A.3.3 (a)) and Anasuria FPSO (Fig. A.3.3 (e)) as examples. The Forties Unity platform has a smaller topside area comparing with the Anasuria FPSO. From Fig. A.3.3 (b-c), it is clear that the radius equalling to 2 can achieve the best detection results while large radius value would increase the topside area of the platform. As for the Anasuria FPSO, however, the radius equalling to 2 is too small to extract the complete structure. Therefore, in this paper, after the contour detection in Sentinel-1 data, the "guide area" locates the candidate Sentinel-2 image

176

subset containing the offshore infrastructure. The size of this subset Sentinel-2 image is extracted. Empirically, if the width or length of this subset is larger than 18 pixels, the radius equalling to 3 is utilized in the following morphological operations on Sentinel-2. On the other hand, the radius value is set to 2 for the image with smaller width and length.
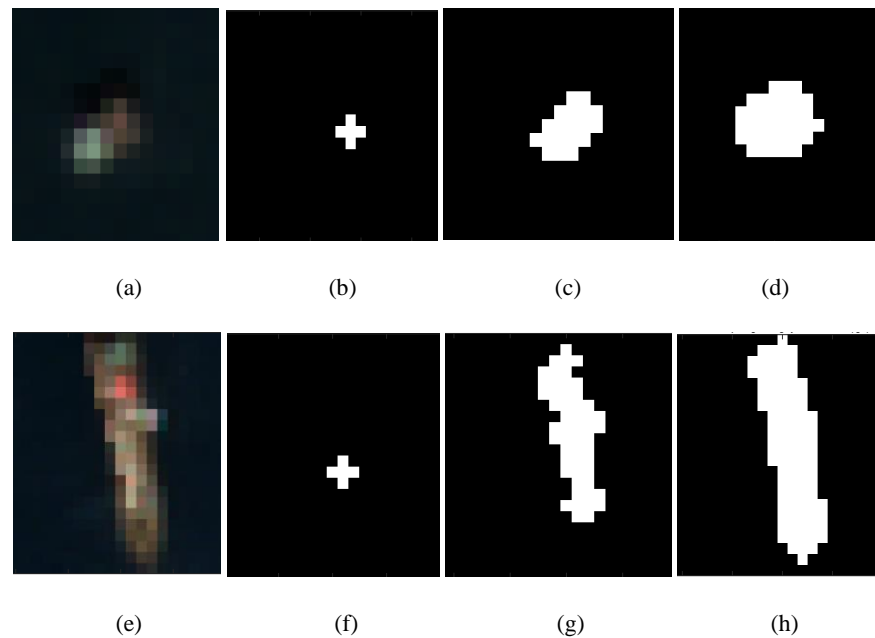

| | | | |
| (a) | (b) | (c) | (d) |

| | | | |
| (e) | (f) | (g) | (h) |

Fig. A.3.3. The effects of radius value in disc structural element of morphological reconstruction operation. (a) The Sentinel-2 true color image for Forties Unity platform; (b) The detected results of (a) when radius value is 1; (c) The detected results of (a) when radius value is 2; (d) The detected results of (a) when radius value is 3; (e) The Sentinel-2 true color image for Anasuria FPSO; (f) The detected results of (e) when radius value is 1; (g) The detected results of (e) when radius value is 2; (h) The detected results of (e) when radius value is 3;

A.3.3 Geolocating with contour range

In this paper, an offshore infrastructure is considered as a correct identification when its ground truth is within the detected contour range. The databases used for constructing ground truth could lack up-to-date information. Fig. A.3.4 shows the bounding box and three kinds of centres based on the detection results, and the corresponding ground truth location of different offshore infrastructure. Here the centre of bounding box, centroid and geometric median are used respectively for presenting the centre location of the detected infrastructure. Note that geometric median denotes the location that minimizes the sum of distances to all detected pixels of target. From Fig. A.3.4, it is clear that the bounding box can effectively extract the

contour range of each offshore infrastructure. As shown in Figs. A.3.4, the ground truth can locate the target infrastructure but not in the exact centre position. In comparison, the centre of bounding box, centroid and geometric median can better locate the centre location. Especially for the FPSO, such as Aoka Mizu FPSO shown in Fig. A.3.4 (c), it would drift with wave and need updates in ground truth frequently. Given this, we use the contour range in this paper to locate the whole structure of an offshore infrastructure.
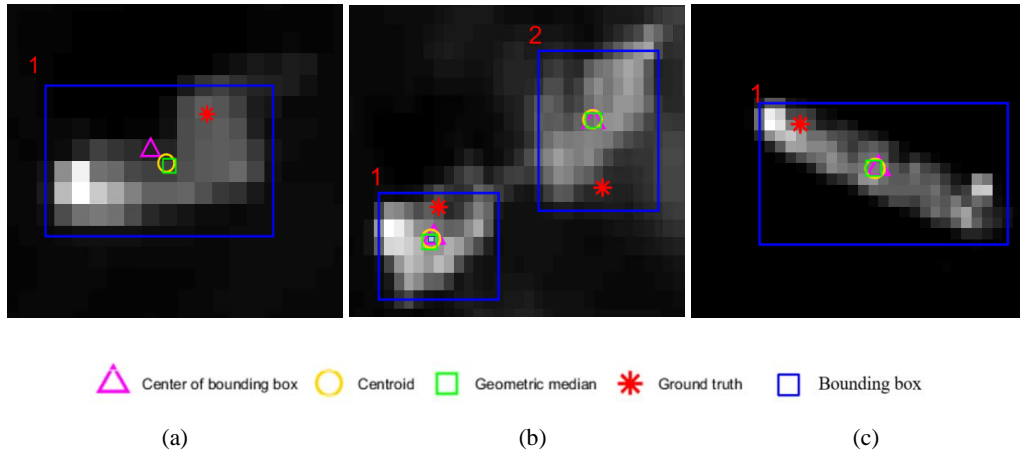

△ Center of bounding box ○ Centroid □ Geometric median ✳ Ground truth □ Bounding box

(a)　　　　　　　　　　(b)　　　　　　　　　　(c)

Fig. A.3.4. The center location and ground truth of offshore infrastructure. (a) Clair platform; (b) The linked rig including Clair Ridge DP and Clair Ridge QU; (c) Aoka Mizu FPSO